Journal of Catalysis 380 (2019) 161–177

Contents lists available at ScienceDirect

Journal of Catalysis

journal homepage: www.elsevier.com/locate/jcat

Mechanistic origins of the high-pressure inhibition of methanol dehydration rates in small-pore acidic zeolites

John R. Di Iorio [a], Alexander J. Hoffman [b], Claire T. Nimlos [a], Steven Nystrom [b], David Hibbitts [b,*], Rajamani Gounder [a,*]

[a] Charles D. Davidson School of Chemical Engineering, Purdue University, 480 Stadium Mall Drive, West Lafayette, IN 47907, USA
[b] Department of Chemical Engineering, University of Florida, 1030 Center Drive, Gainesville, FL 32611, USA

ARTICLE INFO

Article history:
Received 7 August 2019
Revised 26 September 2019
Accepted 5 October 2019
Available online 31 October 2019

Keywords:
Methanol dehydration
Reactant inhibition
Chabazite
Zeolite
Heterogeneous catalysis

ABSTRACT

Turnover rates of Brønsted acid-catalyzed methanol dehydration to dimethyl ether become inhibited at high methanol pressures (>10 kPa, 415 K) on small-pore zeolites (CHA, AEI, LTA, LEV), irrespective of the distribution of framework Al and their attendant H^+ sites, but not on medium-pore or large-pore zeolites. High-pressure kinetic inhibition occurs concomitantly with the stabilization of higher-order methanol clusters (e.g., trimers, tetramers) observed experimentally by physisorption of liquid-like methanol and the appearance of vibrational modes for methanol clusters in IR spectra, consistent with the attenuation of such inhibition at higher temperatures (>450 K) that result in decreased methanol coverage. DFT-predicted methanol coverage phase diagrams confirm that higher-order methanol clusters form in pressure and temperature ranges corresponding to the onset of kinetic inhibition observed experimentally, and that higher-order methanol clusters are reactive but that excess methanol increases the apparent barriers to form kinetically relevant transition states that eliminate dimethyl ether and thus inhibit turnover rates. This combined experimental and theoretical investigation provides precise mechanistic interpretation of the high-pressure inhibition of methanol dehydration turnover rates on small-pore Brønsted acid zeolites. This rigorous analysis enables the development of kinetic models to account for the diverse structures of methanol precursors that dehydrate to form dimethyl ether, and methods to assess the prevalence of higher-order clusters that serve as reactive and inhibitory intermediates within small-pore zeolites during methanol conversion.

1. Introduction

Methanol is a promising carbon source for producing light olefins (e.g., ethene, propene) and aromatics over acidic zeolite catalysts at elevated temperatures (>453 K) via the methanol-to-olefins (MTO) and methanol-to-gasoline (MTG) processes [1,2], in which product selectivities can be tuned via judicious choice of reaction conditions (e.g., temperature, methanol pressure) [3] and zeolite framework [3–5]. The conversion of methanol into olefins proceeds through a "hydrocarbon pool" mechanism, wherein methanol is dehydrated at Brønsted acid sites to form methoxy intermediates that subsequently react with confined polymethylated aromatics to generate new C—C bonds [3,4,6]. Surface-bound methoxy groups (CH_3—Z), formed via methanol dehydration, have also been implicated in the initiation of C—C bond formation, at low turnover numbers, via carbonylation with either carbon monoxide or formaldehyde present either as impurities or formed during reaction [6–8]. Methanol dehydration to dimethyl ether (DME) occurs selectively without olefin formation at low-temperatures (<453 K) [9,10], and measurement of methanol dehydration rate constants has enabled investigating the individual effects of confinement and acid strength in zeolite acid catalysis [10–12].

Methanol dehydration to DME on solid Brønsted acids can proceed via two different mechanisms, referred to as the associative (concerted) or dissociative (sequential) mechanisms (Scheme 1) [10–14]. The first step in both mechanisms is quasi-equilibrated adsorption of a gas-phase methanol at a bare proton. In the associative mechanism, protonated methanol dimers form via quasi-equilibrated adsorption of a second gas-phase methanol, and then eliminate DME and water in a kinetically relevant dehydration step (Scheme 1, top). The dissociative mechanism (Scheme 1, bottom), in contrast, involves kinetically relevant dehydration of methanol monomers to eliminate water and form a surface-bound methoxy

* Corresponding authors.
E-mail addresses: hibbitts@ufl.edu (D. Hibbitts), rgounder@purdue.edu (R. Gounder).

https://doi.org/10.1016/j.jcat.2019.10.012
0021-9517/

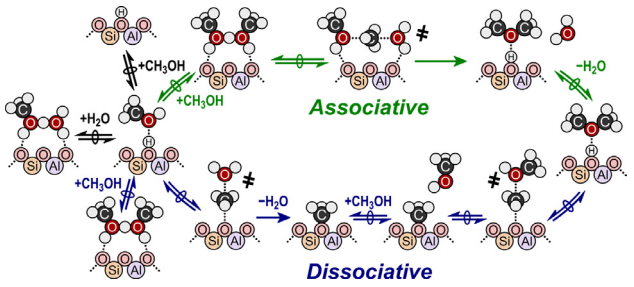

Scheme 1. Structures of intermediates and transition states (marked as ‡) for the associative (top path) and dissociative (bottom path) mechanisms of Brønsted acid-catalyzed methanol dehydration to DME.

intermediate. Surface methoxy intermediates then undergo nucleophilic attack by a second gas-phase methanol in a quasi-equilibrated step to form DME. DME formation rates via the dissociative mechanism are thus inhibited by the formation of protonated methanol dimers [10], while methanol-water complexes can inhibit both pathways (Scheme 1).

Measured reaction kinetics (433 K) and DFT calculations indicate that methanol dehydration to DME proceeds via the associative mechanism at Brønsted acid sites (H^+ sites) of polyoxometalate clusters (POM) supported on amorphous SiO_2 [10], and at such sites confined within medium-pore and large-pore zeolites (FAU, SFH, BEA, MOR, MTW, MFI, and MTT, 0.5–1.2 nm diameter voids) [11–13,15]. Turnover rates of methanol dehydration (433 K, per H^+) on these catalysts follow a Langmuirian dependence on methanol partial pressure (0.05–20 kPa), transitioning from a first-order to zero-order kinetic regime at high methanol pressures. Additionally, *in situ* IR spectra measured on MFI zeolites (433 K, 0.1–16 kPa CH_3OH) do not show bare protons or surface methoxy intermediates, consistent with the associative mechanism [13] and suggesting that all sites are covered by methanol monomers or higher order clusters during reaction. Turnover rates (per H^+, 415 K) measured on small-pore CHA zeolites (Si/Al = 15) containing isolated H^+ sites also appear to proceed via the associative mechanism, based on analogous observations from kinetic and *in situ* IR data (0.05–20 kPa CH_3OH, 415 K) [16]. *In situ* IR spectra (0.05–20 kPa CH_3OH, 415 K) of CHA zeolites of similar composition (Si/Al = 15) containing paired H^+ sites (2 Al per 6-MR), however, show surface methoxy present at coverages that increase with the fraction of paired H^+ sites [16], suggesting that the dissociative dehydration mechanism may proceed at paired H^+ sites in CHA. Furthermore, turnover rates (per H^+) on CHA increase with the fraction of H^+ sites in paired configurations [16,17], and density functional theory (DFT) calculations suggest that interactions between proximal Brønsted acid sites may alter the stability of the deprotonated conjugate base and lead to an increase in acid strength [18]. The precise mechanistic roles of paired and isolated H^+ site ensembles in CHA, however, are convoluted by inhibition of methanol dehydration rates at high methanol pressures (415 K, >10 kPa CH_3OH) [16], a phenomenon not observed on medium-pore and large-pore zeolites [11,13].

The inhibition of certain alkanol dehydration mechanisms has been previously reported for C_2–C_4 alkanols over solid acid catalysts. Bimolecular dehydration rates of ethanol to form diethyl ether (MFI, FER, MOR; 368–409 K, >6 kPa C_2H_5OH) [19] and propanol dehydration to dipropyl ether (MFI, 413–443 K, <4 kPa C_3H_7OH) [20] asymptotically approach a zero-order dependence and are not inhibited at higher alkanol partial pressures, similar to reports of methanol dehydration rates on medium-pore and large-pore zeolites [11]. Ethanol and propanol, unlike methanol, are also able to undergo unimolecular dehydration to form the corresponding alkene. Ethanol dehydration to ethene is inhibited on MOR zeolites (368–409 K, <6 kPa C_2H_5OH) because additional ethanol molecules adsorb at ethanol monomers and must desorb prior to ethene formation transition states [19]. Similar observations have also been reported for unimolecular dehydration of propanol to propene (MFI, 413–443 K, <4 kPa C_3H_7OH) [20] and butanol to butene (W-POM/SiO_2, 343 K, <1 kPa C_4H_9OH) [21] because the coordination of a second alkanol or water forms dimeric intermediates that are spectators in alkene formation routes. These observations indicate that unimolecular alkanol dehydration to the corresponding alkene (<443 K, C_2-C_4 alkanols) is inhibited by coordination of a second alkanol molecule to form higher molecularity intermediates that behave as spectators, but that such intermediates can condense to eliminate the corresponding dialkyl ether and water at rates (<443 K, C_1-C_4 alkanols) that approach a zero-order kinetic regime at high alkanol partial pressures.

Thus, the high-pressure inhibition of bimolecular methanol dehydration rates (415 K) in small-pore CHA zeolites presents a sharp contrast to the inhibition of only unimolecular alkanol dehydration in medium-pore and large-pore zeolites, and the precise mechanistic origin of this inhibition has remained imprecisely understood. In our prior work, such high-pressure rate inhibition was accounted for by including an elementary step for the formation of an unreactive methanol trimer via quasi-equilibrated adsorption of a methanol at a protonated dimer, to derive an *ad hoc* rate equation that allowed estimating first-order and zero-order rate constants from experimentally measured rate data on CHA zeolites [16]. Here, we further investigate the formation and stability of different methanol species at isolated H^+ sites in CHA zeolites during methanol dehydration catalysis using a combination of kinetic, spectroscopic, and theoretical probes. High-pressure inhibition of methanol dehydration rates (per H^+) becomes attenuated at elevated reaction temperatures (>450 K), which coincides with the disappearance of IR vibrational bands characteristic of methanol trimers and larger clusters (~3370 cm^{-1}) detected by *in situ* IR spectroscopy (343–473 K, 10 kPa CH_3OH). Methanol adsorption isotherms indicate that the onset of dehydration rate inhibition (415 K, per H^+) occurs at coverages corresponding to >2 CH_3OH per H^+ site, consistent with IR spectra (0.01–3 CH_3OH/H^+; 293 K) that show the appearance of methanol clusters at coverages of >0.7 CH_3OH per H^+ site and that increase in intensity with increasing methanol coverage. DFT is used to calculate the Gibbs free energies of various methanol complexes (1–12 CH_3OH per proton) confined within CHA as a function of temperature and methanol pressure, which indicate that methanol trimers are preferentially stabilized in CHA at methanol pressures corresponding to the onset of kinetic inhibition observed experimentally (>10 kPa, 415 K). Apparent free energy barriers for methanol dehydration are calculated considering up to four methanol-derived species at an H^+ site, in which spectating methanol species are found to insert between reacting species and framework O atoms. DFT-predicted methanol dehydration rates (415 K) are compared with experimental data to determine plausible reaction mechanisms and highlight the critical influence of the zeolite framework on stabilizing reactive and inhibitory intermediates in methanol conversion pathways.

2. Methods and materials

2.1. Catalyst synthesis and characterization

2.1.1. Synthesis of different small-pore zeolites

The full synthesis procedure of CHA zeolites containing isolated H^+ sites is described in detail elsewhere [17]. In brief, CHA was syn-

thesized using N,N,N-trimethyl-1-adamantylammonium hydroxide as the structure directing agent (SDA) with a molar ratio in the crystallization medium of 1 SiO_2/0.033 Al_2O_3/0.5 TMAdaOH/44 H_2O. In a typical synthesis, deionized water and an aqueous solution of TMAdaOH were mixed and stirred for 15 min under ambient conditions in a perfluoroalkoxy alkane (PFA) jar. Next, aluminum hydroxide powder was added and stirred for 15 min under ambient conditions. Finally, an aqueous colloidal silica solution was added and the contents were covered and stirred for 2 h under ambient conditions. The resulting mixture was transferred to a PTFE-lined stainless-steel autoclave and heated to 433 K under rotation at 40 RPM for 6 days.

The full synthesis procedure of AEI zeolites and the organic SDA, cis-2,6-dimethylpiperidinium hydroxide (DMPOH), are described in detail elsewhere [22,23]. Briefly, AEI was synthesized using a molar composition of 1 SiO_2/0.017 Al_2O_3/0.07 DMPOH/0.58 NaOH/12.3 H_2O. The resulting solution was transferred to a PTFE-lined stainless-steel autoclave and heated to 413 K under rotation for 4 days.

LEV zeolites were synthesized following a reported procedure using a mixture of 1-adamantylamine ($AdaNH_2$) and sodium fluoride [24]. A molar ratio of 1 SiO_2/0.024 Al_2O_3/0.3 $AdaNH_2$/0.05 NaF/10 H_2O was used in the crystallization medium. In a PFA jar, 4.455 g of $AdaNH_2$ (Sigma-Aldrich, 97 wt%) were added to 17.081 g of deionized water (18.2 MΩ) and stirred until fully dissolved. 6 g of FAU zeolite (CBV720, Si/Al = 21, Zeolyst) were added and stirred for 10 min until a uniform slurry was obtained. Finally, 0.237 g of NaF (Sigma-Aldrich, 99 wt%) were added and the mixture was covered and stirred for 2 h at ambient temperature. The resulting mixture was then loaded into a 45 cm^3 PTFE-lined stainless-steel autoclave and placed in a static oven at 423 K for 10 days.

LTA zeolites and the required organic SDA, 1,2-dimethyl-3-(4-methylbenzyl)imidazolium hydroxide (DMMBI-OH) were synthesized according to previous reports [25]. The synthesis of DMMBI-Cl was carried out in a two-neck 500 cm^3 round-bottom flask attached to a water-cooled condenser to minimize solvent evaporation. In the round-bottom flask, a 0.1 M solution of 1,2-dimethylimidazole (Sigma-Aldrich, 98 wt%) was first prepared by dissolving 0.48 g of 1,2-dimethylimidazole in 50 cm^3 of chloroform (Sigma-Aldrich, 99.8 wt%) and stirring for 15 min to homogenize the contents. In a separate 100 cm^3 pear-shaped flask, a 0.1 M solution of 4-methylbenzyl chloride (Sigma-Aldrich, 98 wt%) was prepared by adding 0.70 g of 4-methylbenzyl chloride to 50 cm^3 of chloroform and stirring until homogenous. The 0.1 M solution of 4-methylbenzyl chloride was then added to the 0.1 M solution of 1,2-dimethylimidazole, the second-neck of the round-bottom flask capped with a Viton septum, and stirred for two days at 303 K. After two days, the solution was evaporated, dissolved in a minimum amount of chloroform, and then recrystallized with diethyl ether (Sigma-Aldrich, 99 wt%). A portion of the crystalline product was dissolved in D_2O (Cambridge Isotope Laboratories, 99.9%) and a ^1H NMR spectrum was recorded and was consistent with reported ^1H chemical shifts for DMMBI-Cl (details in Supp. Info.) [25]. The resulting Cl^- form of the SDA salt was then converted to its OH^- form by ion-exchange with a Dowex Marathon A (Sigma-Aldrich) using a mass ratio of 1 SDA/3 resin/5 H_2O and repeated thrice with fresh resin. A final purity of ~80% DMMBI-OH was confirmed by titration with a 0.1 M HCl solution.

The synthesis of high-silica LTA zeolites was performed using a mixture of DMMBI-OH and tetramethylammonium hydroxide (TMAOH) as the SDAs with a molar composition of 1 SiO_2/0.025 Al_2O_3/0.45 DMMBI-OH/0.05 TMAOH/0.49 HF/5 H_2O in the synthesis medium. In a PFA jar, 11.040 g of an aqueous DMMBI-OH solution (20 wt%) were added to 0.233 g of an aqueous TMAOH solution (Sigma-Aldrich, 25 wt%) and stirred for five minutes. Next, 0.032 g of $Al(OH)_3$ powder (SPI Pharma) were added to the SDA solution and stirred until fully dissolved. 1.746 g of tetraethylorthosilicate (TEOS, Sigma-Aldrich, 98 wt%) were then added and the resulting mixture was capped and stirred for two hours under ambient conditions. After two hours, the mixture was uncapped and excess water and ethanol, formed upon hydrolysis of TEOS, was allowed to evaporate under ambient conditions until the target H_2O/SiO_2 ratio was obtained. 5 g of additional water were then added and the mixture was again dehydrated to reach the target H_2O/SiO_2 ratio. After this second dehydration step, 0.160 g of hydrofluoric acid (Sigma-Aldrich, 48 wt%, 99.999% trace metals basis) were added dropwise and stirred with a PTFE spatula for 15 min. The synthesis mixture was then transferred to a 23 cm^3 PTFE-lined stainless-steel autoclave and heated to 448 K under rotation (60 RPM) for 7 days.

After crystallization of each zeolite, the solid products were washed repeatedly with acetone (Sigma-Aldrich, 99.9 wt%) and deionized water (35 cm^3 g_{cat}^{-1}) until the pH of the supernatant remained constant between washes, recovered via centrifugation, and dried at 373 K overnight under stagnant air. The dried, as-synthesized zeolites were then heated to 853 K (0.0167 K s^{-1}) under flowing air (1.67 cm^3 g_{cat}^{-1} s^{-1}) for 10 h to remove the occluded organic SDA.

2.1.1.1. ^1H NMR of 1,2-Dimethyl-3-(4-methylbenzyl)imidazolium chloride. After crystallization of DMMBI-Cl, approximately 0.5 g of the recovered solid were dissolved in 0.5 cm^3 of D_2O and a portion of this solution was placed inside an NMR tube (Wilmad LabGlass, 5 mm thin wall, 7 in., 500 MHz) for ^1H NMR analysis. NMR spectra were collected on a Bruker ARX500 spectrometer equipped with a 5 mm BBFO Z-gradient probe at ambient temperature and represent the average of 128 scans. The measured spectrum is shown in Fig. S.9 of the Supp. Info. ^1H NMR (D_2O, 500 MHz): δ 7.31 (s, 2H), 7.27 (d, 2H), 7.18 (d, 2H), 5.27 (s, 2H), 3.74 (s, 3H), 2.54 (s, 3H), 2.31 (s, 3H).

2.1.2. Structural characterization of zeolite topology and porosity

The crystal topology of all synthesized zeolites was determined from powder X-ray diffraction (XRD) patterns measured on a Rigaku Smartlab X-ray diffractometer equipped with a Cu Kα radiation source (λ = 0.154 nm) operated at 1.76 kW. Samples were loaded onto zero-background sample holders (Rigaku) and pressed flat using a microscope slide prior to collecting diffraction patterns from 2θ = 4–40° at a rate of 0.04° s^{-1} and a step size of 0.01°. Crystal topologies were confirmed by comparison of experimental diffraction patterns with those reported in the International Zeolite Association (IZA) structure database [26]. XRD patterns are shown in Fig. S.10 of the Supp. Info.

Zeolite micropore volumes were determined from Ar adsorption isotherms measured in a liquid Ar bath (87 K) on a Micromeritics ASAP 2020 Surface Area and Porosity Analyzer. Typically, 0.03–0.05 g of sieved zeolite (nominal diameter of 180–250 μm) were degassed by first heating to 393 K (0.167 K s^{-1}) under vacuum (<5 × 10^{-6} torr) for 2 h before further heating to 623 K (0.167 K s^{-1}) under vacuum (<5 × 10^{-6} torr) and holding for 9 h. The volume of gas adsorbed (cm^3 g_{cat}^{-1} at STP) was estimated from a semi-log derivative plot of the adsorption isotherm ($\partial(V_{ads})/\partial(\ln(P/P_0))$ vs. $\ln(P/P_0)$). Ar adsorption isotherms are shown in Fig. S.11 and micropore volumes are tabulated in Table S.1 of the Supp. Info.

2.1.3. Elemental analysis and titration of H^+ sites using NH_3

Total Al and H^+ site contents are tabulated in Table S.1 of the Supp. Info. The total Al content of each zeolite was determined from atomic absorption spectroscopy (AAS) using a Perkin Elmer AAnalyst 300 Atomic Absorption Spectrometer. After removal of

occluded organic SDA molecules by oxidative treatment (853 K, 10 h), zeolite samples (~0.02 g) were digested in 3 g of HF acid (48 wt%, Sigma Aldrich) overnight (at least 8 h) and then diluted with 50 g of deionized water (18.2 MΩ). Aqueous solutions were nebulized into an acetylene/nitrous oxide flame and Al absorbances were measured at a wavelength of 309.3 nm. Al concentrations were determined from calibration curves generated from solutions of known composition prepared by dilution of a 1000 ppm Al standard (Sigma-Aldrich, TraceCERT).

The number of H^+ sites on each zeolite catalyst was measured by temperature programmed desorption (TPD) of NH_3 using reported procedures [27]. After organic removal, zeolite samples were exposed to a 1 M aqueous NH_4NO_3 (Sigma-Aldrich, 99 wt%) solution (150 cm^3 g_{cat}^{-1}) and stirred under ambient conditions for 24 h. Solids were then washed six times with deionized water (35 cm^3 g_{cat}^{-1}), recovered via centrifugation, and dried overnight at 373 K under stagnant air. NH_4-exchanged zeolite samples were then pelletized and sieved (nominal diameter of 180–250 μm) and suspended between two quartz wool plugs in a quartz U-tube reactor. The quartz reactor was then loaded into a Micromeritics Autochem II 2920 Chemisorption analyzer and heated to 873 K (0.167 K s^{-1}) under flowing He (50 cm^3 g_{cat}^{-1} s^{-1}, 99.999%, Indiana Oxygen). The total amount of NH_3 desorbed was then quantified using an Agilent 5973 N mass selective detector (MSD).

2.2. Methanol dehydration kinetics and reactor configuration

Methanol dehydration kinetics were measured in a tubular packed-bed quartz reactor (7 mm inner diameter) with plug-flow hydrodynamics as described previously [16]. Zeolite samples were pelleted and sieved (nominal diameter between 180 and 250 μm) and supported between two quartz wool plugs in the reactor. The total amount of catalyst loaded into the reactor was varied between 0.005 and 0.030 g to maintain differential conversions. The total mass of zeolite charged to the reactor was maintained at a minimum of 0.025 g by dilution with Si-CHA. Dilutions (2–10 × dilution ratio) were prepared by grinding together both powders in a mortar and pestle, pelletizing, and then crushing to retain particles between 180 and 250 μm. Reactors were placed inside a three-zone furnace (Series 3210, Applied Test Systems) with a K-type thermocouple placed in direct contact with the external surface of reactor at the center of the catalyst bed and the temperature of the catalyst bed was controlled by Watlow controllers (EZ-Zone Series). Prior to contact with reactant mixtures, zeolite catalysts were heated to 773 K (0.033 K s^{-1}) and held for 4 h under a 5% O_2/He flow (50 cm^3 g_{cat}^{-1} s^{-1}, 99.999%, Indiana Oxygen). Upon cooling to the desired reaction temperature, samples were flushed with He (150 cm^3 g_{cat}^{-1} s^{-1}, 99.999%, Indiana Oxygen) for 0.5 h to remove residual O_2. Methanol (99.9 wt%, Sigma-Aldrich) was introduced into the He gas stream using a syringe pump (Legato 100, KD Scientific) and sent to the reactor through heated stainless-steel lines maintained at > 373 K using resistive heating tape (Brisk Heat Co.) and insulating wrap. Concentrations of reactants and products were measured using an Agilent 6890 gas chromatograph equipped with a flame ionization detector and an HP Plot-Q column (0.53 mm ID × 30 m × 40 μm film, Agilent). Methane (25% CH_4/Ar, 99.999%, Indiana Oxygen) was used as an internal standard and introduced into the reactor effluent at a constant rate (0.083 cm^3 s^{-1}).

Apparent first-order and zero-order methanol dehydration free energy barriers were measured on CHA zeolites with isolated H^+ sites from DME formation rates (per H^+) measured as a function of methanol pressure (0.05–50 kPa) at temperatures varied non-systematically between 383 and 415 K. Apparent first and zero-order methanol dehydration rate constants (per H^+) were determined from a least squares regression of Eq. (4) to the rate data and the Eyring-Polanyi equation was used to extract first and zero-order apparent activation enthalpies and entropies. These data and calculations are shown in Section S.10 of the Supp. Info.

2.3. Measurement of IR spectra

2.3.1. Steady-state methanol dehydration

IR spectra collected under steady-state methanol dehydration catalysis were measured on a Nicolet 4700 spectrometer with an HgCdTe detector (MCT, cooled to 77 K by liquid N_2). Spectra were collected between 4000 and 400 cm^{-1} and averaged over 64 scans at a 2 cm^{-1} resolution and referenced to an empty cell background collected under He flow (0.33 cm^3 s^{-1}, 99.999%, Indiana Oxygen) at 415 K. Zeolite catalysts were pressed into self-supporting wafers (0.01–0.02 g_{cat} cm^{-2}) and placed within a custom-built quartz IR cell sealed with CaF_2 windows [16,28,29]. Temperatures were measured by K-type thermocouples (Omega) held ~2 mm from each side of the zeolite wafer. Prior to each measurement, the zeolite wafer was heated to 773 K (0.083 K s^{-1}) for 4 h under flowing air (13.3 cm^3 g_{cat}^{-1} s^{-1}) purified by a purge gas generator (Parker Balston, <1 ppm of CO_2, 200 K H_2O dew point), and then cooled under flowing He (13.3 cm^3 g_{cat}^{-1} s^{-1}) to the analysis temperature. Methanol (Sigma-Aldrich, 99.9 wt%) was introduced to the quartz IR cell (0.1–22 kPa) by a syringe pump (Legato 100, KD Scientific) connected to stainless-steel transfer lines maintained >353 K using resistive heating tape (Brisk Heat Co.) and insulating wrap. IR spectra were recorded as a function of time until peak intensities remained constant for >0.25 h. All spectra were baseline corrected and normalized to the zeolite combination and overtone T-O-T vibrational modes (1750–2100 cm^{-1}) of the freshly dehydrated zeolite spectrum.

2.3.2. IR spectra measured at known methanol coverages

Methanol adsorption isotherms were measured on the same IR apparatus as described in Section 2.3.1, except a custom-built glass vacuum manifold was used to introduce small amounts (<1 torr doses) of methanol onto dehydrated CHA zeolites [28,29]. IR spectra taken during methanol adsorption isotherms were referenced to an empty cell background taken under dynamic vacuum at 293 K. Prior to methanol dosing experiments, zeolite self-supporting wafers were heated to 773 K (0.083 K s^{-1}) under dynamic vacuum (<0.1 torr) for 2 h before cooling to room temperature. The adsorption temperature was maintained below room temperature (293 K) using a closed-loop chiller that recirculated chilled water (288 K) through cooling coils encircling the quartz IR cell [28]. Methanol was loaded into a glass ampule (1/4″ OD) and purified on the vacuum manifold via successive freeze-pump-thaw cycles until dissolved gases were no longer observed bubbling out upon thawing. Zeolite samples were exposed to small amounts of methanol (2.5×10^{-7} mol per dose) and allowed to equilibrate for two minutes prior to measurement of an IR spectrum. Methanol coverages were calculated as the total number of moles of methanol that disappeared from the gas phase during each dose by taking the difference in the initial and final number of moles in the gas phase.

2.4. Measurement of methanol adsorption isotherms

High-resolution methanol adsorption isotherms were measured at 293 K using the same gas adsorption apparatus as described in Section 2.1.2. Methanol adsorbates (Sigma-Aldrich, 99.9%) were degassed by successive freeze-pump-thaw cycles and supplied at their respective vapor pressures at 293 K. Adequate resolution at low pressures was achieved by holding samples under dynamic vacuum (<5×10^{-6} torr) on the analysis port during the prepara-

tion sequence until the dosing manifold was charged with adsorbate prior to collection of the first data point. Methanol was then dosed onto the evacuated zeolite sample in equilibrated increments of 1 $cm^3\ g^{-1}$ (gas volume adsorbed at STP per gram) until a final relative pressure of $P\ P_0^{-1} = 0.6$ was reached. This procedure was previously found necessary for obtaining accurate ethanol and water adsorption isotherms on siliceous BEA zeolites [30]. The full adsorption isotherm is shown in Fig. S.16 in the Supp. Info.

2.5. Computational methods

Fully periodic density functional theory (DFT) calculations were performed using the Vienna ab initio software package (VASP) [31–34] and implemented in the Computational Catalysis Interface (CCI) [35]. Planewaves were constructed using the projector augmented wave method (PAW) with an energy cutoff of 400 eV [36,37]. The Brillouin zone was sampled at the Γ-point for all calculations. The Perdew-Burke-Ernzerhof (PBE) form of the generalized gradient approximation (GGA) was used for all calculations [38]. Dispersive interactions were accounted for by including the DFT-D3 empirical correction with Becke and Johnson damping (D3BJ) [39,40]. Structures were optimized in two steps to improve computational efficiency. Structures were optimized in the first step using a wavefunction convergence criteria such that energy variations between iterations were $<10^{-4}$ eV and forces were computed with a fast Fourier transform (FFT) grid of 1.5 × the energy cutoff (PREC = .NORMAL. in VASP); structures were relaxed until the maximum force on any atom was <0.05 eV $Å^{-1}$. These settings may result in inaccurate forces near the minimum; as such, structures are then re-optimized with wavefunctions converged to within 10^{-6} eV and forces computed with an FFT grid 2× the energy cutoff (PREC = .ACCURATE. in VASP). This two-step optimization scheme has been shown to increase computational efficiency by a factor of ~3 for zeolite-based calculations that are sampled at the Γ point [35].

Transition state searches were initiated using the nudged elastic band (NEB) method with 16 intermediate images for each elementary step and converged such that the forces on each atom were <0.5 eV $Å^{-1}$ [41,42]. Transition states were then refined starting from these NEB results using the Dimer method [43], where structures were converged using the same criteria as those used for optimizations (energy variation between iterations $<10^{-6}$ eV, max force per atom <0.05 eV $Å^{-1}$).

The CHA structure was obtained from the database of the international zeolite association (IZA), with unit cell parameters $a = b = 13.675$ Å, $c = 14.767$ Å, $\alpha = \beta = 90.0°$, and $\gamma = 120.0°$ [26]. The CHA structure is comprised of stacked six-member ring (6-MR) structures with adjacent eight-member ring (8-MR) windows leading into larger cage voids. CHA has one symmetrically unique T-site surrounded by four unique O atoms. One of the 36 Si atoms in the CHA unit cell was replaced by an Al atom (Si/Al = 35) and balanced by a proton to form a Brønsted acid site (Fig. S.1, Supporting Information). Previous work has shown that protons associated with Brønsted acid sites prefer to bind to O1 or O4 atoms and are solvated by 6-MR or 8-MR motifs [18,44].

Zeolites are flexible materials and are prone to restructuring during DFT calculations, as recently emphasized for the MFI framework [45]. Therefore, the unit cell parameters of the CHA unit cell were optimized with an energy cutoff of 800 eV without constraints (ISIF = 3 in VASP) to ensure that these initial unit cell parameters would not result in restructuring. These unit cell parameter optimizations yielded a <1% change in each unit cell parameter; therefore, the initial IZA structure was used in all subsequent calculations. Furthermore, annealing of the CHA structure was simulated with *ab initio* molecular dynamics (AIMD) in VASP to confirm that restructuring does not occur with the PBE exchange-correlation functional and D3BJ correction. The CHA structure was heated from 200 K to 800 K over 3 ps, held at 800 K for 3 ps, and cooled from 800 K to 100 K over 15 ps, each with a timestep of 3 fs. The resulting annealed CHA structure was subsequently optimized using the same convergence criteria described above. This annealed and optimized CHA structure differed by <1 kJ mol^{-1} in energy from the directly optimized CHA structure from the IZA database. Moreover, the two structures differed by a negligible distance. These negligible changes in energy and structure indicate that the CHA structure supplied by IZA is sufficiently stable for kinetic studies.

Vibrational frequency calculations were used to approximate zero-point vibrational energies (ZPVEs), vibrational, rotational, and translational enthalpies (H) and free energies (G) using a fixed displacement method (n = 2) for all gas-phase and adsorbed species. Framework Si and O atoms that were not bound to the Al atom were fixed during frequency calculations within the zeolite framework. These values were used to approximate total enthalpies in conjunction with VASP-derived electronic energies (E_0):

$$H = E_0 + ZPVE + H_{vib} + H_{rot} + H_{trans} \quad (1)$$

and free energies

$$G = E_0 + ZPVE + G_{vib} + G_{rot} + G_{trans} \quad (2)$$

at 415 K and 1 bar CH_3OH (standard pressure), the formulas for which are derived from statistical mechanics formalisms (see Section S.1 in the Supp. Info. for details) [46]. All motions for guest species within the zeolite framework are considered vibrations, such that translational and rotational H and G are zero for non-gas phase species, which are treated as ideal gases with appropriate equations from statistical mechanics. Enthalpies and entropies (S) derived from calculations were used to predict equilibrium constants of adsorption (K) from 300 to 500 K, in order to predict adsorption behavior of methanol in CHA and to predict equilibrium and rate constants for DFT-predicted rates. Low-frequency vibrational modes disproportionately contribute to entropy estimates; as such, frequencies below 60 cm^{-1} were replaced by 60 cm^{-1} (with the exception of the negative frequency in transition states), as in previous work [47,48].

The diverse confining voids within single zeolite frameworks affect the energies of guest species differently depending on the orientation and location of those species [48–50]. Therefore, a systematic method of probing the configurational space of zeolites is critical to find favorable configurations of these intermediates [48]. Here, we perform systematic reorientations on adsorbates and transition states interacting with each O atom of the CHA framework to ensure comprehensive probing of the confining space of the CHA voids. Adsorbates and transition states that strongly interact with framework O atoms (e.g., surface methoxy, transition states forming or breaking C–O bonds, and species H-bonding) were (1) reoriented about the axis formed by the Si and Al bound to the O atom; (2) rotated about their interactions with the framework O above the acid site by changing the adsorbate–O dihedral angle; and (3) moved by altering the angle between the Al, O, and adsorbate. Transition states were rotated about internal bonds and incipient bonds and adsorbates that did not interact strongly with the surrounding framework were rotated about the x-, y-, and z-axes (the y- and z-axes are the same as the b- and c-vectors of the CHA unit cell, respectively). These reorientations yielded structures with large ranges of energies, while preserving strong interactions with the surrounding framework. This further indicates that there are diverse void environments around a single acid site within a zeolite framework, which can be probed using these systematic reorientations [48].

3. Results and discussion

3.1. Inhibition of methanol dehydration rates on small-pore zeolites

Methanol dehydration turnover rates (415 K, per H^+) on CHA zeolites containing predominantly isolated H^+ sites increase linearly with methanol partial pressure (P_{CH3OH}) at low partial pressures (<1 kPa), before reaching a maximum and transitioning to a kinetic regime reflecting inhibition at high partial pressures (>10 kPa) (Fig. 1). This behavior is not captured by the form of the associative dehydration rate law derived assuming H^+ sites are covered by methanol monomers and protonated dimers as most abundant surface intermediates (MASI) (Eq. (3)) [10].

$$r_A = \frac{k_{DME,A} K_D P_{CH_3OH}}{1 + K_D P_{CH_3OH}} \quad (3)$$

In Eq. (3), $k_{DME,A}$ is the rate constant for DME formation via the associative mechanism, K_D is the equilibrium constant for forming a protonated dimer from a gaseous methanol and adsorbed methanol monomer, and P_{CH3OH} is partial pressure of methanol. *In situ* IR spectra measured under conditions of methanol dehydration catalysis (415 K, 0.05–20 kPa) detected methanol monomers (~2400 cm^{-1}) and dimers (~2600 cm^{-1}) [13], and vibrational modes for methanol clusters (~3370 cm^{-1}) [51] at high methanol partial pressures (>10 kPa) [16]. Including methanol trimers as a MASI introduces a second-order methanol pressure term in the denominator of the associative dehydration rate law (Eq. (4)), which is able to describe the rate inhibition measured at high methanol partial pressures (Fig. 1, solid line) [16].

$$r_A = \frac{k_{DME,A} K_D P_{CH_3OH}}{1 + K_D P_{CH_3OH} + K_I K_D P_{CH_3OH}^2} \quad (4)$$

In Eq. (4), K_I is the equilibrium constant for forming a methanol trimer from a gaseous methanol and adsorbed protonated dimer. Before using Eq. (4) to describe methanol dehydration rates on CHA zeolites, we first examine and discard other mechanistic assumptions that would also predict high-pressure kinetic inhibition, by considering other plausible intermediates and rate laws derived from the dissociative mechanism that do not consider surface methoxy as a MASI, since such species are not detected by *in situ* IR spectra of CHA zeolites (Si/Al = 15) containing isolated H^+ sites [16].

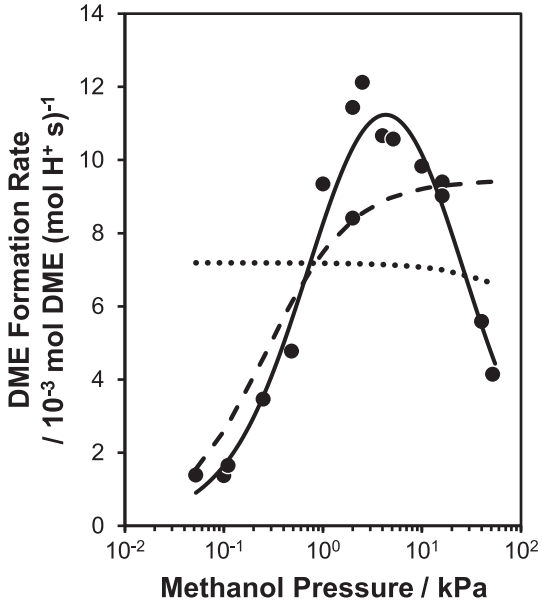

Fig. 1. Least-squares regressions of Eq. (4) (solid line), Eq. (6) (dotted line), and Eq. (7) (dashed line) to experimentally measured methanol dehydration rates (per H^+, 415 K) on a H-CHA (Si/Al = 15) sample containing predominantly isolated H^+ sites.

An alternate rate law can be derived for the dissociative mechanism, assuming methanol monomer dehydration to form methoxy intermediates is the kinetically relevant step, and that H^+ sites, methanol monomers, and protonated dimers are the MASI (r_{D1}; derivation in Section S.13.1 of the Supp. Info.):

$$r_{D1} = \frac{k_{Me} K_M P_{CH_3OH}}{1 + K_M P_{CH_3OH} + K_M K_D P_{CH_3OH}^2} \quad (5)$$

In Eq. (5), k_{Me} is the methoxy formation rate constant, and K_M is the equilibrium constant for forming a methanol monomer from a gaseous methanol and a vacant H^+ site. This expression predicts inhibition at high methanol partial pressures because protonated dimers are spectator species in the dissociative mechanism (Scheme 1). This rate expression would require vacant H^+ sites to be a MASI, however, which is inconsistent with *in situ* IR spectra that show complete perturbation of bridging OH stretching vibrations (~3608 cm^{-1}) by adsorbates at low methanol partial pressures corresponding to the first-order kinetic regime (<1 kPa CH_3OH, 415 K) [16]. The removal of vacant H^+ sites as a MASI causes Eq. (5) to predict between zero-order and negative-order dependences on methanol pressure, resulting in a rate law (Eq. (6)) that does not describe the first-order dependence of methanol dehydration rates at low pressures (Fig. 1, dotted line):

$$r_{D1} = \frac{k_{Me}}{1 + K_D P_{CH_3OH}} \quad (6)$$

Another alternative rate law can be derived from the dissociative mechanism, assuming DME formation is the kinetically relevant step and all preceding steps are quasi-equilibrated, and that methanol monomers and protonated dimers are the MASI, in accordance with *in situ* IR spectra measured on CHA zeolites (Si/Al = 15) containing isolated H^+ sites [16] (r_{D2}; derivation in Section S.13.2 in the Supp. Info.):

$$r_{D2} = \frac{k_{DME,D} K_{MMe} K_{Me} P_{CH_3OH} P_{H_2O}^{-1}}{1 + K_D P_{CH_3OH}} \quad (7)$$

In Eq. (7), $k_{DME,D}$ is the DME formation rate constant for the dissociative mechanism, K_{MMe} is the equilibrium constant for forming a methoxy-methanol pair from a surface methoxy and gaseous methanol, and P_{H2O} is the gas-phase partial pressure of water, which is generated via methanol monomer dehydration to form a surface methoxy. This rate law predicts a first-order kinetic regime at low methanol pressures and a transition to a zero-order kinetic regime at higher pressures, but also predicts rate inhibition caused by hydration of surface methoxy intermediates. Eq. (7) was regressed to methanol dehydration rates (per H^+, 415 K) measured on CHA zeolites containing isolated H^+ sites, assuming that the gaseous water partial pressure is equal to that of DME formed from reaction (Fig. 1, dashed line). The high-pressure inhibition observed experimentally causes methanol conversion to decrease (Fig. 2a) faster than Eq. (7) would predict, indicating that the product water formed via methanol dehydration is unable to account for the measured inhibition (Fig. 1, dashed line). Moreover, methanol dehydration rates do not depend on space velocity at fixed methanol pressure (per H^+, 1 kPa CH_3OH, 5–30% conv.; Fig. 2b), as would be predicted by Eq. (7) because of the inverse dependence of methanol dehydration rates on water pressure (solid line, Fig. 2b; derivation in Section S.12 of Supp. Info.). Methanol dehydration rates (415 K, per H^+) were also measured after treating methanol reactants to remove any residual moisture and contaminants (purification procedure in Section S.4, Supp. Info.), and were

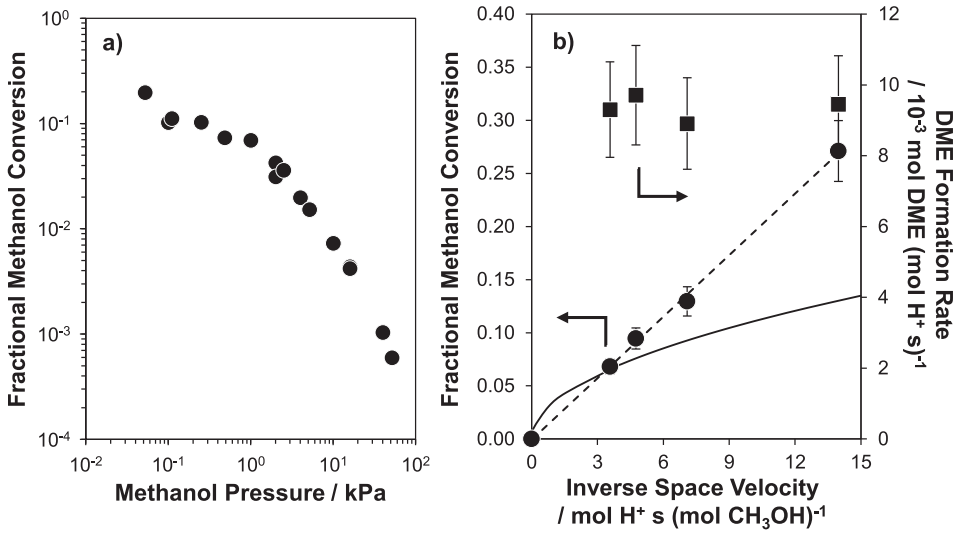

Fig. 2. (a) Fractional methanol conversion (415 K) on a H-CHA (Si/Al = 15) sample with isolated H^+ sites as a function of methanol pressure, and (b) fractional methanol conversion (circles) and DME formation rates (per H^+, 415 K; squares) along with the predicted dependence from Eq. (7) (solid line, derivation in Section S.12 of Supp. Info.) as a function of inverse space velocity.

identical to those measured using unpurified methanol (Fig. S.9, Supp. Info.). Thus, any adventitious water present in the reactant methanol feed, or generated *in situ* as a reaction product, is not responsible for the observed inhibition at high methanol pressures.

3.2. DFT assessments of prevalent methanol dehydration reaction pathways

Prior to interpreting the mechanistic origin of high-pressure inhibition of methanol dehydration rates, we first use DFT to predict the free energy landscapes (Fig. 3) of both the associative and dissociative mechanism at isolated H^+ sites in CHA (1 bar, 415 K). For the associative mechanism, DME formation from a protonated dimer intermediate is the kinetically relevant (i.e., rate-determining) step, and DFT estimates a zero-order free energy barrier ($\Delta G_{zero} = \Delta G_{\ddagger} - \Delta G_{dimer}$) of 137 kJ mol^{-1} and first-order free energy barrier ($\Delta G_{first} = \Delta G_{\ddagger} - \Delta G_{monomer} - \Delta G_{CH3OH,g}$) of 123 kJ mol^{-1} (Fig. 3). For the dissociative mechanism, the first step methylates the zeolite surface with an intrinsic and overall barrier of 135 kJ mol^{-1}, while the second step involves methylating methanol to form DME with an intrinsic barrier of 77 kJ mol^{-1} and an overall barrier of 130 kJ mol^{-1} (Fig. 3). Either of these steps could be kinetically relevant should DME form via the dissociative mechanism. Therefore, the kinetic fates of surface methoxy intermediates were determined by calculating ratio of the reverse rate of the first step (r_{-D1}) to the forward rate of the second step (r_{D2}) as a function of conversion (details in Section S.3 in Supp. Info.). The forward rate of the second step is >10× faster than the reverse rate of the first step below 30% conversion, corresponding to the highest value tested in this work (Fig. S.7, Supp. Info.), and thus the first step is kinetically relevant at these conditions.

The reaction coordinate diagram in Fig. 3 was constructed after carefully examining each intermediate and transition state structure to identify their most stable configurations, using systematic reorientations of initially converged structures to more comprehensively probe the configurational space accessible within zeolite voids [48]. The first step of the dissociative mechanism involves surface methylation transition states that are stabilized by 8-MR structures, in which H atoms of hydroxyl groups form H-bonds to lattice O atoms (Fig. 4a). Surface methylation transition states preferentially interact with O3 of the conjugate base and form two H-bonds to O atoms in the 8-MR, in which O3 is located

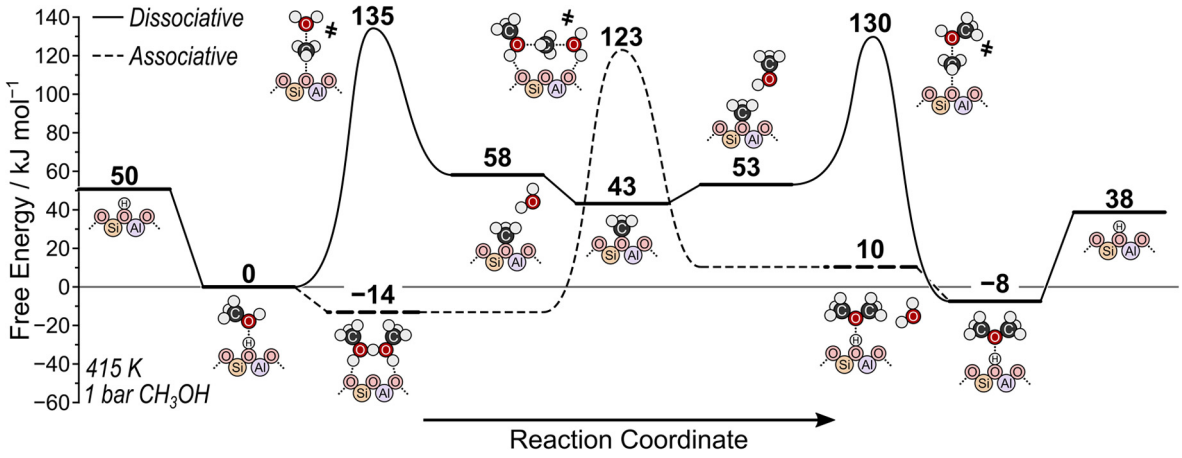

Fig. 3. Reaction coordinate diagram showing DFT-calculated free energies (ΔG; kJ mol^{-1}) of intermediates and transition states involved in methanol dehydration on isolated H^+ sites in CHA at 415 K and 1 bar of CH_3OH.

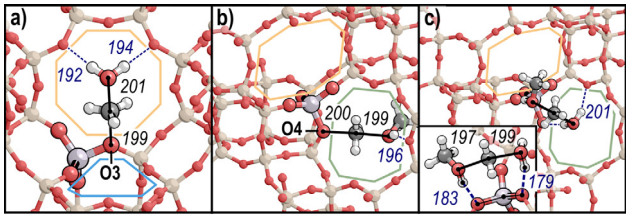

	a)	b)	c)
ΔG_{app}	135	130	123
ΔH_{app}	129	121	51
ΔS_{app}	−14	−22	−174
ΔG_{int}	135	78	137

Fig. 4. The most favorable transition state found in CHA for (a) surface methylation (the first step of the dissociative mechanism), (b) methanol methylation (the second step of the dissociative mechanism), and (c) associative dimethyl ether formation. The framework O atom with which the methyl group interacts in (a) and (b) is labeled. Incipient bonds (black) and H-bonds (navy) are labeled in pm. Apparent (ΔG_{app}) and intrinsic free energy (ΔG_{int}) and apparent enthalpy (ΔH_{app}) barriers in kJ mol^{-1}, and apparent entropies (ΔS_{app}) in J mol^{-1} K^{-1}, are shown relative to an adsorbed methanol. The 8-MR (orange, green) and 6-MR (light blue) adjacent to each transition state are highlighted.

(192 and 194 pm, Fig. 4a). The most favorable surface methylation transition states at O4 and O2, which are also in 8-MR, are 13 and 18 kJ mol^{-1} higher in energy, respectively, indicating the strong preference for the transition state geometry at O3 for surface methylation (Fig. S.2 in the Supp. Info.). The transition state at O1 is 38 kJ mol^{-1} higher in energy than that at O3, as this transition state is not solvated by surrounding framework atoms (Fig. S.2 in the Supp. Info.), because it is instead located in the larger CHA cage void, which confers weaker dispersive stabilization.

The second step of the dissociative mechanism, in which another methanol accepts the surface methyl group, also occurs most easily in the 8-MR; however, this transition state forms preferentially at O4 of the conjugate base rather than at O3 (Fig. 4b). The methanol that accepts the surface methyl group forms one H-bond to another O atom in the 8-MR that contains O4 of the active site. The reacting oxygenate species (CH_3OH) contains only one polar O—H bond instead of two (H_2O), resulting in less H-bonding capacity in this transition state than in the other two possible transition states that occur during methanol dehydration (Fig. 4). Moreover, this H-bond is longer (196 pm; Fig. 4b) and weaker than the H-bonds formed in surface methylation (192 and 194 pm; Fig. 4a) and associative DME formation (179 and 201 pm; Fig. 4c) transition states.

The associative transition state (Fig. 4c) is stabilized by 8-MR structures similarly to surface methylation transition states (Fig. 4a). The water leaving group in this transition state forms two H-bonds to framework O atoms in the 8-MR, one of which is O4 of the conjugate base and stabilizes partial charges of the transition state structure. Furthermore, the methanol that accepts the methyl group forms another H-bond to O3 of the conjugate base, again stabilizing the transition state and allowing for rapid surface protonation after DME is formed. These concerted H-bonding motifs form a ring of interactions as the methyl group is transferred from one oxygenate to another (Fig. 4c, inset), allowing for more effective charge distribution than is possible in either of the dissociative transition states. Moreover, H-bonding in the associative transition state occurs predominantly with O atoms of the conjugate base, which harbor more negative partial charge, resulting in shorter (181 pm on average in Fig. 4c; 193 and 196 pm in Fig. 4) and stronger stabilizing interactions between reacting species and the zeolite surface.

Maximum rate analysis was then used to predict rates of competing reaction pathways using these DFT-predicted free energy barriers, which are taken together with statistical mechanics formalisms (see Section S.1 of the Supp. Info. for relevant formulas) to calculate rate (k_i) and equilibrium constants (K_i), as described in previous work [48,52]. The overall rate of a reaction pathway is taken as the rate of the slowest elementary step, identified from rates calculated by separately considering each elementary step to be the sole rate-limiting step. The fastest overall rates among different competing reaction pathways are used to identify prevailing reaction routes. Although the associative route occurs with an overall barrier 12 kJ mol^{-1} lower than that of the dissociative route at 415 K (123 kJ mol^{-1} overall; Fig. 3), the resulting larger rate constant does not account for pressure effects on rates, requiring maximum rate analysis to assess competing dehydration pathways.

The results of maximum rate analysis at 415 K and 0.1% conversion are shown in Fig. 5, with rates of the associative pathway and of the first and second steps of the dissociative pathway shown as a function of methanol pressure. The second step of the dissociative pathway occurs at faster rates than the associative mechanism at all pressures considered here (0.01–100 kPa) (Fig. 5), consistent with analysis of the reversibility of the first step that indicates it is the sole kinetically relevant step of the dissociative mechanism (Section S.3, Supp. Info.). The dissociative pathway dominates at pressures below 4 kPa at 415 K, which reflects the relative pressure dependences of rates for the associative and dissociative routes:

$$\frac{r_{D1}}{r_A} = \frac{k_{D1}}{k_A K_D P_{CH_3OH}} \tag{8}$$

This equation indicates that the dissociative route will dominate at sufficiently low methanol pressures, and that the prevailing reaction mechanism will shift to the associative route at higher pressures. Rates estimated by DFT predict this transition occurs at 4, 10, 23, and 63 kPa at 415, 433, 450, and 473 K, respectively (Fig. S.6b). This shift reflects entropic and enthalpic preferences for these routes, in which the adsorption of a second methanol in the associative route confers enthalpic gains but concomitant entropic losses that preferentially benefit the dissociative mechanism at high temperatures and low pressures. This is consistent

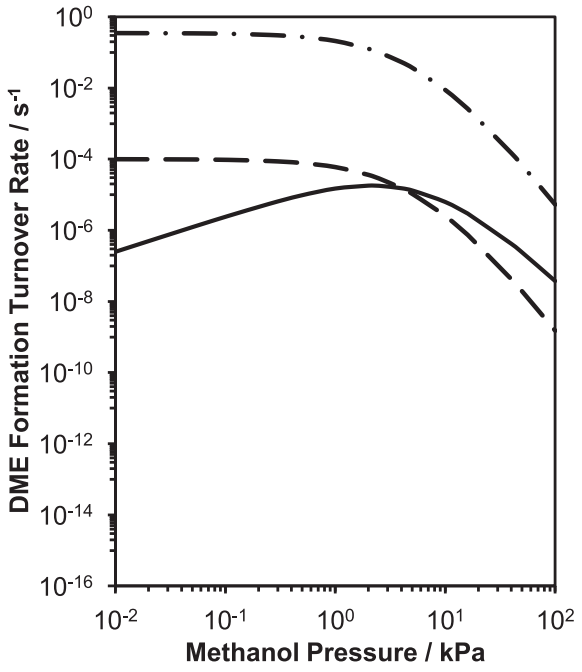

Fig. 5. DFT-predicted rates (415 K) for kinetically-relevant methoxy (dashed line) and DME (dashed-dotted line) formation steps of the dissociative mechanism, and for the associative mechanism (solid line) at 0.1% CH_3OH conversion.

with prior work on MFI zeolites [12,13,15] and POM catalysts [10], which indicate similar behavior for these mechanisms with different kinetic conditions.

3.3. Generality of high-pressure kinetic inhibition on small-pore zeolites and its dependence on temperature

Taken together, the experimental data in Section 3.1 provide strong evidence that methanol dehydration proceeds via the associative dehydration mechanism at isolated H^+ sites in CHA zeolites. These findings are consistent with previous investigations of methanol dehydration on microporous (medium-pore, large-pore) and mesoporous solid Brønsted acid catalysts that have compared both dehydration mechanisms under conditions where sites are covered by methanol monomers and dimers (433 K, 0.2–16 kPa CH_3OH) [10,12,13,53,54]. In Section 3.2, the DFT-calculated free energy barriers (415 K) on isolated H^+ sites in CHA zeolites in both the first-order and zero-order regime for the associative mechanism show closer agreement with values measured experimentally (Table 1). Moreover, maximum rate analysis indicates that the associative mechanism prevails at sufficiently high methanol pressures (>4 kPa) in CHA containing only isolated H^+ sites.

We next experimentally probed whether high-pressure inhibition is a general feature of small-pore microporous acids, given that such high-pressure inhibition of methanol dehydration rates was also observed in our prior studies of CHA zeolites with different fractions of paired H^+ sites [16]. Methanol dehydration rates (415 K, per H^+) were measured as a function of methanol pressure on other small-pore zeolite frameworks including AEI, LEV, and LTA, and the data are shown in Fig. 6. Methanol dehydration rates on all small-pore zeolites show a first-order kinetic regime at low methanol pressures, before reaching a maximum and then decreasing with increasing methanol pressure. These data suggest that small-pore zeolite framework topologies, in general, assist in stabilizing inhibitory methanol species at sufficiently high methanol partial pressures.

CHA zeolites (Si/Al = 15) containing predominantly isolated H^+ sites were chosen as representative samples to further study the mechanistic origin of the high-pressure inhibition of methanol dehydration rates in small-pore zeolites. High-pressure inhibition becomes attenuated in CHA containing only isolated H^+ sites (Fig. 7a), and in CHA containing paired H^+ sites (Fig. S.15, Supp. Info.), with increasing reaction temperature (398–473 K). This behavior is inconsistent with that expected if inhibition were to reflect intracrystalline transport restrictions of larger DME products, which would cause inhibition to become more severe with increasing temperature. Light olefins (e.g., ethene and propene) were observed in the reactor effluent at low methanol partial pressures at temperatures >433 K, and decreased in concentration with increasing methanol partial pressures, consistent with previous reports of methanol-to-olefins in H-MFI (623 K) [4]. First-order rate constants (per H^+), extracted from linear regression of Eq. (3) to the data in Fig. 7a, initially increase exponentially with temperature (398–415 K), but begin to deviate from this exponential dependence at elevated temperatures (433–473 K; Fig. 7b), in part reflecting scavenging of C_1 intermediates and DME products to produce olefins under first-order methanol dehydration conditions (<1 kPa). In contrast, zero-order rate constants (per H^+) increase exponentially with temperature in the range studied (398–473 K), suggesting that any olefin formation does not significantly influence DME formation rates at high methanol pressures (>10 kPa CH_3OH) [4]. These results suggest that methanol dehydration rates are not inhibited by intracrystalline transport of DME products and instead may reflect inhibition by absorption of excess methanol molecules as proposed previously [17], as would be expected from the decrease in methanol coverage with increasing temperature at fixed methanol pressure.

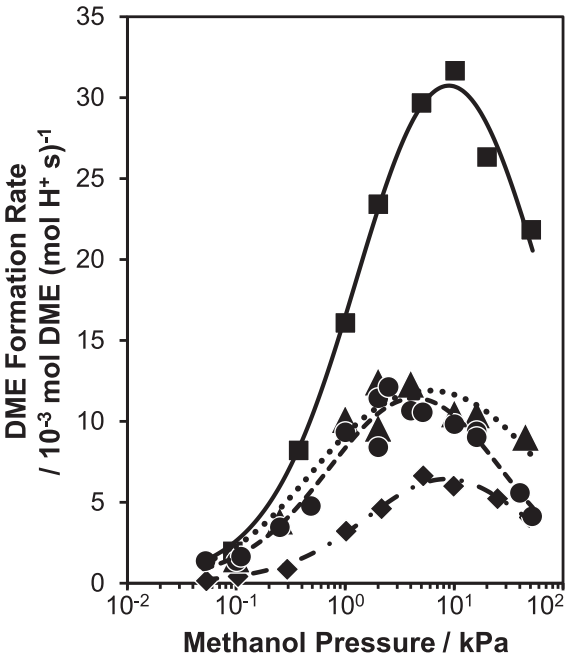

Fig. 6. Measured (data points) and regressed (lines; Eq. (3)) DME formation rates (415 K, per H^+) on representative AEI (squares; solid), CHA (circles; dashed), LEV (triangles; dotted), and LTA (diamonds; dash-dot) zeolites as a function of methanol pressure.

The adsorbed methanol structures on CHA zeolites containing isolated H^+ sites at varying temperatures (343–473 K) were assessed from *in situ* IR spectra measured at 10 kPa CH_3OH, which coincides with the onset of inhibition in CHA zeolites (Fig. 1). CH_3-OH cluster (~3370 cm^{-1}) [51] formation is a strong function of temperature (Fig. 8), evident by IR peaks that decrease in intensity at faster rates than those for protonated methanol dimers (2620 cm^{-1}; Fig. 8, inset) [13], suggesting that methanol adsorbs in clusters (e.g., trimers, tetramers) [51] more weakly than in protonated dimer structures. These findings are consistent with the adsorption of excess methanol at protonated methanol dimers, and with the attenuated inhibition of methanol dehydration rates at higher reaction temperatures (398–473 K; Fig. 7).

3.4. Adsorbed methanol structures as a function of coverage assessed from in situ IR spectra, equilibrium adsorption isotherms, and DFT-calculated free energies

Methanol adsorption isotherms (293 K; full isotherm shown in Fig. S.16 of Supp. Info.), normalized to the number of H^+ sites, were used to determine methanol coverage (θ_{CH3OH}, per H^+ site; Fig. 9a) on isolated H^+ sites in CHA zeolites as a function of methanol relative pressure (P P_{sat}^{-1}; P_{sat} is the saturated methanol vapor

Table 1
Measured and calculated first-order and zero-order free energy barriers (ΔG; kJ mol^{-1}) at 415 K for the associative and dissociative dehydration mechanisms at isolated H^+ sites in CHA zeolites.

	ΔG_{first} (kJ mol^{-1})	ΔG_{zero} (kJ mol^{-1})
Measured[a]	100	117
Associative[b]	123	137
Dissociative[b]	135	77

[a] Calculated from rate data measured between 383 and 415 K.
[b] Calculated from DFT (PBE-D3BJ, PAW).

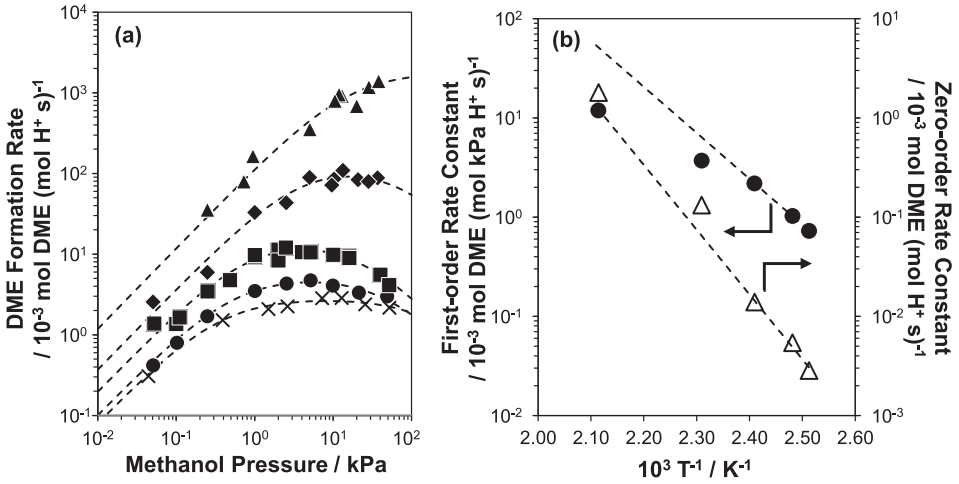

Fig. 7. (a) DME formation rates (per H^+) measured at 398 K (crosses), 403 K (circles), 415 K (squares), 433 K (diamonds), and 473 K (triangles) on CHA (Si/Al = 15) containing isolated H^+ sites. Dashed lines are linear regressions to Eq. (4). (b) First-order (closed circles) and zero-order (open triangles) rate constants (per H^+) measured as a function of temperature (398–473 K) on CHA (Si/Al = 15) containing isolated H^+ sites. Dashed line are exponential fits to the data between 398 and 415 K.

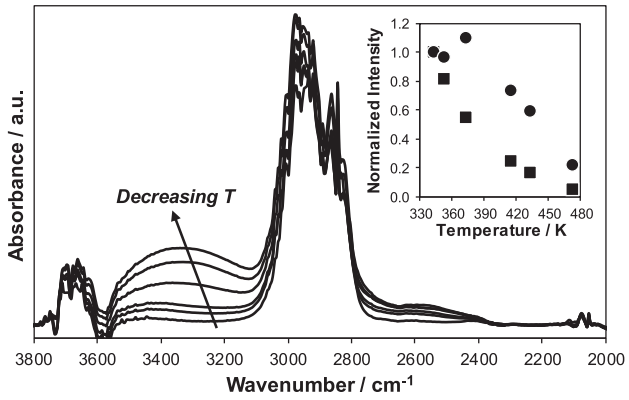

Fig. 8. IR spectra of H-CHA (Si/Al = 15, isolated Al) at 10 kPa CH_3OH measured at 343 K, 353 K, 373 K, 415 K), 433 K, and 473 K. Inset shows the intensity of the IR peaks for methanol clusters (~3370 cm^{-1}; squares) and protonated methanol dimers (~2620 cm^{-1}; circles) as a function of temperature, normalized to the peak intensity at 343 K.

pressure). Differential changes in methanol coverage (α) were calculated from the derivative of the methanol coverage isotherm (Fig. 9a) with respect to the logarithmic change in reduced pressure, according to the following equation:

$$\alpha = \frac{\partial \theta_{CH_3OH}}{\partial\left(\ln\left(\frac{P}{P_{sat}}\right)\right)} \tag{9}$$

Values of α are plotted as the secondary abscissa in Fig. 9a, and used to assess the rate of change of methanol coverage as a function of relative pressure in order to identify transitions in methanol chemisorption regimes, as typically done to identify transitions in physisorption regimes of non-interacting adsorbates (e.g., N_2, Ar) caused by the filling of pores of different characteristic size [55,56].

At low methanol coverages (<1 CH_3OH per H^+ site), adsorption is characterized by an initial maximum (~0.6 CH_3OH per H^+) in the differential methanol coverage isotherm, followed by a local minimum at ~1 CH_3OH (per H^+) (Fig. 9a). This adsorption behavior is characteristic of pore filling in the case of non-interacting adsorbates (e.g., Ar, N_2) within microporous voids [57], but in the case of

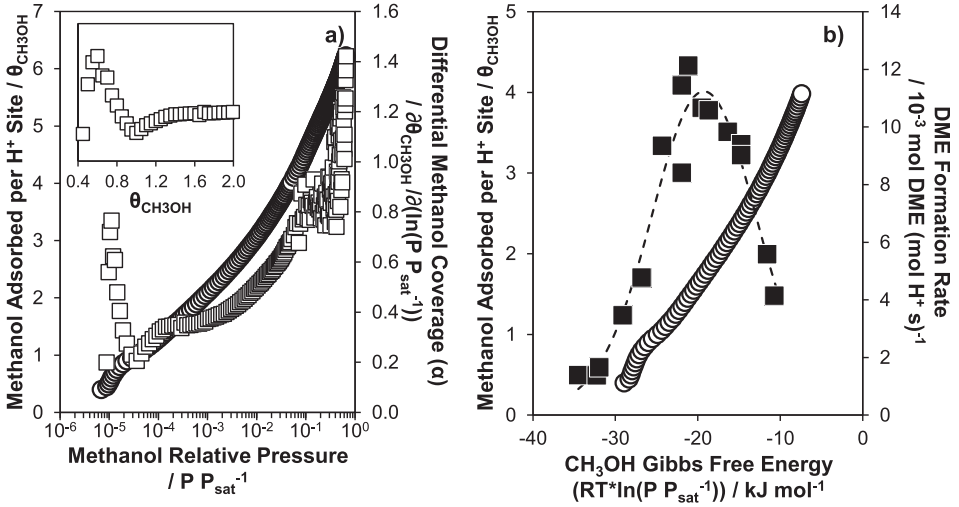

Fig. 9. (a) Methanol coverage (CH_3OH per H^+ site; circles) and the differential methanol coverage (Eq. (9); squares) as a function of methanol relative pressure on H-CHA containing only isolated H^+ sites at 293 K. The inset shows a magnified version of the differential methanol coverage versus methanol coverage at low methanol relative pressures ($P\,P_{sat}^{-1}$ <1 0 $^{-3}$). (b) DME formation rate (415 K, per H^+; squares) and methanol coverage (293 K, per H^+, circles) measured on H-CHA containing only isolated H^+ sites as a function of the gas-phase methanol Gibbs free energy (Eq. (10)). Dashed line is a fit of Eq. (4) to experimental DME formation rates (415 K, per H^+).

methanol reflects the selective adsorption at H^+ sites to form methanol monomers at coverages <1 CH_3OH (per H^+). Continued adsorption of methanol results in a second maximum and subsequent local minimum in the differential isotherm at ~1.7 CH_3OH (per H^+), which reflects the adsorption of a second methanol to form protonated dimers. This local minimum is then followed by the continuous adsorption of additional methanol with increasing methanol pressure until saturation of the CHA pore volume is achieved at a value corresponding to >6 CH_3OH (~0.20 cm^3 g^{-1} CH_3OH adsorbed at STP).

Methanol coverages (per H^+) at the temperatures of catalysis cannot be measured directly, and were instead estimated from equilibrium methanol adsorption data measured at 293 K by first transforming methanol relative pressure into an equivalent methanol Gibbs free energy (ΔG_{CH3OH}) according to the following equation (derivation in Section S.16 of the Supp. Info.):

$$\Delta G_{CH_3OH} = RTln\left(\frac{P}{P_{sat}}\right) \quad (10)$$

where R is the ideal gas constant (8.314 J mol^{-1} K^{-1}), T is the temperature (K), P is the absolute methanol pressure, and P_{sat} is the methanol vapor pressure (at T). The value of ΔG_{CH3OH} reflects equilibrium between gaseous and liquid-like intrazeolitic methanol species as a function of methanol pressure and temperature. Methanol coverages are plotted as a function of the ΔG_{CH3OH} (293 K, Fig. 9b), calculated from adsorption isotherm data (Fig. 9a) and Eq. (10). DME formation rates (415 K, per H^+) are also plotted as a function of ΔG_{CH3OH} (Fig. 9b), after normalizing the methanol partial pressures at which rates were measured (0.05–50 kPa) by the vapor pressure of methanol at 415 K according to Eq. (10). DME formation rates show a first-order dependence on ΔG_{CH3OH} values corresponding to methanol coverages of ~ 1 CH_3OH (per H^+), and begin to transition towards a zero-order kinetic regime for ΔG_{CH3OH} values corresponding to methanol coverages approaching 2 CH_3OH (per H^+). The onset of inhibition coincides with ΔG_{CH3OH} values of ~−19.4 kJ mol^{-1} (Fig. 9b) that correspond to methanol coverages exceeding ~2 CH_3OH (per H^+). These results further corroborate the interpretation that methanol dehydration rates (415 K) in CHA zeolites become inhibited upon adsorption of methanol beyond protonated dimer structures, and that such inhibition becomes more severe as additional methanol adsorbs within microporous voids at higher methanol partial pressures.

The structures of adsorbed methanol were also monitored by *in situ* IR spectra (293 K) collected upon dosing methanol in fractional quantities (~0.05 CH_3OH per H^+ per dose), as shown in Fig. 10. Only bare H^+ sites (~3605 cm^{-1}) and methanol monomers (~2380 cm^{-1}) are detected at low coverages of <0.3 CH_3OH (per H^+). Protonated methanol dimers (~2600 cm^{-1}) begin to appear beyond a coverage of ~0.3 CH_3OH (per H^+), and increase in intensity to saturation at ~2.3 CH_3OH (per H^+). At methanol coverages >0.7 CH_3OH (per H^+), peaks characteristic of methanol clusters (~3300 cm^{-1}) are observed and increase in intensity with methanol coverage up to 3 CH_3OH (per H^+), even after saturation of monomer and dimer features occurs. These data provide spectroscopic evidence for the formation of methanol clusters (>2 CH_3OH per H^+ site) at gas-phase methanol free energies that correspond to the onset of inhibition of methanol dehydration rates (415 K, per H^+) in CHA zeolites.

Adsorption free energy values are calculated using DFT to estimate equilibrium constants, and thus most stable methanol cluster size (per H^+) at an isolated H^+ site in CHA as a function of methanol partial pressure and temperature. Free energies of adsorption of methanol clusters ranging in size from 0 to 12 methanol molecules were computed to estimate the most stable species at an isolated H^+ site in CHA over a wide range of methanol pressures

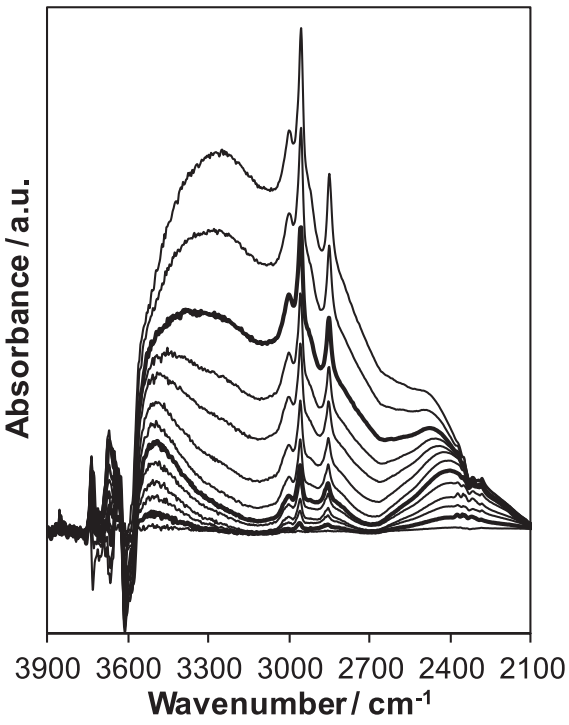

Fig. 10. IR spectra measured at 293 K on H-CHA (Si/Al = 15) with isolated H^+ sites as a function of methanol dosing (0.01–3 CH_3OH/H^+).

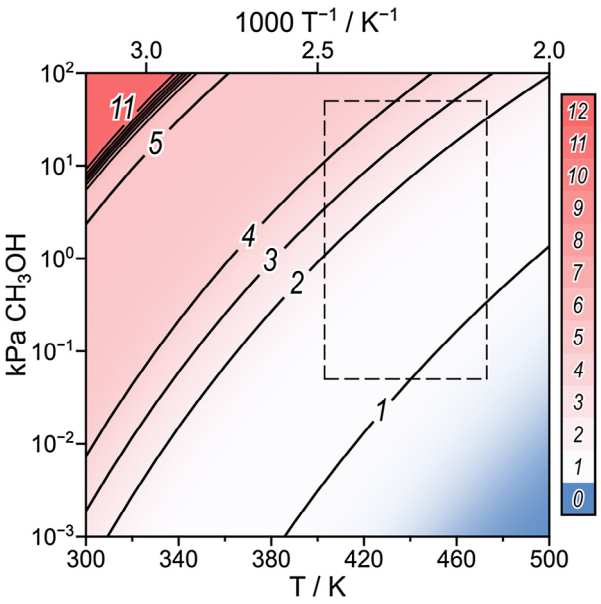

Fig. 11. Phase diagram predicting the average methanol cluster size at isolated H^+ sites in CHA, denoted by the phase boundary lines in the figure and the colored legend to the right of the figure. Equilibrium constants for adsorption were predicted by free energies from DFT at 415 K and 1 bar CH_3OH. The area enclosed by dashed lines correspond to the range of kinetic conditions studied for methanol dehydration in this work (403–473 K, 0.05–50 kPa CH_3OH).

(10^{-3}–10^2 kPa CH_3OH) and temperatures (300–500 K), as shown in Fig. 11. Methanol clusters deprotonate H^+ sites and form extended cationic networks with each other, in which methanol molecules link two O atoms of the AlO_4^- conjugate base through a series of H-bonds (additional details and data in Section S.15, Supp. Info.). At low temperatures and high methanol pressures (<350 K, >50 kPa CH_3OH), the most stable methanol cluster rapidly

shifts from a pentamer to a dodecamer (12 CH_3OH^*; Fig. 11). The predicted formation of these dodecamers is analogous to capillary condensation, when enthalpic stabilization conferred by adsorption of large quantities of methanol (or another adsorbate) leads to rapid filling of zeolite pores. Notably, these dodecamers have approximately the same density (12 CH_3OH^* per unit cell) as the methanol-saturated CHA samples measured experimentally (Fig. 9a). These CHA samples (Si/Al = 15) contain 2.25 H^+ per unit cell, while the DFT model (Si/Al = 35) contains 1 H^+ per unit cell; therefore, these DFT calculations reflect the pore-filling behavior observed experimentally.

The area enclosed by the dashed lines in Fig. 11 corresponds to the reaction conditions studied here, and methanol monomers and dimers dominate the surface of CHA at pressures below 3 kPa CH_3OH at 415 K. At high temperatures (>450 K) and low methanol pressures (<10^{-2} kPa CH_3OH), empty H^+ sites are predicted to be the most favorable conformation because entropic considerations favor desorption into the gas-phase, assuming adsorbed methanol molecules do not react (Fig. 11). Methanol trimers become the most prevalent cluster size at higher methanol pressures (3–13 kPa CH_3OH) at 415 K, which coincides with the onset of inhibition in experimentally measured DME formation rates (415 K, Fig. 1). DFT predicts that isolated H^+ sites in CHA are covered with a mixture of methanol tetramers and pentamers (~4.5 CH_3OH per H^+) at 50 kPa, the highest partial pressure where DME formation rates were measured. These results are consistent with experimentally measured methanol adsorption isotherms that indicate high-pressure kinetic inhibition occurs when coverages exceed two CH_3OH (per H^+) at 415 K (Fig. 9). The inhibition of methanol dehydration rates becomes attenuated at elevated temperatures in CHA zeolites (Fig. 7), consistent with DFT-predicted methanol coverages that decrease systematically with increasing temperature (>433 K). From examining the DFT-predicted coverages at the 50 kPa isobar, methanol coverages change from a mixture of tetramers and pentamers at 415 K to a mixture of dimers and trimers at 473 K (Fig. 11). These observations are consistent with the disappearance of methanol clusters at elevated temperatures (>433 K, Fig. 8) and with attenuated high-pressure inhibition of methanol dehydration rates at elevated temperatures (>433 K, Fig. 7).

Methanol clusters around Brønsted acid sites form extended networks with each other, in which methanol molecules link two O atoms of the acid site through a series of H-bonds (Fig. 12). The methanol monomer prefers to adsorb to O4 in CHA and interact with another O atom in the associated 8-MR (Fig. 12a). Monomers interact with only a proton bound to one O atom of the Brønsted acid site; however, as more methanol adsorbs, the site deprotonates to form protonated clusters that interact with multiple O atoms of the conjugate base. This multisite interaction has been shown in previous theoretical studies of methanol dehydration on MFI and on POM clusters [10,53,54,58]. Complexes comprised of 2–5 CH_3OH prefer to interact with O3 and O4 of CHA concurrently (Fig. 12b–e). As clusters expand, the distance over which they can interact increases, allowing for clusters of >5 CH_3OH to interact with O4 and O1 through both 8-MR adjacent to the Al T-site (Fig. S.18, Supp. Info).

This set of kinetic, spectroscopic, and theoretical data indicates that the low-temperature (415 K) dehydration of methanol to DME proceeds via the associative dehydration mechanism in CHA zeolites containing predominantly isolated H^+ sites and is inhibited by the formation of methanol clusters at high methanol partial pressures (>10 kPa). Although formation of these higher-order clusters can be included as separate elementary steps in a more comprehensive reaction mechanism, deriving a rate law to describe high-pressure inhibition becomes convoluted by the inability to distinguish whether a specific methanol cluster is solely responsible for inhibition, or whether parallel DME formation routes from higher-order clusters proceed at different rates via interactions of additional methanol with the relevant precursor and transition states. Perturbation of methanol dehydration turnover rates (per H^+, 473 K) by the presence of neighboring Na^+ atoms on partially-exchanged POM clusters [59] further suggests that the presence of excess methanol may alter the free energy landscape for DME formation in CHA zeolites. These different possibilities can be described by a generalized rate law accounting for the superposition of parallel DME formation routes at H^+ sites covered with different methanol cluster sizes:

$$r_A = \frac{\sum_{j=2}^{k} \alpha_j P_{CH_3OH}^{j}}{\sum_{m=1}^{n} \beta_m P_{CH_3OH}^{m}} \quad (11)$$

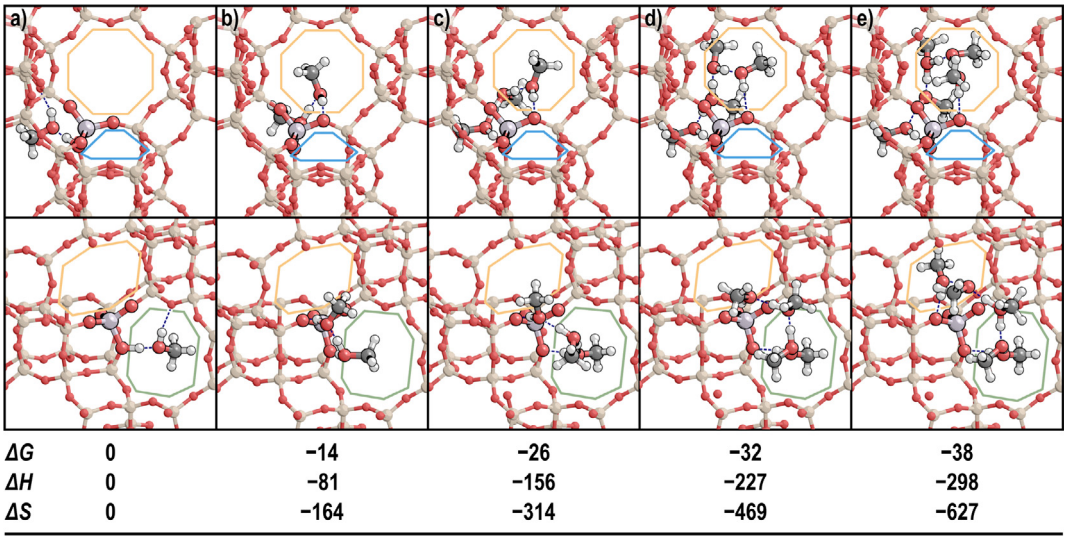

Fig. 12. The most stable methanol clusters comprised of (a) a methanol monomer (CH_3OH^*), (b) a methanol dimer (2 CH_3OH^*), (c) a methanol trimer (3 CH_3OH^*), (d) a methanol tetramer (4 CH_3OH^*), and (e) a methanol pentamer (5 CH_3OH^*). Free energies (ΔG) and enthalpies (ΔH) in kJ mol^{-1}, and entropies (ΔS) in J mol^{-1} K^{-1}, are shown relative to the methanol monomer at 415 K and 1 bar CH_3OH. The 8-MR (orange, green) and 6-MR (blue) adjacent to each structure are highlighted. H-bonds are indicated with dashed lines (navy) and are all 170–250 pm.

where, j represents the number of methanol (i.e., 2 through k molecules) involved in the transition state, α_j represents the apparent rate constants for DME formation when j methanol are involved in the transition state, m represents the number of methanol (i.e., 1 through n molecules) in the various MASI species (e.g., monomers, dimers, higher-order clusters), and β_m represents the apparent equilibrium constants to form a methanol cluster containing m molecules from a gaseous methanol and an adsorbed cluster containing m-1 methanol molecules. While this rate law (Eq. (11)) describes all possible DME formation routes and surface coverages, it does not provide additional mechanistic insight into the nature of high-pressure inhibition in small-pore zeolites. In the following section, we thus use DFT to investigate various DME formation routes via intermediates and transition states at different coverage, pressures, and temperatures in at isolated H^+ sites in CHA zeolites.

3.5. DFT-predicted DME formation rates at different methanol coverages

DME formation can occur after desorption of excess methanol to form the kinetically relevant transition state, or in the presence of adsorbed spectating methanol molecules, which can influence the stabilities of the dehydration transition state and its relevant precursor state. Here, we calculate the Gibbs free energy barrier of each methanol dehydration transition state with up to four CH_3-OH co-adsorbed at an isolated H^+ site in CHA. This approach accounts for the potential contributions from parallel DME formation pathways that occur with additional spectating methanol and gives mechanistic insight into the interactions during catalysis from larger clusters of oxygenates in zeolites.

Surface methylation transition states prefer to form H-bonds with spectating CH_3OH species rather than with framework O atoms (Fig. 13), because the methanol O—H bond is more polar than framework Si—O bonds, enhancing H-bonding between these hydroxyl moieties. Therefore, spectating methanol species prefer to insert themselves where H-bonds between transition states and framework O atoms are otherwise located in the absence of spectating adsorbates (Fig. 4a). Intrinsic reaction free energy barriers (ΔG_{int}) are essentially unaffected by the insertion of one spectating species into transition states (135 kJ mol^{-1} without spectator to 134 kJ mol^{-1} with one spectator), but increase upon insertion of multiple spectating species (155 and 143 kJ mol^{-1} for two and three spectating methanol molecules, respectively) as they crowd the transition state and inhibit its formation (Fig. 13). In contrast, apparent barriers (ΔG_{app}) for surface methylation transition states remain similar (130–135 kJ mol^{-1}), except for that with one spectating methanol (121 kJ mol^{-1}), as larger methanol clusters become favored at the conditions at which free energies are approximated (415 K, 1 bar). Despite higher ΔG_{int} values with additional spectating molecules, ΔG_{app} values remain essentially unchanged because enthalpic stabilization conferred by H-bonding with additional methanol compensates for the entropic losses to form larger clusters. These data indicate that the first step of the dissociative dehydration mechanism occurs with lower standard state (1 bar) free energy barriers in the presence of a spectating methanol at isolated H^+ sites in CHA (415 K).

Similarly, the second step of the dissociative route can occur in the presence of spectating methanol (Fig. 14). The intrinsic barriers for this second step decrease in the presence of additional spectating methanol molecules from 78 to 35–36 kJ mol^{-1} (Fig. 14). The methanol accepting the surface methoxy group forms additional H-bonds to spectating methanol in the most stable transition states identified, because framework Si—O bonds are less polar than hydroxyl O—H bonds of spectating methanol, which favors H-bonding between methanol species during reaction as in the case of surface methylation reactions. The insertion of these co-adsorbed methanol molecules into the transition states also overcomes strain in forming H-bonding networks between the cationic transition state and the zeolite framework. The stronger H-bonds provided by co-adsorbed methanol molecules stabilize dissociative DME formation transition states more than the precursor state, CH_3–Z, leading to decreases in intrinsic barriers with spectating

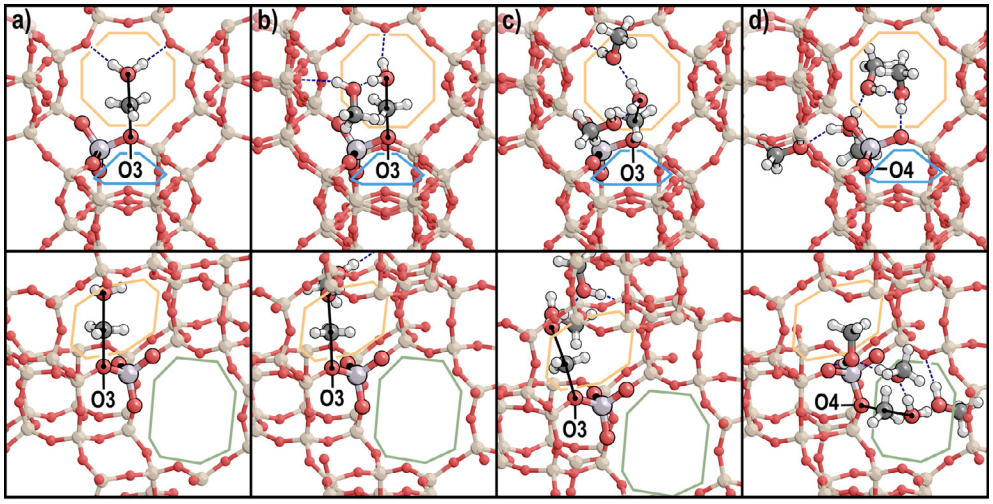

	a)	b)	c)	d)
ΔG_{app}	135	121	130	133
ΔH_{app}	129	62	6	−56
ΔS_{app}	−14	−142	−297	−456
ΔG_{int}	135	134	155	143

Fig. 13. The most favorable surface methylation transition state with (a) zero, (b) one, (c) two, and (d) three spectating CH_3OH molecules. Incipient and breaking bonds of the transition state are shown with black lines and H-bonds in navy. The O atom with which the methyl group is interacting is labeled. Apparent free energies (ΔG_{app}) and enthalpies (ΔH_{app}) in kJ mol^{-1}, and entropies (ΔS_{app}) in J mol^{-1} K^{-1}, are shown relative to an adsorbed methanol. Intrinsic free energy barriers (ΔG_{int}) are shown in kJ mol^{-1}. The 8-MR (orange, green) and 6-MR (blue) adjacent to each transition state are highlighted.

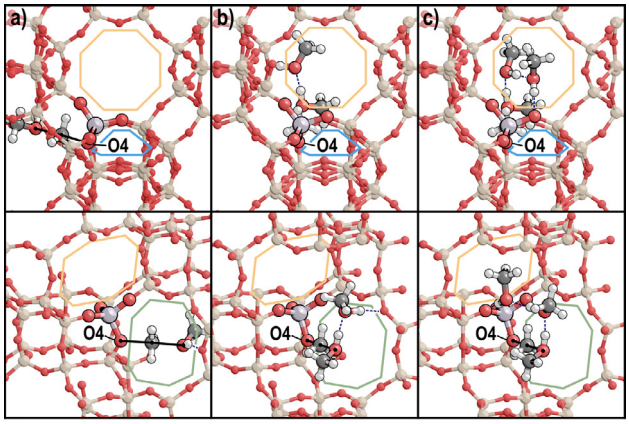

ΔG_{app}	130	112	106
ΔH_{app}	121	44	−28
ΔS_{app}	−22	−163	−323
ΔG_{int}	78	36	35

Fig. 14. The most favorable transition states for the second step of the dissociative route with (a) zero, (b) one and (c) two spectating CH_3OH molecules. Incipient and breaking bonds of the transition state are shown with black lines and H-bonds in navy. The O atom with which the methyl group is interacting is labeled. Apparent free energies (ΔG_{app}) and enthalpies (ΔH_{app}) in kJ mol^{-1}, and entropies (ΔS_{app}) in J mol^{-1} K^{-1}, are shown relative to an adsorbed methanol. Intrinsic free energy barriers (ΔG_{int}) are shown in kJ mol^{-1}. The 8-MR (orange, green) and 6-MR (blue) adjacent to each transition state are highlighted.

methanol present. These decreases in the intrinsic barriers propagate to apparent free energy barriers (1 bar, 415 K) for this reaction, indicating that this reaction is more facile at high methanol coverages.

The associative route can also occur in the presence of spectating methanol molecules (Fig. 15). One spectating methanol molecule at these conditions reduces both the overall (95 kJ mol^{-1}) and intrinsic (121 kJ mol^{-1}) DME formation barriers by 18 and 16 kJ mol^{-1}, respectively. The first spectating methanol prefers to insert between the methanol accepting the methyl group and the

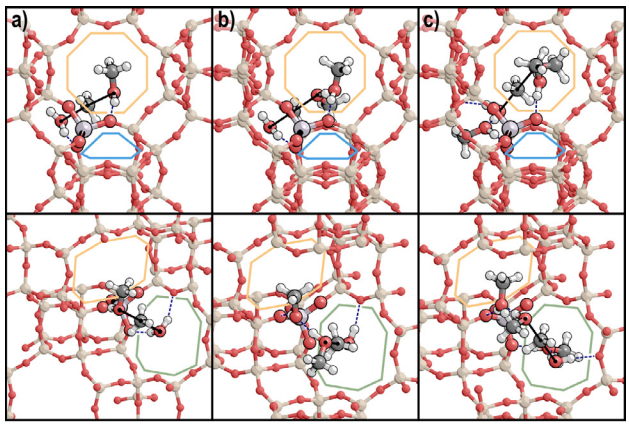

ΔG_{app}	123	95	114
ΔH_{app}	51	−38	−86
ΔS_{app}	−174	−321	−482
ΔG_{int}	137	121	146

Fig. 15. The most favorable transition states for the associative route with (a) zero, (b) one and (c) two spectating CH_3OH molecules. Incipient and breaking bonds of the transition state are shown with black lines and H-bonds in navy. Overall free energies (ΔG_{app}) and enthalpies (ΔH_{app}) in kJ mol^{-1}, and entropies (ΔS_{app}) in J mol^{-1} K^{-1}, are shown relative to an adsorbed methanol. Intrinsic free energy barriers (ΔG_{int}) are shown in kJ mol^{-1}. The 8-MR (orange, green) and 6-MR (blue) adjacent to each transition state are highlighted.

conjugate base (Fig. 15b). An additional spectating methanol then interacts with the conjugate base between the H_2O leaving group and the conjugate base, such that the transition state only interacts with the framework through spectating methanol molecules (Fig. 15c). This implies that the surface Brønsted acid site is no longer directly involved in the reaction, but instead allows for the formation of protonated clusters within which reactions proceed. These associative transition states occur with lower apparent free energy barriers (1 bar, 415 K) than dissociative transition states at corresponding methanol coverages. Specifically, the associative route with one spectating methanol has the lowest apparent free energy barrier for DME formation (95 kJ mol^{-1}) of all the transition states tested in this work (Fig. 15b). This indicates that methanol dehydration at sufficiently high pressures and low temperatures will prefer to occur in the presence of spectating methanol molecules and from larger clusters of methanol.

Spectating methanol molecules introduce additional possible pathways that may occur in parallel to form DME (Scheme S.4 in Supp. Info.) and maximum rate analysis can be used to identify quasi-equilibrated and kinetically relevant elementary steps and compare predicted rates of these competing pathways by calculating relevant standard-state rate and equilibrium constants from predicted reaction and activation free energies. This analysis allows for estimation of the contribution of each mechanism tested here (dissociative and associative with 0–3 spectating CH_3OH) to the overall rates of methanol dehydration measured at different conditions. The associative mechanism with no spectating methanol molecules occurs faster than the same mechanism with one or two spectators at <0.02 kPa CH_3OH (Fig. 16a); at higher pressures, the rate with one spectating methanol is higher than with zero or two spectators. Fig. 16c shows the best associative pathways (0 spectators <0.02 kPa and 1 spectator at higher pressures) and the best rates of the second step of the dissociative pathway, as well as the rates of the first step of the dissociative pathway with 0–3 spectators. The second step of the dissociative mechanism is rapid at all conditions, and always more so than the first step, regardless of the number of spectating methanol species (Fig. 16c), which indicates that the first step of the dissociative mechanism is the kinetically relevant step for dissociative DME formation at all relevant pressures at 415 K. Overall, the dissociative mechanism without spectators prevails at methanol pressures <0.3 kPa, because rates of associative DME formation are suppressed at such low coverages of methanol dimer and trimer complexes, yet the associative mechanism with one spectating methanol prevails at all methanol partial pressures above 0.3 kPa shown here (up to 100 kPa) (Fig. 16c). The high-pressure mechanism implied by studies on heteropolyacids and other zeolite frameworks is that DME is made from the rearrangement of a protonated methanol dimer [10,13,15]; in CHA, this route (absent spectators) does not prevail at any condition. Despite the preferable formation of tetramers and pentamers at higher methanol pressures at 415 K, routes with 2–3 spectators (up to four methanol molecules total) occur at rates slower than the associative route with one spectating methanol. This preference for the associative DME formation route with one spectating methanol, at conditions where tetramers and pentamers begin to increase in coverage, results in apparent kinetic inhibition as methanol molecules must desorb first for the preferred route to occur.

The sum of estimated rates of all parallel pathways (Eq. S.47) that form DME is compared to experimentally measured rates of methanol dehydration at 415 K from 0.01 to 100 kPa CH_3OH in Fig. 17. To exemplify qualitative trends, DFT-predicted rates are multiplied by a factor of 5.1 such that their relative scales are similar. The predicted rate behavior agrees qualitatively with that measured in kinetic experiments. Theoretically predicted and experimentally measured rates increase in a first-order regime at

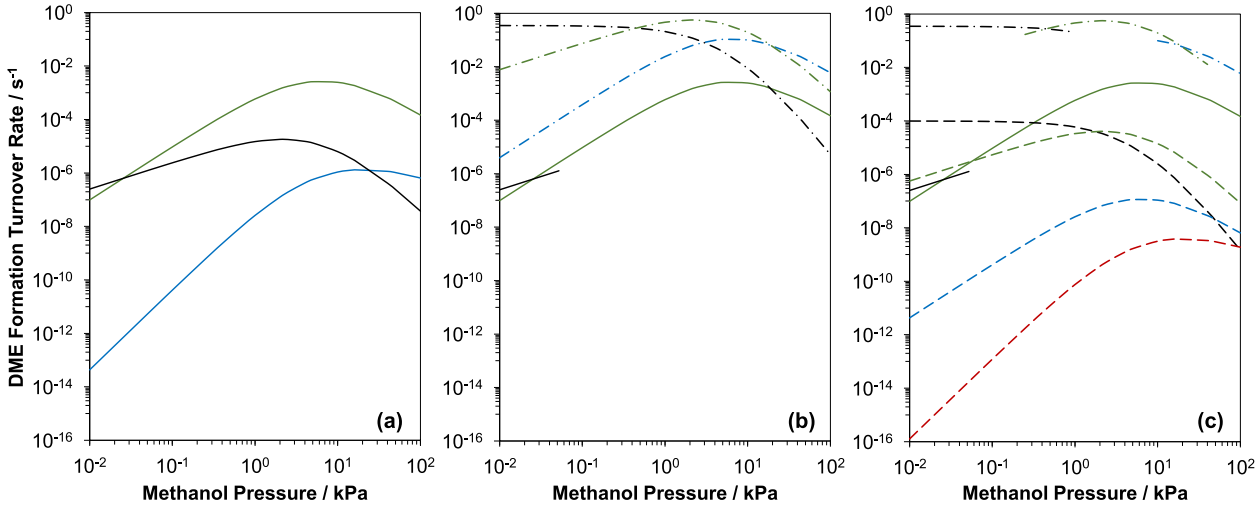

Fig. 16. DFT-predicted rates (415 K) with zero (black), one (green), two (blue), or three (red) spectating methanol molecules for (a) the associative mechanism (solid lines), (b) kinetically-relevant DME formation of the dissociative mechanism (dashed-dotted lines), and (c) kinetically-relevant methoxy formation of the dissociative mechanism (dashed lines) at 0.1% CH_3OH conversion. The maximum predicted rates of the associative mechanism (solid lines) are shown in (b) and (c) and of kinetically-relevant DME formation of the dissociative mechanism (dashed-dotted lines) are shown in (c) for comparison.

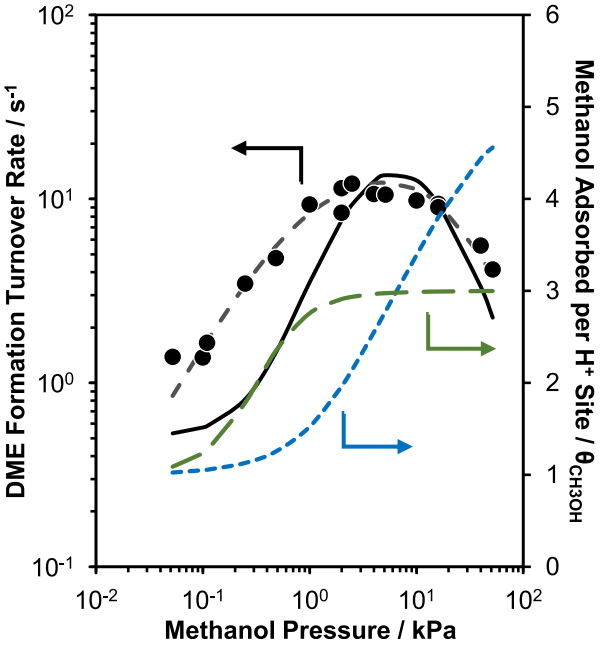

Fig. 17. Measured DME formation rates (415 K, per H^+; circles), regression of measured rates to Eq. (12) (grey dashed line), and DFT-predicted rates (415 K) scaled by 5.1x (solid black line, Eq. S.47) at 0.1% conversion. Average methanol cluster size (blue dashed line) and average number of methanol molecules in dehydration transition states (green dashed line) are shown for comparison.

low pressures, reach a maximum corresponding to the zero-order regime, and then become inhibited at higher pressures.

This theoretical evidence in conjunction with spectroscopic and adsorption data (Sections 3.3 and 3.4) indicates that associative methanol dehydration is inhibited at high pressures when trimers, tetramers, and pentamers form in small-pore zeolites. Methanol dehydration preferentially occurs from a trimer containing one spectating methanol at intermediate pressures. Tetramers and pentamers form at higher methanol pressures, but their dehydration transition states are crowded by spectating species and associative routes with only one spectator continue to prevail. Thus, desorption precedes DME formation to yield more favorable transition states and rates are inhibited at high methanol partial pressures. Given that DME formation proceeds predominantly via the associative route with one spectating methanol at relevant pressures (>0.3 kPa CH_3OH) and larger clusters can form within the CHA pores, DME formation rates can be described as

$$r_{DME} = \frac{k_{DME,A3} K_D K_{Tr} P^2_{CH_3OH}}{1 + K_D P_{CH_3OH} + K_D K_{Tr} P^2_{CH_3OH} + K_D K_{Tr} K_{Te} P^3_{CH_3OH} + K_D K_{Tr} K_{Te} K_P P^4_{CH_3OH}} \quad (12)$$

This rate law reflects the dominance of the associative route with one spectating methanol, and up to a methanol pentamer as potential MASI, and accurately predicts the kinetic behavior measured experimentally (dashed line in Fig. 17).

4. Conclusions

A combined experimental and computational approach was used to investigate the mechanistic origin of the high-pressure inhibition of rates of methanol dehydration to dimethyl ether (DME) in small-pore zeolites (CHA, AEI, LEV, LTA), which occurs irrespective of the framework Al or extraframework H^+ site distribution. CHA zeolites containing isolated H^+ sites were chosen as the exemplar case in order to simplify mechanistic interpretation of experimentally measured data and to connect experimental data more faithfully to the low Al-content structures modeled by theory (Si/Al = 35). Identifying the mechanistic origins of high-pressure inhibition first required knowledge of the prevalent reaction mechanisms and kinetically relevant steps for methanol conversion to DME. Experimental measurements of methanol dehydration turnover rate dependences on pressure (0.05–50 kPa) and temperature (403–473 K), and *in situ* IR spectra that monitor prevalent surface intermediates as a function of reaction conditions, provide evidence that methanol dehydration proceeds via the associative mechanism on isolated H^+ sites in CHA zeolites. These observations were corroborated by DFT calculations that enabled discriminating candidate parallel dehydration pathways from different surface intermediates. Reaction and activation free energies were calculated for the associative and dissociative dehydration mechanisms after systematically identifying the most energetically favorable adsorbate and transition state configurations by reorienting transition states and intermediates around framework binding sites and

within adjacent voids. The most stable transition state structures were those that maximized the number of hydrogen bonds made with framework O atoms, leading to more effective charge distribution and stronger stabilizing interactions between reacting species and the zeolite framework. A maximum rate analysis of the most favorable routes for the associative and dissociative pathways showed that the dissociative mechanism prevails at isolated H^+ sites in CHA at sufficiently low methanol pressures (e.g., <4 kPa at 415 K), but that the associative mechanism dominates at higher pressures, especially those corresponding to the onset of experimentally observed high-pressure inhibition (>10 kPa CH_3OH, 415 K).

Methanol adsorption equilibrium isotherms (10^{-4}–10 kPa, 293 K) were used to estimate the methanol coverages (per H^+ site) present during catalysis (0.05–50 kPa, 415 K), by comparing data at equivalent gaseous methanol free energy. This analysis suggests that inhibition of methanol dehydration rates (415 K) occurs at coverages exceeding 2 CH_3OH per H^+ site. Methanol dehydration rates measured as a function of temperature (403–473 K) reveal that high-pressure inhibition disappears at elevated temperatures (>450 K), concomitant with the disappearance of methanol clusters in IR spectra measured under equivalent conditions. These experimental data indicate that the associative dehydration mechanism becomes inhibited by the adsorption of excess methanol, but these data alone are unable to distinguish between parallel dehydration pathways that may proceed through different methanol intermediates at different rates.

DFT-predicted methanol coverages agree with those estimated experimentally and indicate that inhibition of methanol dehydration occurs in the presence of methanol trimers and tetramers, with pentamers ultimately forming at the highest of experimental pressures studied (>40 kPa, 415 K). Methanol coverages calculated at high pressures and elevated temperatures (up to 473 K) show that the surface shifts to being covered primarily by methanol dimers, consistent with the disappearance of high-pressure inhibition at temperatures >450 K. Free energies for DME formation transition states were calculated for the associative and dissociative pathways, and a maximum rate analysis was used to predict DME formation rates as a function of methanol pressure and coverage. This analysis indicates that the associative dehydration pathway prevails under the experimental conditions tested here (0.1–50 kPa CH_3OH, 415 K), but that the most favorable dehydration route occurs via a methanol trimer and that inhibition reflects the formation of methanol tetramers, from which methanol must first desorb to form transition states of sufficient stability. Applying observations from both experiment and theory, a rate expression was derived for the associative dehydration mechanism wherein DME is formed via methanol trimers and becomes inhibited by methanol tetramers, which describes DME formation rates measured experimentally on isolated H^+ sites in CHA. This kinetic model allows for the quantitative description of methanol inhibition in CHA zeolites, and extension of this analysis to better understand the mechanistic differences between isolated and paired H^+ sites in small-pore zeolites. These findings highlight how modeling interactions between transition states and the zeolite framework with different reactant coverages can be used to clarify and extend insights gained from measurements of kinetic inhibition. This work highlights methods for handling the complexity that arises when zeolites turn over catalytic cycles under conditions wherein molecules are present in extended complexes and approach condensation regimes.

Acknowledgements

We acknowledge financial support provided by the National Science Foundation CAREER program under award number 1552517-CBET for the experimental work at Purdue. We also thank Sachem, Inc. for providing the organic structure-directing agent used to synthesize SSZ-13. A.H. and D.H. also acknowledge funding from the ACS Petroleum Research Fund New Doctoral Investigation Award (57079DNI5). This work used the Extreme Science and Engineering Discovery Environment (XSEDE) [60], which is supported by the National Science Foundation grant number ACI-1548562 through allocation CTS160041. Additional computational resources were provided by the University of Florida Research Computing.

Appendix A. Supplementary material

Supplementary data to this article can be found online at https://doi.org/10.1016/j.jcat.2019.10.012.

References

[1] C. Chang, A. Silvestri, The conversion of methanol and other O-compounds to hydrocarbons over zeolite catalysts, J. Catal. 47 (1977) 249–259, https://doi.org/10.1016/0021-9517(77)90172-5.
[2] R. Dessau, On the H-ZSM-5 catalyzed formation of ethylene from methanol or higher olefins, J. Catal. 99 (1986) 111–116, https://doi.org/10.1016/0021-9517(86)90204-6.
[3] S. Ilias, A. Bhan, Mechanism of the catalytic conversion of methanol to hydrocarbons, ACS Catal. 3 (2013) 18–31, https://doi.org/10.1021/cs3006583.
[4] U. Olsbye, S. Svelle, M. Bjørgen, P. Beato, T.V.W. Janssens, F. Joensen, et al., Conversion of methanol to hydrocarbons: how zeolite cavity and pore size controls product selectivity, Angew. Chem. Int. Ed. Engl. 51 (2012) 5810–5831, https://doi.org/10.1002/anie.201103657.
[5] J.H. Kang, F.H. Alshafei, S.I. Zones, M.E. Davis, Cage-defining ring: a molecular sieve structural indicator for light olefin product distribution from the methanol-to-olefins reaction, ACS Catal. 9 (2019) 6012–6019, https://doi.org/10.1021/acscatal.9b00746.
[6] P. Bollini, A. Bhan, Improving HSAPO-34 methanol-to-olefin turnover capacity by seeding the hydrocarbon pool, ChemPhysChem. 19 (2018) 479–483, https://doi.org/10.1002/cphc.201701027.
[7] Y. Liu, F.M. Kirchberger, S. Müller, M. Eder, M. Tonigold, M. Sanchez-Sanchez, et al., Critical role of formaldehyde during methanol conversion to hydrocarbons, Nat. Commun. 10 (2019) 1462, https://doi.org/10.1038/s41467-019-09449-7.
[8] Y. Liu, S. Müller, D. Berger, J. Jelic, K. Reuter, M. Tonigold, et al., Formation mechanism of the first carbon-carbon bond and the first olefin in the methanol conversion into hydrocarbons, Angew. Chem. Int. Ed. Engl. 55 (2016) 5723–5726, https://doi.org/10.1002/anie.201511678.
[9] E. Derouane, J. Nagy, P. Dejaifve, J.H.C. van Hooff, B.P. Spekman, J.C. Védrine, et al., Elucidation of the mechanism of conversion of methanol and ethanol to hydrocarbons on a new type of synthetic zeolite, J. Catal. 53 (1978) 40–55, https://doi.org/10.1016/0021-9517(78)90006-4.
[10] R.T. Carr, M. Neurock, E. Iglesia, Catalytic consequences of acid strength in the conversion of methanol to dimethyl ether, J. Catal. 278 (2011) 78–93, https://doi.org/10.1016/j.jcat.2010.11.017.
[11] A.J. Jones, S.I. Zones, E. Iglesia, Implications of transition state confinement within small voids for acid catalysis, J. Phys. Chem. C. 118 (2014) 17787–17800, https://doi.org/10.1021/jp5050095.
[12] A.J. Jones, R.T. Carr, S.I. Zones, E. Iglesia, Acid strength and solvation in catalysis by MFI zeolites and effects of the identity, concentration and location of framework heteroatoms, J. Catal. 312 (2014) 58–68, https://doi.org/10.1016/j.jcat.2014.01.007.
[13] A.J. Jones, E. Iglesia, Kinetic, spectroscopic, and theoretical assessment of associative and dissociative methanol dehydration routes in zeolites, Angew. Chem. Int. Ed. Engl. 53 (2014) 12177–12181, https://doi.org/10.1002/anie.201406823.
[14] R. Gounder, A.J. Jones, R.T. Carr, E. Iglesia, Solvation and acid strength effects on catalysis by faujasite zeolites, J. Catal. 286 (2012) 214–223, https://doi.org/10.1016/j.jcat.2011.11.002.
[15] A. Ghorbanpour, J.D. Rimer, L.C. Grabow, Computational assessment of the dominant factors governing the mechanism of methanol dehydration over H-ZSM-5 with heterogeneous aluminum distribution, ACS Catal. 6 (2016) 2287–2298, https://doi.org/10.1021/acscatal.5b02367.
[16] J.R. Di Iorio, C.T. Nimlos, R. Gounder, Introducing catalytic diversity into single-site chabazite zeolites of fixed composition via synthetic control of active site proximity, ACS Catal. 7 (2017) 6663–6674, https://doi.org/10.1021/acscatal.7b01273.
[17] J.R. Di Iorio, R. Gounder, Controlling the isolation and pairing of aluminum in chabazite zeolites using mixtures of organic and inorganic structure-directing agents, Chem. Mater. 28 (2016) 2236–2247, https://doi.org/10.1021/acs.chemmater.6b00181.
[18] S. Nystrom, A. Hoffman, D. Hibbitts, Tuning Brønsted acid strength by altering site proximity in CHA framework zeolites, ACS Catal. 8 (2018) 7842–7860, https://doi.org/10.1021/acscatal.8b02049.

[19] H. Chiang, A. Bhan, Catalytic consequences of hydroxyl group location on the rate and mechanism of parallel dehydration reactions of ethanol over acidic zeolites, J. Catal. 271 (2010) 251–261, https://doi.org/10.1016/j.jcat.2010.01.021.
[20] Y. Zhi, H. Shi, L. Mu, Y. Liu, D. Mei, D.M. Camaioni, et al., Dehydration pathways of 1-Propanol on HZSM-5 in the presence and absence of water, J. Am. Chem. Soc. 137 (2015) 15781–15794, https://doi.org/10.1021/jacs.5b09107.
[21] J. Macht, M.J. Janik, M. Neurock, E. Iglesia, Mechanistic consequences of composition in acid catalysis by polyoxometalate Keggin clusters, J. Am. Chem. Soc. 130 (2008) 10369–10379, https://doi.org/10.1021/ja803114r.
[22] M. Dusselier, J.E. Schmidt, R. Moulton, B. Haymore, M. Hellums, M.E. Davis, Influence of organic structure directing agent isomer distribution on the synthesis of SSZ-39, Chem. Mater. 27 (2015) 2695–2702, https://doi.org/10.1021/acs.chemmater.5b00651.
[23] J.D. Albarracin-Caballero, I. Khurana, J.R. Di Iorio, A.J. Shih, J.E. Schmidt, M. Dusselier, et al., Structural and kinetic changes to small-pore Cu-zeolites after hydrothermal aging treatments and selective catalytic reduction of NO_x with ammonia, React. Chem. Eng. 2 (2017) 168–179, https://doi.org/10.1039/C6RE00198J.
[24] S. Shibata, M. Itakura, Y. Ide, M. Sadakane, T. Sano, FAU–LEV interzeolite conversion in fluoride media, Micropor. Mesopor. Mat. 138 (2011) 32–39, https://doi.org/10.1016/j.micromeso.2010.09.034.
[25] D. Jo, T. Ryu, G.T. Park, P.S. Kim, C.H. Kim, I.-S. Nam, et al., Synthesis of high-silica LTA and UFI zeolites and NH_3 –SCR performance of their copper-exchanged form, ACS Catal. 6 (2016) 2443–2447, https://doi.org/10.1021/acscatal.6b00489.
[26] C. Baerlocher, L.B. McCusker, Database of Zeolite Structures: http://www.iza-structure.org/databases., (2013). http://www.iza-structure.org/databases.
[27] J.R. Di Iorio, S.A. Bates, A.A. Verma, W.N. Delgass, F.H. Ribeiro, J.T. Miller, et al., The dynamic nature of brønsted acid sites in Cu–Zeolites during NOx selective catalytic reduction: quantification by gas-phase ammonia titration, Top. Catal. 58 (2015) 424–434, https://doi.org/10.1007/s11244-015-0387-8.
[28] V.J. Cybulskis, J.W. Harris, Y. Zvinevich, F.H. Ribeiro, R. Gounder, A transmission infrared cell design for temperature-controlled adsorption and reactivity studies on heterogeneous catalysts, Rev. Sci. Instrum. 87 103101 (2016), https://doi.org/10.1063/1.4963665.
[29] J.W. Harris, M.J. Cordon, J.R. Di Iorio, J.C. Vega-Vila, F.H. Ribeiro, R. Gounder, Titration and quantification of open and closed Lewis acid sites in Sn-Beta zeolites that catalyze glucose isomerization, J. Catal. 335 (2016) 141–154, https://doi.org/10.1016/j.jcat.2015.12.024.
[30] J.S. Bates, R. Gounder, Influence of confining environment polarity on ethanol dehydration catalysis by Lewis acid zeolites, J. Catal. 365 (2018) 213–226, https://doi.org/10.1016/j.jcat.2018.05.009.
[31] G. Kresse, J. Hafner, Ab initio molecular-dynamics simulation of the liquid-metal-amorphous-semiconductor transition in germanium, Phys. Rev. B, Condens. Matter. 49 (1994) 14251–14269, https://doi.org/10.1103/PhysRevB.49.14251.
[32] G. Kresse, J. Hafner, *Ab initio* molecular dynamics for liquid metals, Phys. Rev. B. 47 (1993) 558–561, https://doi.org/10.1103/PhysRevB.47.558.
[33] G. Kresse, J. Furthmüller, Efficient iterative schemes for *ab initio* total-energy calculations using a plane-wave basis set, Phys. Rev. B. 54 (1996) 11169–11186, https://doi.org/10.1103/PhysRevB.54.11169.
[34] G. Kresse, J. Furthmüller, Efficiency of ab-initio total energy calculations for metals and semiconductors using a plane-wave basis set, Comp. Mater. Sci. 6 (1996) 15–50, https://doi.org/10.1016/0927-0256(96)00008-0.
[35] P. Kravchenko, C. Plaisance, D. Hibbitts, A new computational interface for catalysis, Pre-Print Available rxiv.link/8040737 (n.d.). http://doi.org/10.26434/chemrxiv.8040737.v3.
[36] G. Kresse, D. Joubert, From ultrasoft pseudopotentials to the projector augmented-wave method, Phys. Rev. B. 59 (1999) 1758–1775, https://doi.org/10.1103/PhysRevB.59.1758.
[37] P.E. Blöchl, Projector augmented-wave method, Phys. Rev. B. 50 (1994) 17953–17979, https://doi.org/10.1103/PhysRevB.50.17953.
[38] J.P. Perdew, K. Burke, M. Ernzerhof, Generalized gradient approximation made simple, Phys. Rev. Lett. 77 (1996) 3865–3868, https://doi.org/10.1103/PhysRevLett. 77.3865.
[39] S. Grimme, S. Ehrlich, L. Goerigk, Effect of the damping function in dispersion corrected density functional theory, J. Comput. Chem. 32 (2011) 1456–1465, https://doi.org/10.1002/jcc.21759.
[40] S. Grimme, J. Antony, S. Ehrlich, H. Krieg, A consistent and accurate ab initio parametrization of density functional dispersion correction (DFT-D) for the 94 elements H-Pu, J. Chem. Phys. 132 (2010) 154104, https://doi.org/10.1063/1.3382344.
[41] G. Henkelman, H. Jónsson, Improved tangent estimate in the nudged elastic band method for finding minimum energy paths and saddle points, J. Chem. Phys. 113 (2000) 9978–9985, https://doi.org/10.1063/1.1323224.
[42] H. Jónsson, G. Mills, K.W. Jacobsen, Nudged elastic band method for finding minimum energy paths of transitions, in: B.J. Berne, G. Ciccotti, D.F. Coker (Eds.), Classical and Quantum Dynamics in Condensed Phase Simulations, World Scientific, 1998, pp. 385–404, https://doi.org/10.1142/9789812839664_0016.
[43] G. Henkelman, H. Jónsson, A dimer method for finding saddle points on high dimensional potential surfaces using only first derivatives, J. Chem. Phys. 111 (1999) 7010–7022, https://doi.org/10.1063/1.480097.
[44] A.J. Jones, E. Iglesia, The strength of brønsted acid sites in microporous aluminosilicates, ACS Catal. 5 (2015) 5741–5755, https://doi.org/10.1021/acscatal.5b01133.
[45] A. Hoffman, M. DeLuca, D. Hibbitts, Restructuring of MFI framework zeolite models and their associated artifacts in density functional theory calculations, J. Phys. Chem. C. 123 (2019) 6572–6585, https://doi.org/10.1021/acs.jpcc.8b12230.
[46] D.A. McQuarrie, Statistical Mechanics, University Science Books, Sausalito, Calif, 2000.
[47] S. Herrmann, E. Iglesia, Elementary steps in acetone condensation reactions catalyzed by aluminosilicates with diverse void structures, J. Catal. 346 (2017) 134–153, https://doi.org/10.1016/j.jcat.2016.12.011.
[48] M. DeLuca, P. Kravchenko, A. Hoffman, D. Hibbitts, Mechanism and Kinetics of Methylating C6–C12 Methylbenzenes with Methanol and Dimethyl Ether in H-MFI Zeolites, ACS Catal. 9 (2019) 6444–6460, https://doi.org/10.1021/acscatal.9b00650.
[49] R. Gounder, E. Iglesia, The catalytic diversity of zeolites: confinement and solvation effects within voids of molecular dimensions, Chem. Commun. 49 (2013) 3491–3509, https://doi.org/10.1039/c3cc40731d.
[50] S. Wang, E. Iglesia, Catalytic diversity conferred by confinement of protons within porous aluminosilicates in Prins condensation reactions, J. Catal. 352 (2017) 415–435, https://doi.org/10.1016/j.jcat.2017.06.012.
[51] G. Mirth, J.A. Lercher, M.W. Anderson, J. Klinowski, Adsorption complexes of methanol on zeolite ZSM-5, Faraday Trans. 86 (1990) 3039–3044, https://doi.org/10.1039/ft9908603039.
[52] C.A. Farberow, J.A. Dumesic, M. Mavrikakis, Density functional theory calculations and analysis of reaction pathways for reduction of nitric oxide by hydrogen on Pt(111), ACS Catal. 4 (2014) 3307–3319, https://doi.org/10.1021/cs500668k.
[53] P. Deshlahra, R.T. Carr, E. Iglesia, Ionic and covalent stabilization of intermediates and transition states in catalysis by solid acids, J. Am. Chem. Soc. 136 (2014) 15229–15247, https://doi.org/10.1021/ja506149c.
[54] P. Deshlahra, R.T. Carr, S.-H. Chai, E. Iglesia, Mechanistic details and reactivity descriptors in oxidation and acid catalysis of methanol, ACS Catal. 5 (2015) 666–682, https://doi.org/10.1021/cs501599y.
[55] P.L. Llewellyn, E. Bloch, S. Bourrelly, Surface area/porosity, adsorption, diffusion, in: M. Che, J.C. Védrine (Eds.), Characterization of Solid Materials and Heterogeneous Catalysts: From Structure to Surface Reactivity, Wiley-VCH Verlag GmbH & Co. KGaA, Weinheim, Germany, 2012, pp. 853–879, https://doi.org/10.1002/9783527645329.ch19.
[56] M. Thommes, Physical adsorption characterization of nanoporous materials, Chemie Ingenieur Technik. 82 (2010) 1059–1073, https://doi.org/10.1002/cite.201000064.
[57] W.S. Borghard, P.T. Reischman, E.W. Sheppard, Argon Sorption in ZSM-5, J. Catal. 139 (1993) 19–23, https://doi.org/10.1006/jcat.1993.1002.
[58] W. Knaeble, E. Iglesia, Kinetic and theoretical insights into the mechanism of Alkanol dehydration on solid Brønsted acid catalysts, J. Phys. Chem. C. 120 (2016) 3371–3389, https://doi.org/10.1021/acs.jpcc.5b11127.
[59] T.J. Wilke, M.A. Barteau, Cation exchange effects on methanol oxidation and dehydration by supported polyoxometalates, J. Catal. 371 (2019) 357–367, https://doi.org/10.1016/j.jcat.2019.02.006.
[60] J. Towns, T. Cockerill, M. Dahan, I. Foster, K. Gaither, A. Grimshaw, et al., XSEDE: accelerating scientific discovery, Comput. Sci. Eng. 16 (2014) 62–74, https://doi.org/10.1109/MCSE.2014.80.

Supporting Information

Mechanistic Origins of the High-Pressure Inhibition of Methanol Dehydration Rates in Small-Pore Acidic Zeolites

John R. Di Iorio,[1] Alexander J. Hoffman,[2] Claire T. Nimlos,[1] Steven Nystrom,[2] David Hibbitts,*[2] Rajamani Gounder*[1]

[1]*Charles D. Davidson School of Chemical Engineering, Purdue University, 480 Stadium Mall Drive, West Lafayette, IN 47907, USA*

[2]*Department of Chemical Engineering, University of Florida, 1030 Center Drive, Gainesville, FL 32611, USA*

*Corresponding author. E-mails: hibbitts@ufl.edu, rgounder@purdue.edu

Table of Contents

List of Figures, Tables, and Schemes

S.1. Statistical mechanics approximations for rate and equilibrium constants

Enthalpies (H) and free energies (G) for gas-phase and adsorbed species are calculated as a sum of DFT-calculated electronic energy (E_0), zero-point vibrational energy (ZPVE), and vibrational, translational, and rotational enthaplies (H_{vib}, H_{trans}, H_{rot}) and free energies (G_{vib}, G_{trans}, G_{rot}):

$$H = E_0 + ZPVE + H_{vib} + H_{trans} + H_{rot} \tag{S.1}$$

$$G = E_0 + ZPVE + G_{vib} + G_{trans} + G_{rot} \tag{S.2}$$

Motions of adsorbates within the zeolite framework were considered frustrated movements and only contributed to vibrational terms such that translational and rotational H and G were zero. Framework Al atoms and the four O atoms bound to them were included in normal mode analysis, but all remaining framework Si and O atoms remained static during frequency calculations. Vibrational, rotational, and translational energies were calculated from statistical mechanics [1]:

$$ZPVE = \sum_i \left(\frac{1}{2} h\nu_i\right) \tag{S.3}$$

$$H_{vib} = \sum_i \left(\frac{h\nu_i e^{\frac{-h\nu_i}{k_B T}}}{1-e^{\frac{-h\nu_i}{k_B T}}} \right) \tag{S.4}$$

$$G_{vib} = \sum_i \left(-k_B T \ln \left(\frac{1}{1-e^{\frac{-h\nu_i}{k_B T}}} \right) \right) \tag{S.5}$$

Translational and rotational free energies and enthalpies were calculated for all gas-phase species:

$$H_{trans} = \frac{5}{2} k_B T \tag{S.6}$$

$$H_{rot,linear} = k_B T \tag{S.7}$$

$$H_{rot,nonlinear} = \frac{3}{2} k_B T \tag{S.8}$$

$$G_{trans} = -k_B T \ln \left(\left(\frac{2\pi M k_B T}{h^2} \right)^{\frac{3}{2}} V \right) \tag{S.9}$$

$$G_{rot} = -k_B T \ln \left(\frac{\pi^{\frac{1}{2}}}{\sigma} \left(\frac{T^3}{\theta_x \theta_y \theta_z} \right)^{\frac{1}{2}} \right) \tag{S.10}$$

$$\theta_i = \frac{h^2}{8\pi^2 k_B I_i} \tag{S.11}$$

where I_i is the moment of inertial about each axis and σ is the symmetry number. Entropies (S) are calculated from H and G:

$$S = \frac{H-G}{T} \tag{S.12}$$

G values at a wide range of temperatures (300–500 K) were estimated from H and S values calculated at 415 K.

Rate constants can be approximated from DFT-calculated enthalpies and free energies at a range of temperatures using statistical mechanics formalisms:

$$k = \frac{k_B T}{h} \exp\left(\frac{-\Delta G^{\ddagger}}{k_B T}\right) \tag{S.13}$$

$$K = \exp\left(\frac{-\Delta G_{ads}}{k_B T}\right) \tag{S.14}$$

where k_B is Boltzmann's constant. Rate and equilibrium constants are calculated at standard pressures (1 bar CH_3OH).

S.2. Configurational effects on calculated energies for intermediates and transition states

The CHA framework has four distinct O atoms around its only unique T-site; these O atoms are show in Figure S.1 with the rings of the CHA framework. A proton (which can accommodate H-bound adsorbates), methyl group, or transition state can interact with each of these O atoms. This multiplicity of locations for binding lends itself to configurational complexity in theory approaches to studying zeolites. Moreover, the plethora of confining environments within zeolites—even those with high symmetry, such as CHA—further compounds this configurational complexity.

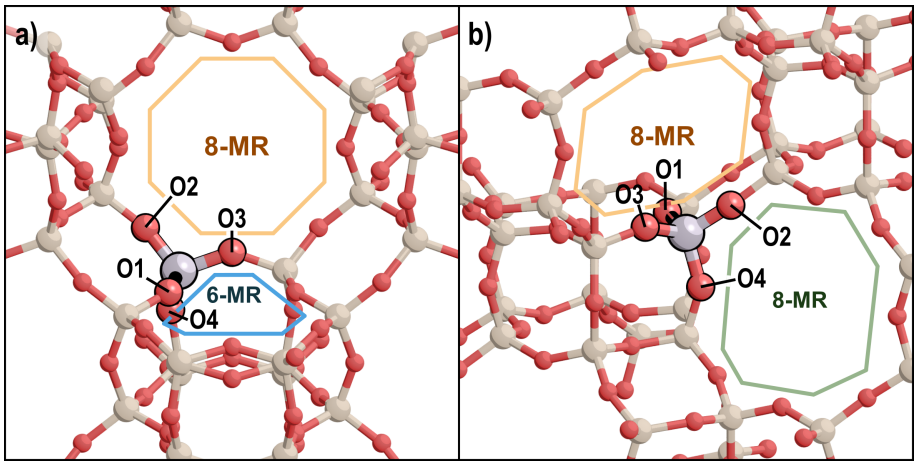

Figure S.1. CHA structure with Al substituted for a Si atom. Symmetrically unique O atoms around this Al atom are labeled from convention [2]. (a) The six-member (6-MR) and eight-member (8-MR) rings containing O1, O2, and O3 of the Al atom; (b) another view showing the two 8-MR shared by O2 of the Al containing O2, O3, and O4.

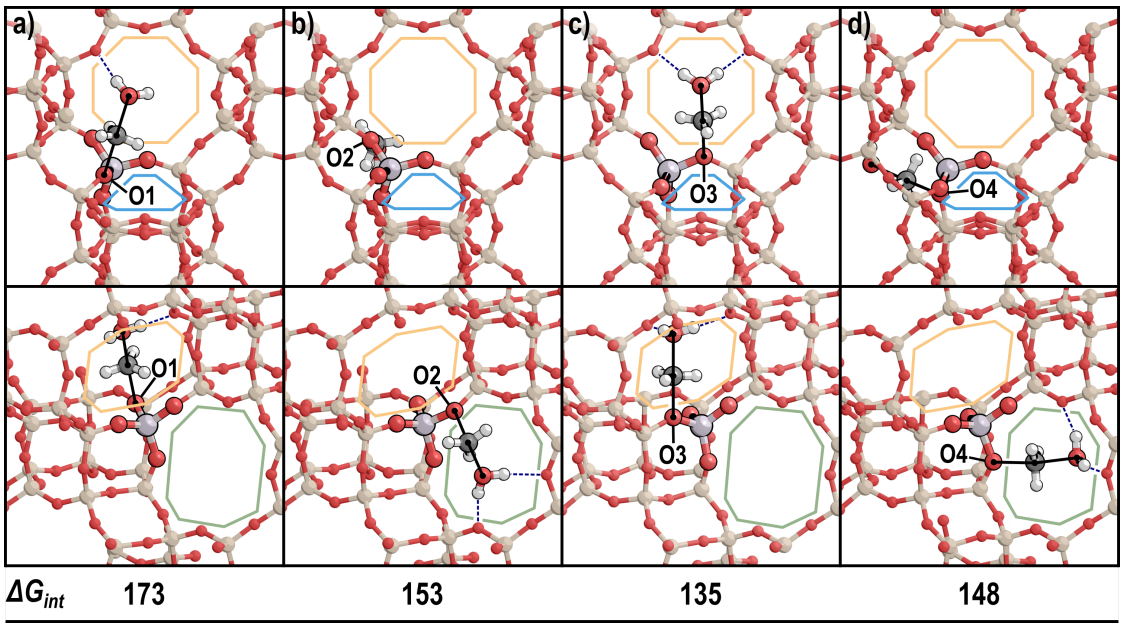

Figure S.2. The lowest energy transition states for the first step of the dissociative mechanism without spectators on (a) O1, (b) O2, (c) O3, and (d) O4. H-bonds are shown with blue dashed lines and incipient and breaking bonds are shown with black lines. The O atom with which the transition state is interacting is labeled. Intrinsic free energy barriers (ΔG_{int}) are shown in kJ mol^{-1} also relative to one adsorbed methanol.

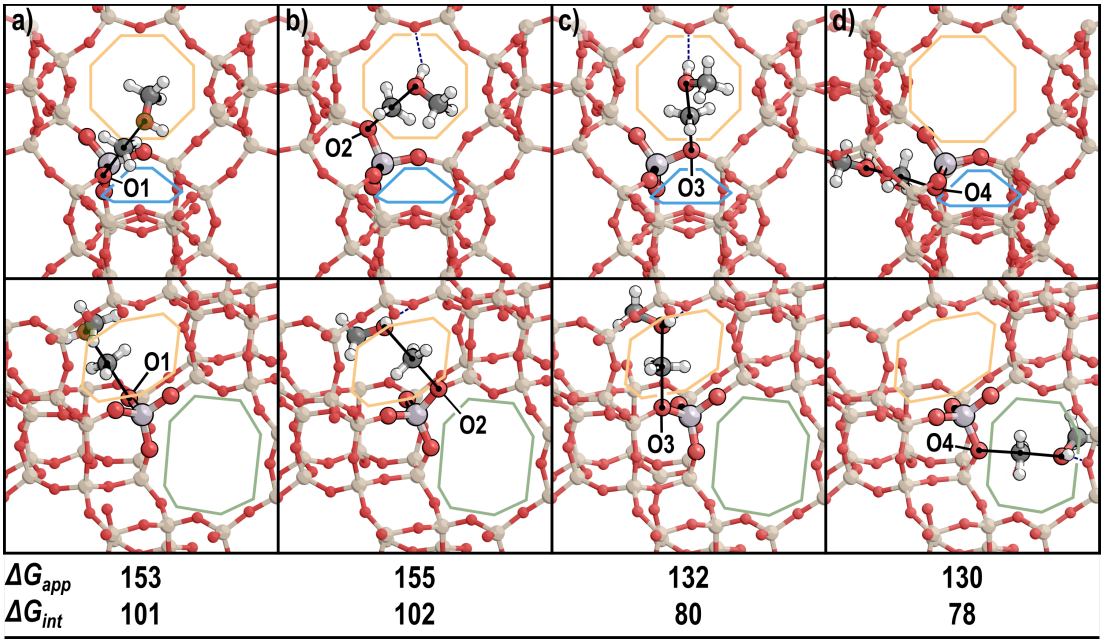

Figure S.3. The lowest energy transition states for the second step of the dissociative mechanism without spectators on (a) O1, (b) O2, (c) O3, and (d) O4. H-bonds are shown with blue dashed lines and incipient and breaking bonds are shown with black lines. The O atom with which the transition state is interacting is labeled. Apparent free energy (ΔG_{app}) barriers are shown in kJ mol^{-1} relative to one adsorbed methanol. Intrinsic free energy barriers (ΔG_{int}) are shown in kJ mol^{-1}.

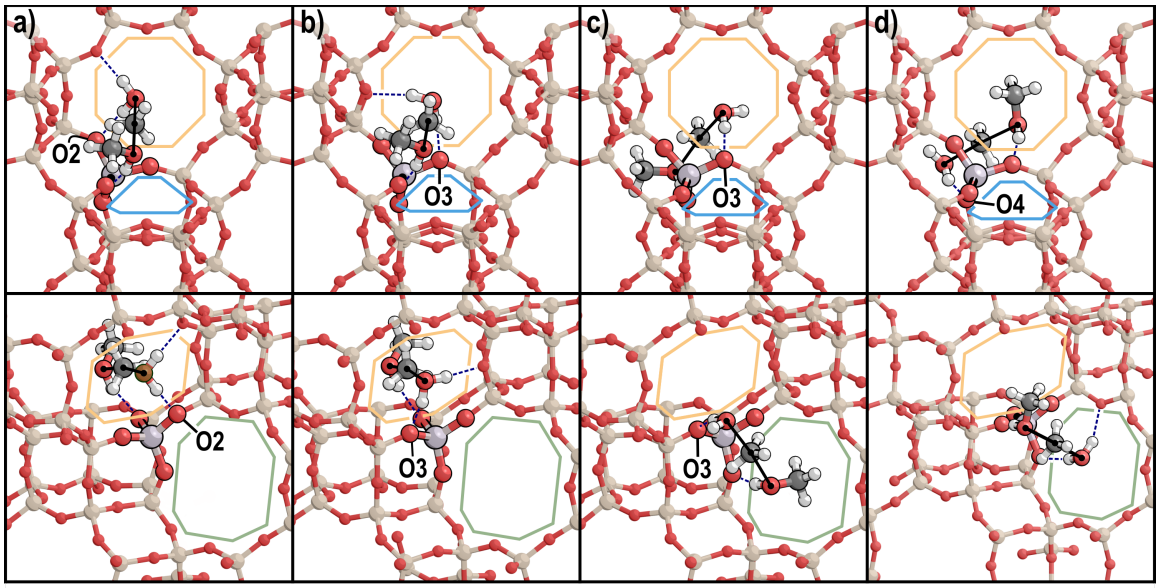

	a)	b)	c)	d)
ΔG_{app}	126	128	149	123
ΔG_{int}	140	141	163	137

Figure S.4. The four lowest energy transition states for the associative mechanism without spectators with the with (a) the water H-bonding with O2 and methanol H-bonding with O1, (b) the water H-bonding with O3 and methanol H-bonding with O1, (c) the water H-bonding with O3 and methanol H-bonding with O4, and (d) the water H-bonding with O4 and methanol H-bonding with O3. H-bonds are shown with blue dashed lines and incipient and breaking bonds are shown with black lines. The O atom with which the water is interacting is labeled. Apparent free energy (ΔG_{app}) and enthalpic (ΔH_{app}) barriers are shown in kJ mol^{-1} and apparent entropies (ΔS_{app}) in J mol^{-1} K, relative to one adsorbed methanol. Intrinsic free energy barriers (ΔG_{int}) are shown in kJ mol^{-1} also relative to one adsorbed methanol.

S.3. Comparison of dissociative and associative mechanisms without spectating methanol molecules

Methanol dehydration, if it proceeds via the dissociative route, can be limited by either of the two steps in that pathway. The relative rates of the two pathways can be assessed by computing rates using a maximum rate analysis (as seen in Section 3.5 of the main text) or by comparing the forward and reverse reactions possible from a surface methyl group. A surface methyl group during methanol dehydration can either (1) react with water to re-form methanol or (2) react with another methanol to form dimethyl ether (DME) (Scheme S.1). Coefficients of adsorption in the presence of a CH_3–Z species for H_2O (K_{W-M}) and CH_3OH (K_{M-M}) define adsorption steps prior to reaction to form DME (k_{D2}) or to re-form methanol (k_{-D1}).

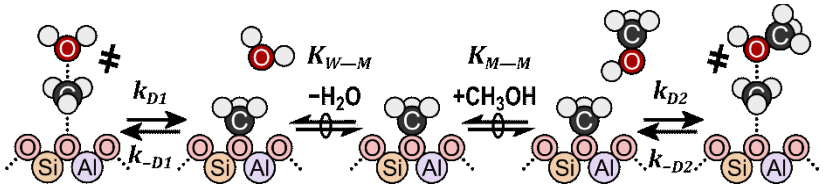

Scheme S.1. The possible routes to remove a surface methyl (CH_3–Z) group during methanol dehydration.

Based on the paths described in Scheme S.1, rate equations can be derived to describe the formation of methanol from this surface methyl:

$$r_{-D1} = k_{-D1} K_{W-M} P_{H_2O} \tag{S.15}$$

or to describe the formation of DME:

$$r_{D2} = k_{D2} K_{M-M} P_{CH_3OH} \tag{S.16}$$

The ratios of these rates can be written as a function of conversion (X) to compare the relative rates of these two steps and determine the rate-determining step (RDS) of the dissociative mechanism:

$$\frac{r_{-D1}}{r_{D2}} = \frac{k_{-D1} K_{W-M}}{k_{D2} K_{M-M}} \left(\frac{X}{1-X} \right) \tag{S.17}$$

Using energies calculated from DFT, these rate and equilibrium constants can be calculated from statistical mechanics formalisms (Section S.1) (415 K, 1 bar CH_3OH). Ultimately, the ratio of these rate and equilibrium coefficients reflects the difference in energy between the two transition states:

$$\frac{k_{-D1} K_{W-M}}{k_{D2} K_{M-M}} = \exp\left(\frac{-\left(\Delta G^{\ddagger}_{D1} - \Delta G^{\ddagger}_{D2} \right)}{k_B T} \right) \tag{S.18}$$

These calculated values were used to estimate the ratio of rates of methanol formation and DME formation from a CH_3–Z group at different conversions using Eq. S.17 (Fig. S.5). The rate of the second step of the dissociative mechanism exceeds the reverse rate of the first step by at least a factor of 10 at all conversions tested experimentally. This indicates that the first step of the dissociative route can be considered irreversible and is the RDS at all relevant catalytic conditions when spectating methanol species are excluded.

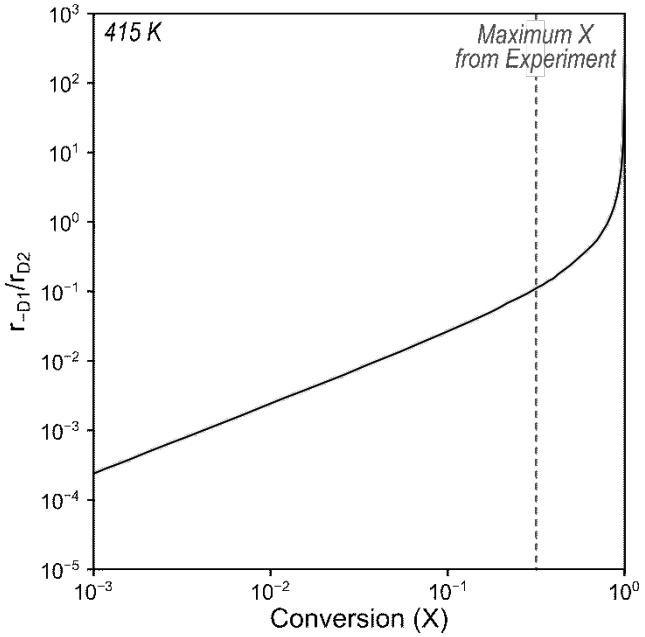

Figure S.5. Ratio of rates of the two possible rate-determining steps in dissociative methanol dehydration at 415 K. The maximum conversion tested experimentally is marked with a dashed line.

The relative rates of the dissociative mechanism (which is limited by its first step at relevant conditions) and the associative mechanism can be compared using maximum rate analysis. DFT-calculated enthalpies and entropies can be used to approximate rate and equilibrium constants at standard conditions (Section S.1), from which rates can be estimated using the appropriate rate equations. The rate equation for the dissociative mechanism without spectators and without considering anything larger than a methanol dimer as a most abundant surface intermediate (MASI) is:

$$r_{D1} = \frac{k_{D1} K_M P_M}{1 + K_M P_M + K_M K_D P_M^2} \tag{S.19}$$

The rate equation for the associative mechanism with the same assumptions is

$$r_A = \frac{k_A K_M K_D P_M^2}{1 + K_M P_M + K_M K_D P_M^2} \tag{S.20}$$

The ratio of these two rates, therefore, is

$$\frac{r_D}{r_A} = \frac{k_D}{k_A K_D P_M} \tag{S.21}$$

The ratio of these rate coefficients reflects the differences in free energy between the dissociative ($\Delta G_{D1}^{\ddagger}$) and associative ($\Delta G_A^{\ddagger}$) transition states and a methanol dimer structure (ΔG_D):

$$\frac{k_D}{k_A K_D} = \exp\left(-\frac{\left(\Delta G_{D1}^{\ddagger} - \Delta G_A^{\ddagger} - \Delta G_D\right)}{k_B T}\right) \tag{S.22}$$

The dissociative mechanism prevails at low methanol pressures, but the associative mechanism dominates at higher pressures (Fig. S.6). The pressure at which the prevalent mechanism shifts from dissociative to associative increases with increasing temperature. This reflects differences

in enthalpic and entropic contributions to relevant free energies; the associative mechanism is enthalpically favored but entropically disfavored as adsorption of additional methanol molecules results in entropic losses. This is consistent with previous work which has found a preference for the dissociative mechanism at elevated reaction temperatures in MFI [5] and on polyoxometalates [6] due to entropic contributions to the free energies for these mechanisms.

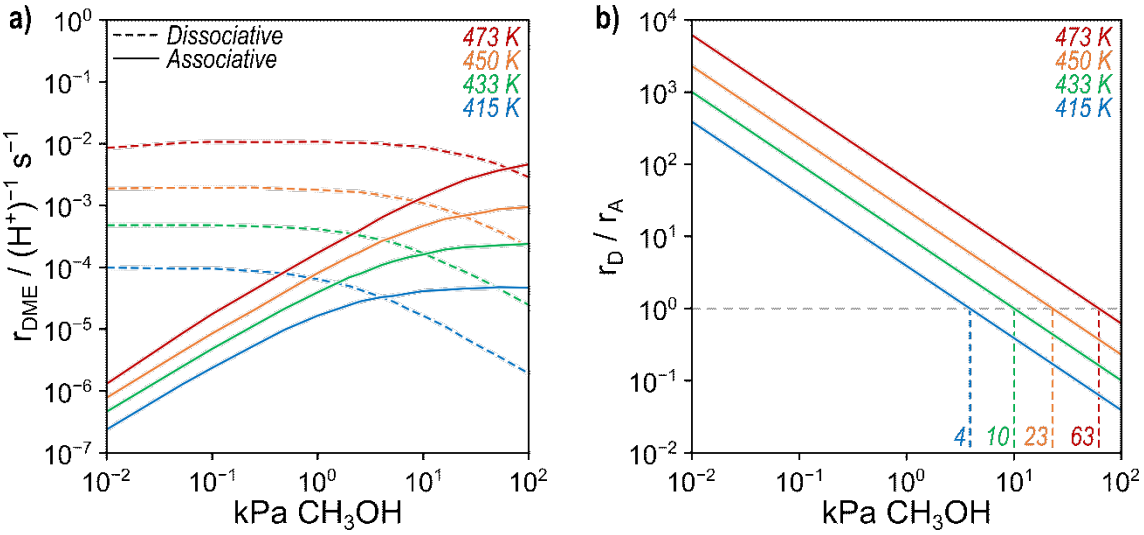

Figure S.6. (a) DFT-predicted rates of dissociative (dashed lines) and associative (solid lines) methanol dehydration without spectators and excluding intermediates larger than two methanol molecules at 415 K (blue), 433 K (green), 450 K (orange), and 473 K (red). (b) Ratios of the dissociative and associative rates of DME formation at these temperatures, with the pressures at which the prevailing route shifts from dissociative to associative labeled in kPa.

S.4. Purification and drying of reactant methanol

Additional water may also have entered the system via the reactant methanol and this was also considered as a possible source of water contamination. Methanol (99.9 wt%, HPLC-grade, Sigma-Aldrich) was further purified by first removing dissolved gases (e.g., N_2, O_2) via freeze-pump-thaw until the equilibrium vapor pressure of methanol at room temperature (13.6 kPa at ~294 K) was reached and no bubbling was observed upon thawing (an indication of volatile contaminants). After the freeze-pump-thaw cycles, methanol was then refluxed overnight (338 K) under an Ar atmosphere (99.999%, Indiana Oxygen) to minimize the presence of volatile organic contaminants (e.g., formaldehyde) [7]. Finally, methanol was then transferred via a double-ended cannula to a round-bottom flask containing dehydrated 3A molecular sieves (dried at 523 K under dynamic vacuum overnight (<5 Pa); Sigma-Aldrich) held under an Ar atmosphere and left overnight to remove residual water. This dried, degassed methanol was then transferred via gas-tight syringe, to the syringe pump and used as the reactant feed. Methanol dehydration rates (per H^+, 415 K) using this purified methanol are indistinguishable from those measured with unpurified methanol and are inhibited to a similar extent at high methanol pressures (>10 kPa; Fig. S.7).

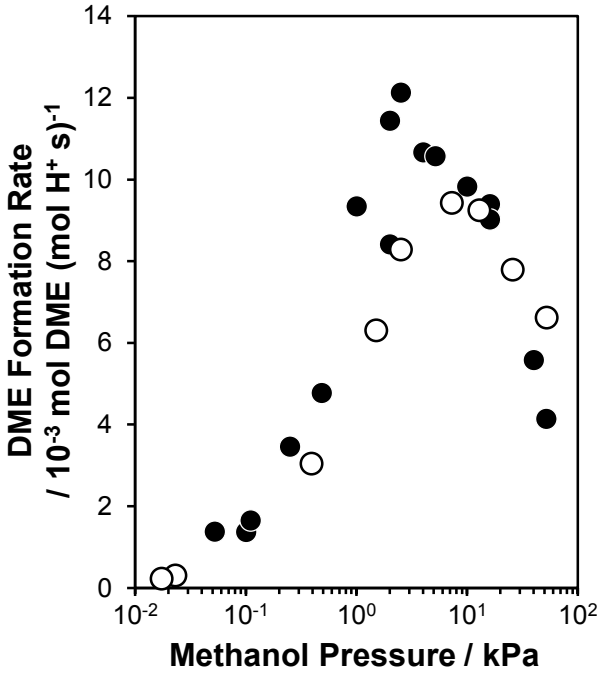

Figure S.7. DME formation rate (per H^+, 415 K) measured on H-CHA with only isolated H^+ sites as a function of methanol pressure using unpurified (solid) and purified methanol (open).

S.5. DFT-calculated methanol cluster stability

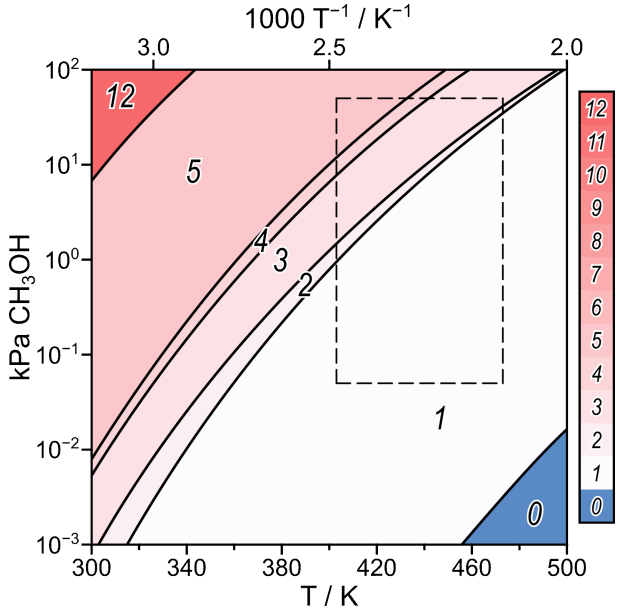

Figure S.8. Phase diagram predicting the most stable methanol cluster size at isolated H^+ sites in CHA, denoted by the phase boundary lines in the figure and the colored legend to the right of the figure. Equilibrium constants for adsorption were predicted by free energies from DFT at 415 K and 1 bar CH_3OH. The area enclosed by dashed lines correspond to the range of kinetic conditions studied for methanol dehydration in this work (403–473 K, 0.05–50 kPa CH_3OH).

S.6. ^{1}H NMR spectrum of 1,2-dimethyl-3-(4-methylbenzyl)imidazolium chloride

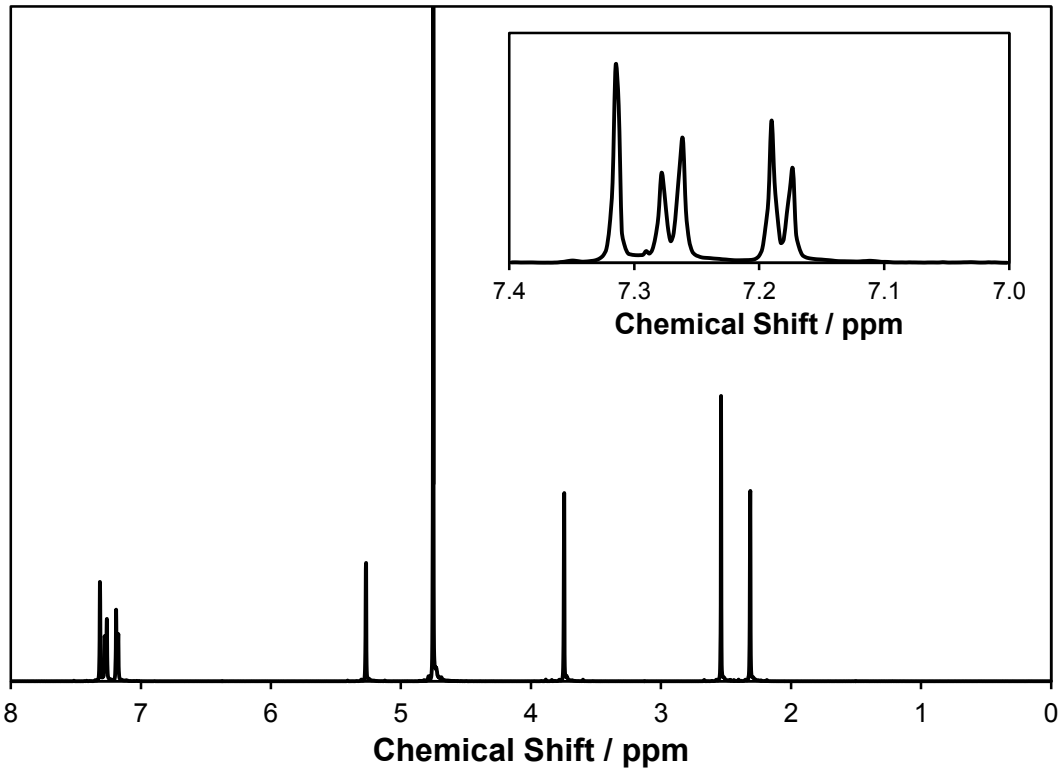

Figure S.9. ^{1}H NMR spectrum of 1,2-dimethyl-3-(4-methylbenzyl)imidazolium chloride in D_2O. Peak at ~4.7 ppm is due to residual H_2O present in the D_2O solvent. Inset shows a zoom in to the region between 7.4-7.0 ppm.

The overall reaction for the synthesis of 1,2-dimethyl-3-(4-methylbenzyl)imidazolium chloride is shown in Scheme S.2 and the assigned chemical shifts of each H atom of the product are shown in Scheme S.3. Notably, only a single resonance is observed for the two olefinic H atoms of the imidazolium ring (δ: 7.31 ppm; Fig. S.9, inset). Integration of this peak indicates that 2 H atoms share this chemical shift and is likely representative of a resonance structure of the delocalized imidazolium cation where the charge is shared across the N atoms (Scheme S.3) [8].

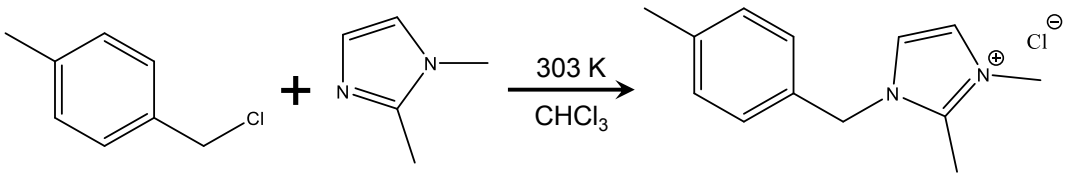

Scheme S.2. Overall reaction between 4-methylbenzyl chloride and 1,2-dimethylimidazole to form 1,2-dimethyl-3-(4-methylbenzyl)imidazolium chloride.

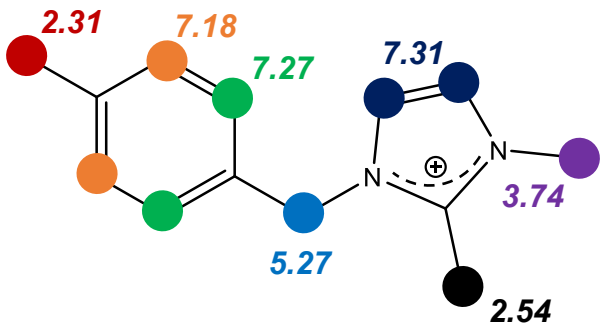

Scheme S.3. Proposed resonance structure of the imidazolium cation. Colored circles are used to distinguish chemically distinct H atoms (not shown) and their corresponding ^{1}H NMR chemical shifts (in ppm). ^{1}H NMR (D_2O, 500 MHz): δ 7.31 (s, 2H), 7.27 (d, 2H), 7.18 (d, 2H), 5.27 (s, 2H), 3.74 (s, 3H), 2.54 (s, 3H), 2.31 (s, 3H).

S.7. Powder X-ray diffraction patterns of different small-pore zeolites

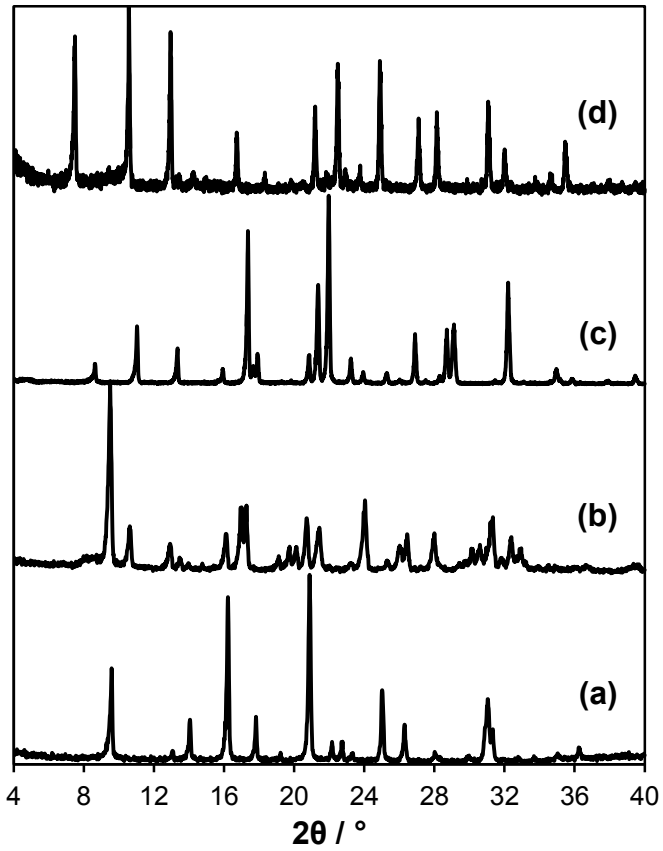

Figure S.10. Powder XRD patterns of (a) CHA, (b) AEI, (c) LEV, and (d) LTA zeolites.

S.8. Argon adsorption isotherms (87 K) on various small-pore zeolites

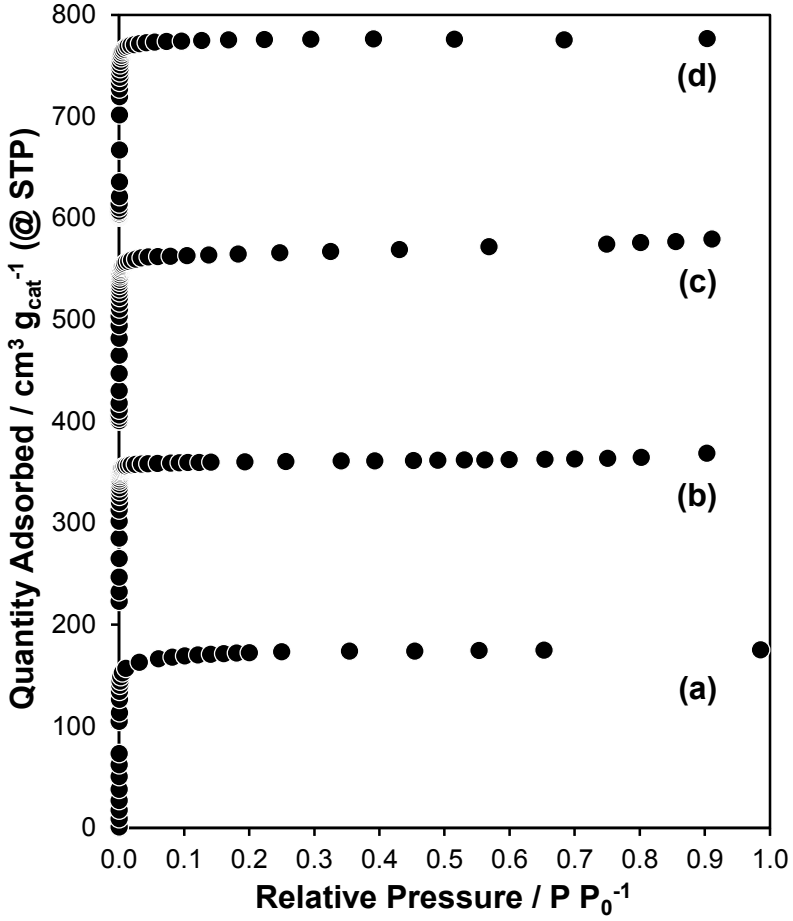

Figure S.11. Ar adsorption isotherms (87 K) measured on (a) CHA, (b) AEI, (c) LEV, and (d) LTA zeolites. Isotherms are vertically offset by 200 $cm^3 g_{cat}^{-1}$.

S.9. Tabulated micropore volumes, Al content, and H^+ site content on different small-pore zeolites

Table S.1. Micropore volumes estimated from Ar adsorption isotherms (87 K), total Al content measured by AAS, and H^+ site contents measured by NH_3 TPD on different small-pore zeolites.

Zeolite Framework	Micropore Volume / $cm^3\ g_{cat}^{-1}$ (@ STP)	Al Content 10^{-3} mol Al g_{cat}^{-1}	Si/Al	H^+ Site Content 10^{-3} mol H^+ g_{cat}^{-1}	H^+/Al
LTA	0.21	0.57	28	0.46	0.81
CHA	0.19	0.98	16	0.93	0.95
AEI	0.20	1.59	9.5	1.35	0.85
LEV	0.20	0.98	16	0.93	0.95

S.10. Measurement of methanol dehydration activation enthalpies and entropies on CHA zeolites

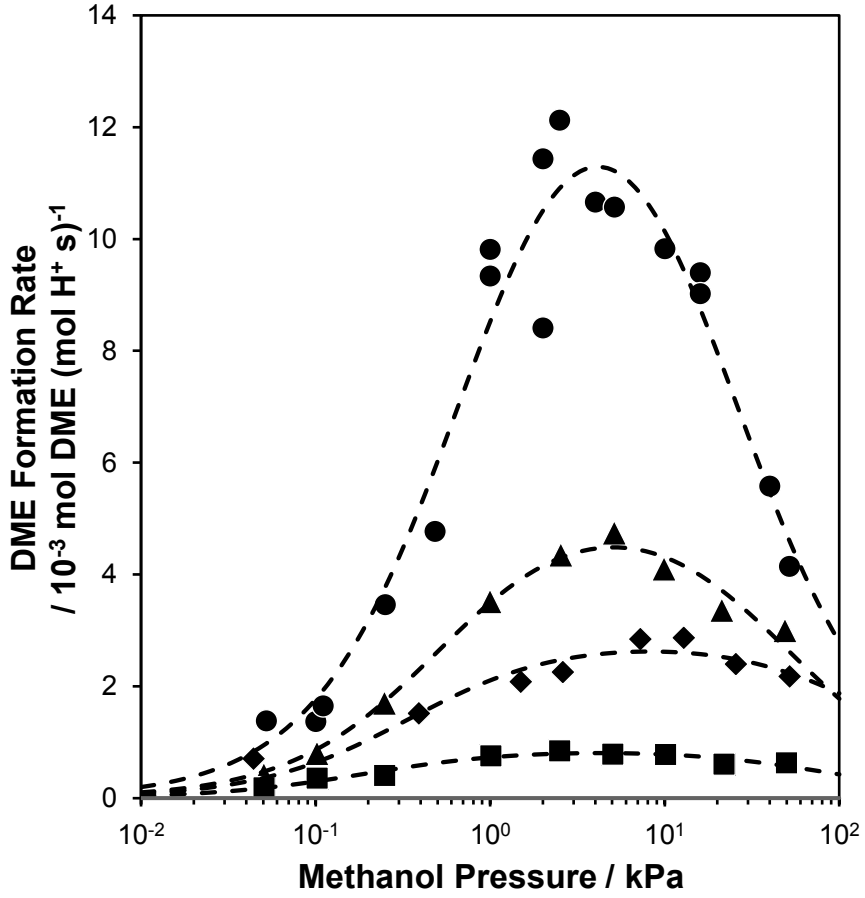

Figure S.12. DME formation rates measured as a function of methanol pressure at 383 (squares), 398 (diamonds), 403 (triangles), and 415 K (circles) on a CHA zeolite with only isolated H^+ sites. Dashed lines are least squares regressions to Eq. 4 (main text).

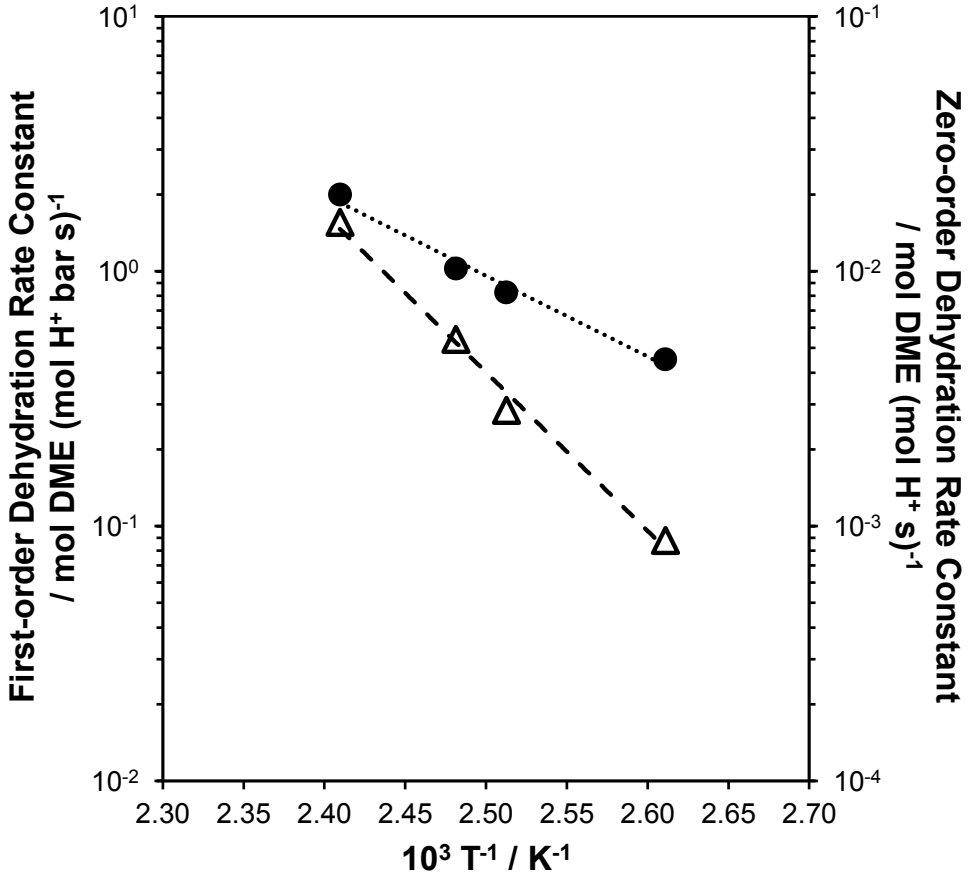

Figure S.13. First-order (circles) and zero-order (triangles) methanol dehydration rate constants (per H^+ site) measured as a function of temperature (383-415 K) on a CHA zeolite containing isolated H^+ sites.

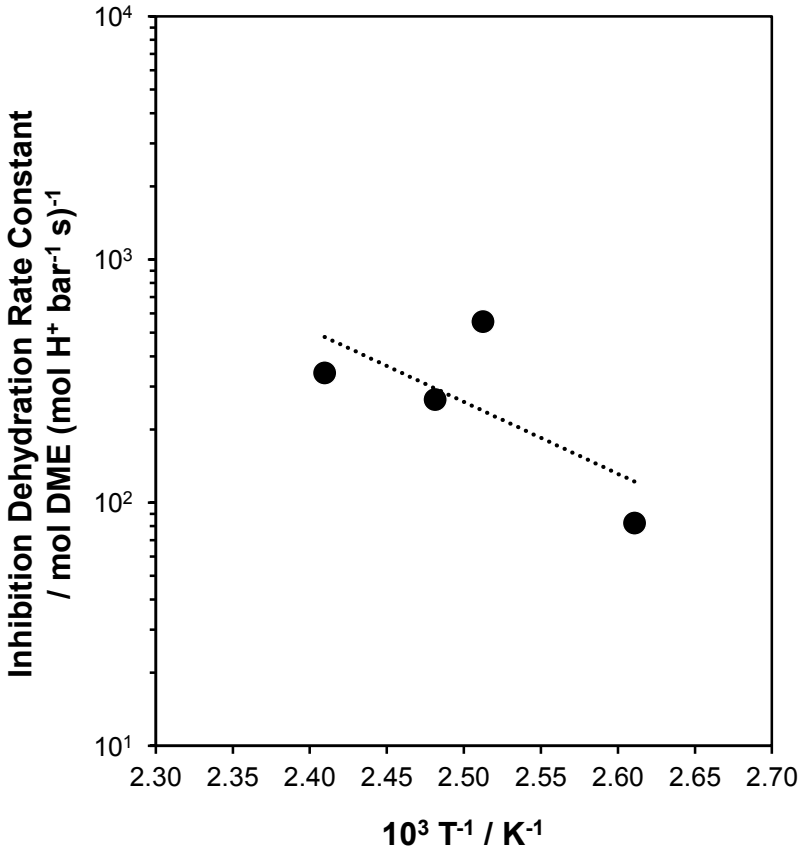

Figure S.14. Apparent inhibition methanol dehydration rate constant (per H^+ site) measured as a function of temperature (383-415 K) on a CHA zeolite containing only isolated H^+ sites.

First-order and zero-order apparent activation enthalpies and entropies were calculated from measured methanol dehydration rate constants (Fig. S.12 and S.13) using the Eyring-Polanyi equation [9,10]:

$$k = \frac{k_B T}{h} \exp\left(\frac{-\Delta G^{\ddagger}}{RT}\right) \tag{S.23}$$

where k_B is the Boltzmann constant, h is Planck's constant, R is the universal gas constant, and $\Delta G^{\ddagger}$ is the activation free energy. Eq. S.23 can be expanded in terms of activation enthalpies ($\Delta H^{\ddagger}$) and activation entropies ($\Delta S^{\ddagger}$):

$$k = \frac{k_B T}{h} \exp\left(\frac{-\Delta H^{\ddagger}}{RT}\right) \exp\left(\frac{\Delta S^{\ddagger}}{R}\right) \tag{S.24}$$

and then linearized as follows:

$$\ln\left(\frac{k}{T}\right) - \ln\left(\frac{k_B}{h}\right) = -\frac{-\Delta H^{\ddagger}}{RT} + \frac{\Delta S^{\ddagger}}{R} \tag{S.25}$$

Apparent first-order and zero-order activation parameters for methanol dehydration on isolated H^+ sites in CHA zeolites are listed in Table S.2.

Table S.2. First-order, zero-order, and inhibition apparent activation enthalpies ($\Delta H^{\ddagger}$), entropies ($\Delta S^{\ddagger}$), and Gibbs free energies ($\Delta G^{\ddagger}$) measured on CHA with only isolated H^+ sites (383-415 K).

	$\Delta H^{\ddagger}$ / kJ mol^{-1}	$\Delta S^{\ddagger}$ / J mol^{-1} K^{-1}	$\Delta G^{\ddagger}$(415 K) / kJ mol^{-1}
First-order	61	-95	100
Zero-order	115	-7	117
Inhibition	50	-280	165

Rates of methanol dehydration were also measured at elevated temperatures on CHA with only isolated Al sites (up to 473 K, Fig. 7a) and are shown here without a logarithmic pressure scale (Fig. S.14).

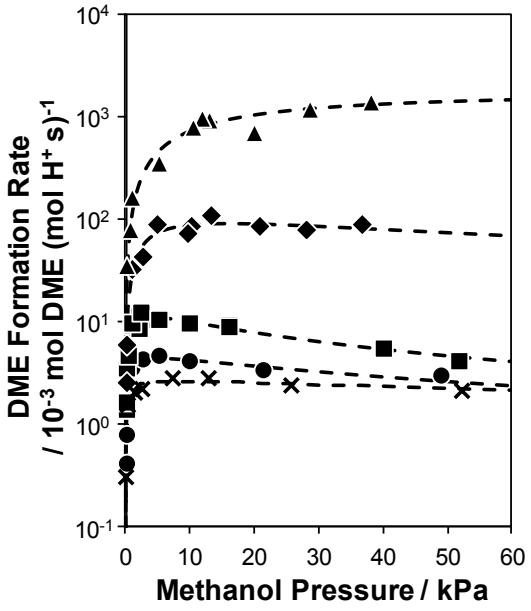

Figure S.15. DME formation rates (per H^+) measured at 398 K (crosses), 403 K (circles), 415 K (squares), 433 K (diamonds), and 473 K (triangles) as a function of temperature (403-473 K) on CHA with only isolated H^+ sites.

DME formation rates (per H^+) were also measured on a CHA zeolite containing 24% paired H^+ sites as a function of temperature (403-473 K) and high-pressure inhibition was also observed to become attenuated at elevated reaction temperatures (>433 K, Fig. S.15).

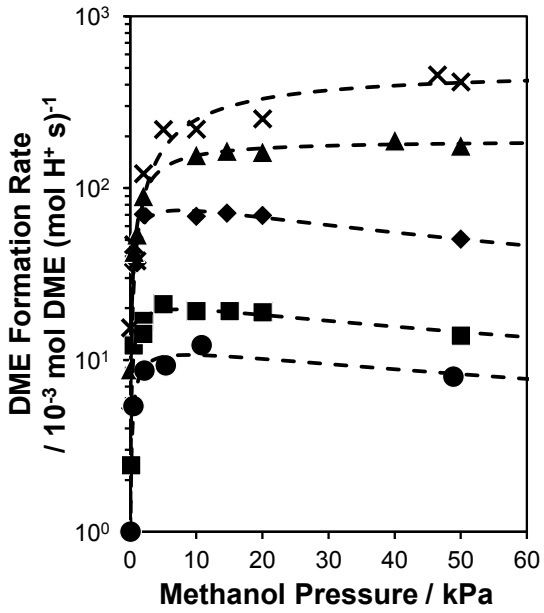

Figure S.16. DME formation rates (per H^+) measured at 403 K (circles), 415 K (squares), 433 K (diamonds), 450 K (triangles), and 473 K (crosses) as a function of temperature (403-473 K) on CHA with 24% paired H^+ sites.

An interesting observation is that high-pressure inhibition appears to become more severe with increasing temperature in the low temperature regime (383-415 K; Fig. S.12), but disappears with increasing temperature above 433 K (Fig. 7a). At low-temperatures (<415 K), both apparent first-order and zero-order rate constants follow an Arrhenius dependence on temperature (383-415 K; Fig. S.13), and the same is true for the apparent inhibition rate constant extracted using Eq. 4 in the main text (Fig. S.14). There does appear to be an outlier in this data set (398 K; Fig. S.14), but removal of this data point does not change the magnitude of the calculated activation enthalpy or entropy substantially (<20% variation). The values of $\Delta H_{inhibit}$ and $\Delta S_{inhibit}$ (Table S.2) suggest that the inhibition is governed largely by entropic penalties likely due to the disruption of partially-ordered methanol structures that form at low-temperatures (<415 K; Fig. 15, main text) and this manifests in more severe inhibition with increasing temperature under these conditions (<415 K), as is observed in Fig. S.12. The formation of larger methanol clusters from gaseous methanol becomes less favorable with increasing temperature (Fig. 11, main text; Section S.15, SI) due to the entropic penalty required for confining multiple methanol molecules within the pores of CHA zeolites. As a result, the surface coverage shifts from a trimer and tetramer covered surface to a monomer and dimer covered surface at elevated reaction temperature (>433 K). This diminished presence of larger methanol clusters at elevated temperatures (>433 K) manifests itself in the disappearance of rate inhibition at high methanol partial pressures (>20 kPa) and gives rise to the trend observed in Fig. 7a of the main text. Ultimately, the trends observed at high methanol pressures (>20 kPa) and increasing temperature (383-473 K) can be rationalized by a trade-off in difference in the entropic barriers for the formation of large adsorbed methanol clusters from gaseous methanol

(e.g., trimers and tetramers) and the formation of the dehydration transition state from such clusters.

S.11. Methanol adsorption isotherm on a CHA zeolite

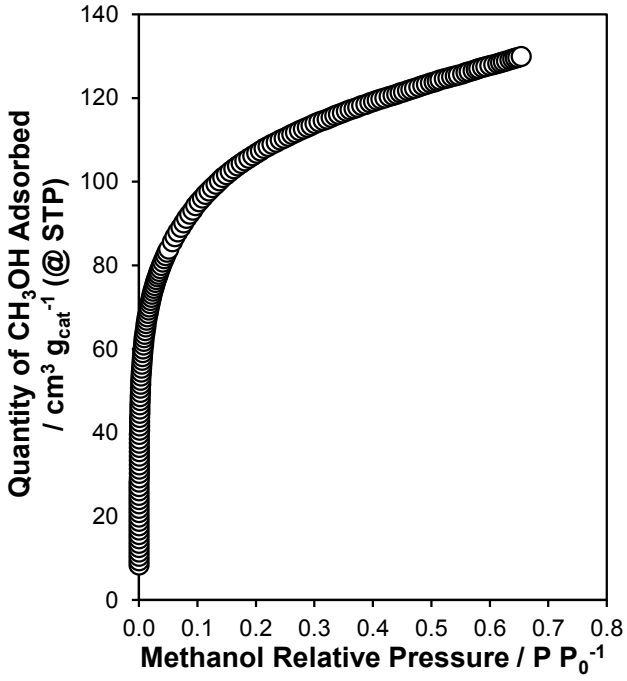

Figure S.17. Methanol adsorption isotherm measured at 293 K as a function of methanol relative pressure on isolated H^+ sites in CHA.

A methanol adsorption isotherm was also measured on a purely siliceous CHA zeolite for comparison and is shown in Fig. S.18. The relative methanol pressure required to adsorb ~10 $cm^3\ g_{cat}^{-1}$ (@STP) of methanol on Si-CHA compared to CHA containing only isolated H^+ sites is nearly 4 orders of magnitude larger ($5x10^{-2}$ vs. $6.8x10^{-6}$ P P_0^{-1}), suggesting that these dispersive interactions are significantly weaker than the interactions between methanol and H^+ sites or other adsorbed methanol molecules.

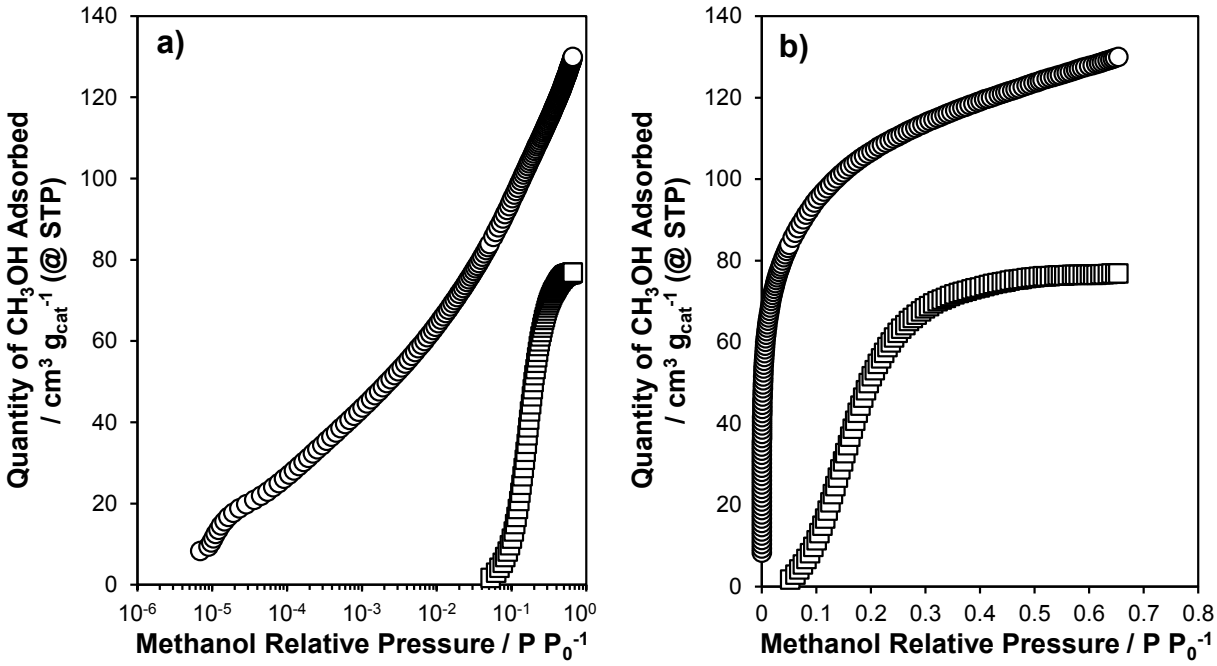

Figure S.18. Methanol adsorption isotherm measured at 293 K on a purely siliceous CHA zeolite (squares) and on an aluminosilicate CHA containing only isolated H^+ sites (Si/Al = 15; circles) as a function of a log (a) and linear (b) relative pressure scale.

S.12. Estimation of methanol conversion as a function of space velocity

Reversible dehydration of surface methoxy species relevant to the dissociative dehydration mechanism gives rise to a rate expression that is predicted to show a strong dependence on methanol conversion (Eq. 7, main text). Methanol conversions were estimated as a function of residence time (mol H^+ s (mol $CH_3OH)^{-1}$) for Eq. 7 using the packed bed differential equation:

$$\frac{\partial X_M}{\partial W} = \frac{1}{F_{M_0}} \frac{k_{DME,D} K_{MMe} K_{Me} P_{CH_3OH} P_{H_2O}^{-1}}{1 + K_D P_{CH_3OH}} \tag{S.26}$$

where X_M is the methanol conversion, F_{M0} is the inlet CH_3OH molar flow rate, the integrand is the rate expression from Eq. 7, and W is the total weight of catalyst to be integrated over. The partial pressure of methanol and water at a given position along the catalyst bed (W) were calculated in terms of conversion as follows:

$$P_{CH_3OH} = \frac{F_{M_0}}{F_{tot}}(1 - X_M) \tag{S.27}$$

$$P_W = \frac{F_{M_0}}{F_{tot}}\left(\frac{X_M}{2}\right) \tag{S.28}$$

where F_{M0} is the initial methanol molar flow rate entering the catalyst bed. The dehydration rate and equilibrium constants were fixed such that the methanol conversion predicted by Eq. S.26 was the same as that measured experimentally (Fig. 2) at a residence time of 3.7 mol H^+ s (mol $CH_3OH)^{-1}$. The differential equation was then solved over a range of residence times (0.01-15 mol H^+ s (mol $CH_3OH)^{-1}$) at 1 kPa of methanol using the same catalyst weight as used to measure the experimental data and is shown in Fig. 2. This qualitative prediction shows a function that bends over sharply with increasing residence time and deviates substantially from the experimentally measured linear dependence of methanol conversion on residence time.

S.13. Derivation of alternative methanol dehydration rate expressions

S.13.1 Kinetically-relevant methoxy formation with empty H^+ sites as a MASI

Rates of DME formation via the dissociative pathway (Scheme 1, main text) can also proceed through methanol monomer dehydration to form surface methoxy as the kinetically-relevant step, with all preceding steps quasi-equilibrated and assuming this step to be irreversible, the rate expression can be described as:

$$r_{D1} = k_{DME,D}[M*] \tag{S.29}$$

where $k_{DME,D}$ is the methoxy formation rate constant and [M*] is the concentration of methanol monomers on the surface. Considering the adsorption of gaseous methanol, at a given partial pressure (P_{CH3OH}), at an empty H^+ site ([*]) to form methanol monomers to be quasi-equilibrated:

$$K_M = \frac{[M*]}{P_{CH_3OH}[*]} \tag{S.30}$$

we can substitute Eq. S.30 into Eq. S.29 to get the rate of DME formation in terms of measureable quantities:

$$r_{D1} = k_{DME,D}K_M P_{CH_3OH}[*] \tag{S.31}$$

Assuming that empty H^+ sites, methanol monomers, and protonated dimers (given by [D*]), which are considered to be inhibitory species for the dissociative pathway, are the most abundant surface intermediates (MASI) during methanol dehydration catalysis, the total number of sites [L] can be expressed as:

$$[L] = [*] + [M*] + [D*] \tag{S.32}$$

Taking protonated dimers to be in quasi-equilibrium with methanol monomers and a gaseous methanol:

$$K_D = \frac{[D*]}{P_{CH_3OH}[M*]} \tag{S.33}$$

Eq. S.32 can be rewritten as:

$$[L] = [*] + K_M P_M[*] + K_D K_M P_{CH_3OH}^2[*] \tag{S.34}$$

Solving for the total number of empty H^+ sites:

$$[*] = \frac{[L]}{1+K_M P_{CH_3OH}+K_D K_M P_{CH_3OH}^2} \tag{S.35}$$

and substituting Eq. S.35 into Eq. S.31 gives the resulting rate expression for DME formation from kinetically-relevant methoxy formation:

$$r_{D1} = \frac{k_{Me}K_M P_{CH_3OH}}{1+K_M P_{CH_3OH}+K_M K_D P_{CH_3OH}^2} \tag{S.36}$$

IR spectra measured during steady-state methanol dehydration catalysis (0.1-22 kPa, 415 K) indicate that all H^+ sites are covered by methanol during catalysis [11]. This eliminates empty H^+ sites as a possible MASI and reduces Eq. S.35 to:

$$[*] = \frac{[L]}{K_M P_{CH_3OH}+K_D K_M P_{CH_3OH}^2} \tag{S.37}$$

This ultimately eliminates the numerator of Eq. S.36 and generates the following function that is always -1 order in methanol under all conditions:

$$r_{D1} = \frac{k_{Me}}{1+K_D P_{CH_3OH}} \tag{S.38}$$

S.13.2 Kinetically relevant DME formation considering reversible methoxy formation

Another alternative rate law can be derived from kinetically-relevant DME formation, but considering methoxy formation to be reversible and quasi-equilibrated. Considering DME formation as the kinetically-relevant step, the rate expression becomes:

$$r_{D2} = k_{DME,D}[MMe*] \tag{S.39}$$

where, [MMe*] is the concentration of methoxy/methanol co-adsorbed species on the surface (Scheme 1, main text). If we consider the formation of methoxy/methanol co-adsorbed species (Eq. S.40), dehydration to form surface methoxy (Eq. S.41), and methanol adsorption to form methanol monomers (Eq. S.42) to be quasi-equilibrated:

$$K_{MMe} = \frac{[MMe*]}{P_{CH_3OH}[Me*]} \tag{S.40}$$

$$K_{Me} = \frac{[Me*]P_{H_2O}}{[M*]} \tag{S.41}$$

$$K_M = \frac{[M*]}{P_{CH_3OH}[*]} \tag{S.42}$$

Eq. S.39 can now be rewritten in terms of measurable quantities:

$$r_{D2} = k_{DME,D} K_{MMe} K_{Me} P_{CH_3OH}^2 P_{H_2O}^{-1}[*] \tag{S.43}$$

Based on IR spectra taken during methanol dehydration catalysis [11], we will consider the MASI to be methanol monomers and protonated dimers, which allows us to write the total number of sites, [L], as:

$$[L] = [M*] + [D*] \tag{S.44}$$

Solving for the number of vacant sites yields Eq. S.37, which can then be substituted into Eq. S.43 to give:

$$r_{D2} = \frac{k_{DME,D} K_{MMe} K_{Me} P_{CH_3OH} P_{H_2O}^{-1}}{1+K_D P_{CH_3OH}} \tag{S.45}$$

S.14. Maximum rate analysis of DFT-predicted DME formation rates

Parallel pathways contribute to overall dimethyl ether (DME) formation rates when transition states with spectating methanol molecules are considered. Therefore, the rates of DME formation are described by a sum of these parallel rates. As shown in Section S.3., methoxy formation is the kinetically-relevant step in the dissociative route. Therefore, the observed rate of DME formation is

$$r_{obs} = \sum_{i=1}^{4} r_{D1,i} + \sum_{j=2}^{4} r_{A,j} \tag{S.46}$$

where i and j represent the total methanol molecules participating in the dissociative and associative route, respectively. This sum represents the experimentally observed DME formation rate

$$r_{obs} = \frac{\sum_{i=1}^{4} \alpha_i P_{CH_3OH}^{i} + \sum_{j=2}^{4} \beta_j P_{CH_3OH}^{j}}{\sum_{m=1}^{5} K_m P_{CH_3OH}^{m}} \tag{S.47}$$

where α_i and β_j represent apparent rate coefficients for the first step of the dissociative route with i total methanol molecules and the associative route with j total methanol molecules, respectively, and K_m represents a lumped equilibrium constant for the formation of a cluster of m methanol molecules.

S.15. DFT-calculated structures of methanol clusters

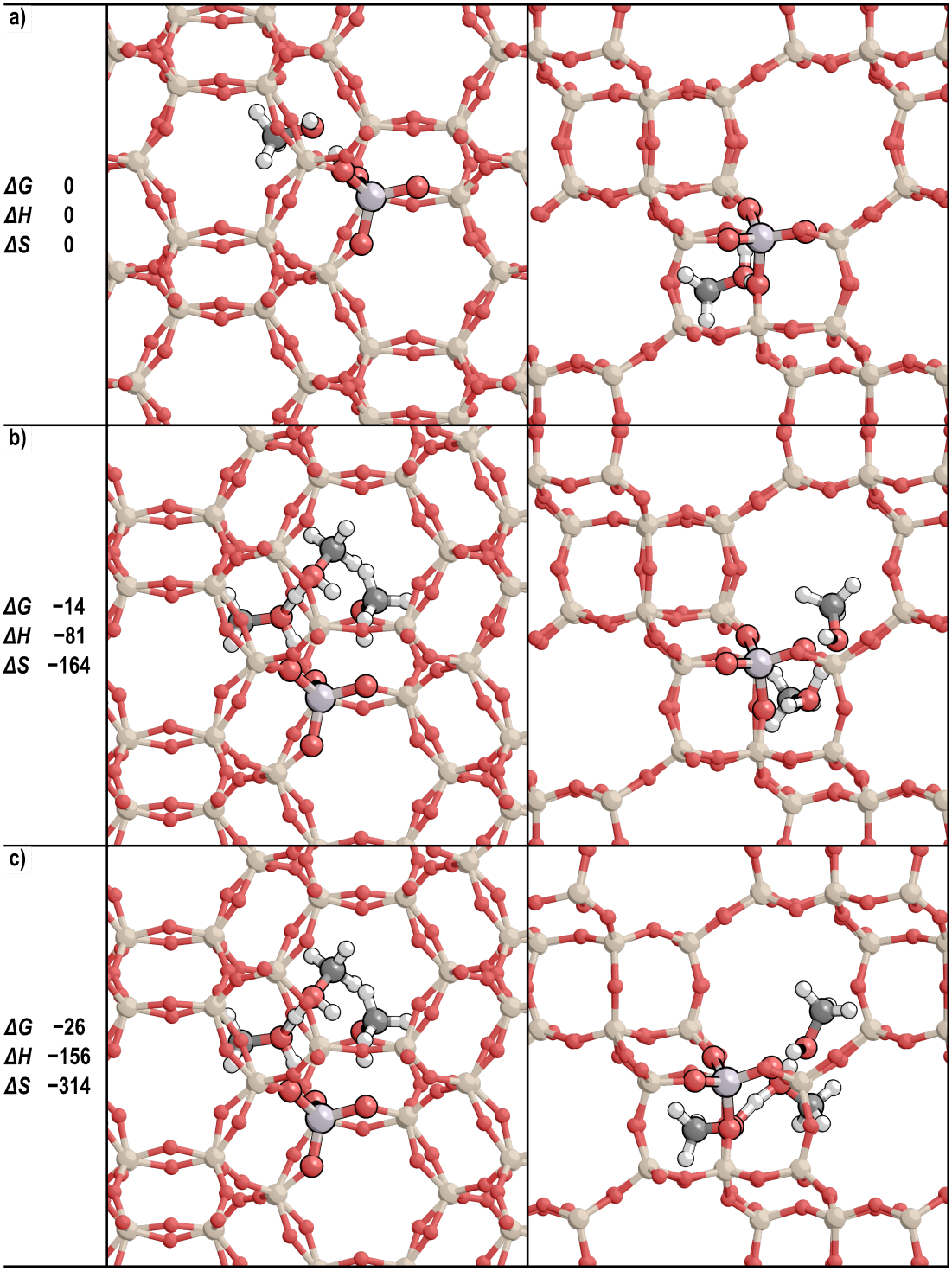

Figure S.19. The most stable methanol clusters shown with views along the c-axis of the CHA unit cell (left) and along the b-axis of CHA (right) with (a) one, (b) two, and (c) three methanol molecules. Free energies (ΔG) and enthalpies (ΔH) in kJ mol^{-1}, and entropies (ΔS) in J mol^{-1} K^{-1}, are shown relative to the methanol monomer at 415 K and 1 bar CH_3OH.

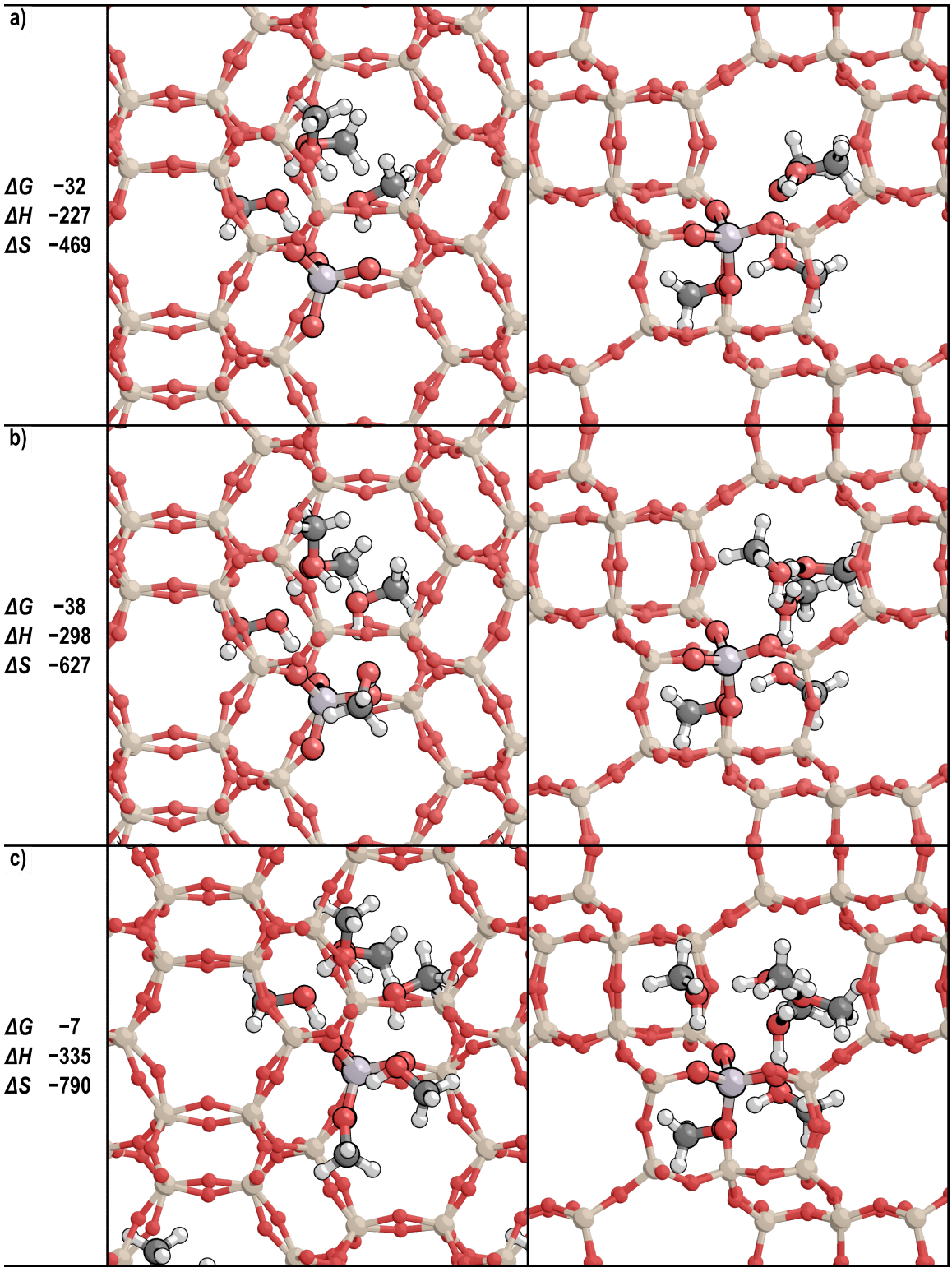

Figure S.20. The most stable methanol clusters with views along the c-axis of the CHA unit cell (left) and along the b-axis of CHA (right) with (a) four, (b) five, and (c) six methanol molecules. Free energies (ΔG) and enthalpies (ΔH) in kJ mol^{-1}, and entropies (ΔS) in J mol^{-1} K^{-1}, are shown relative to the methanol monomer at 415 K and 1 bar CH_3OH.

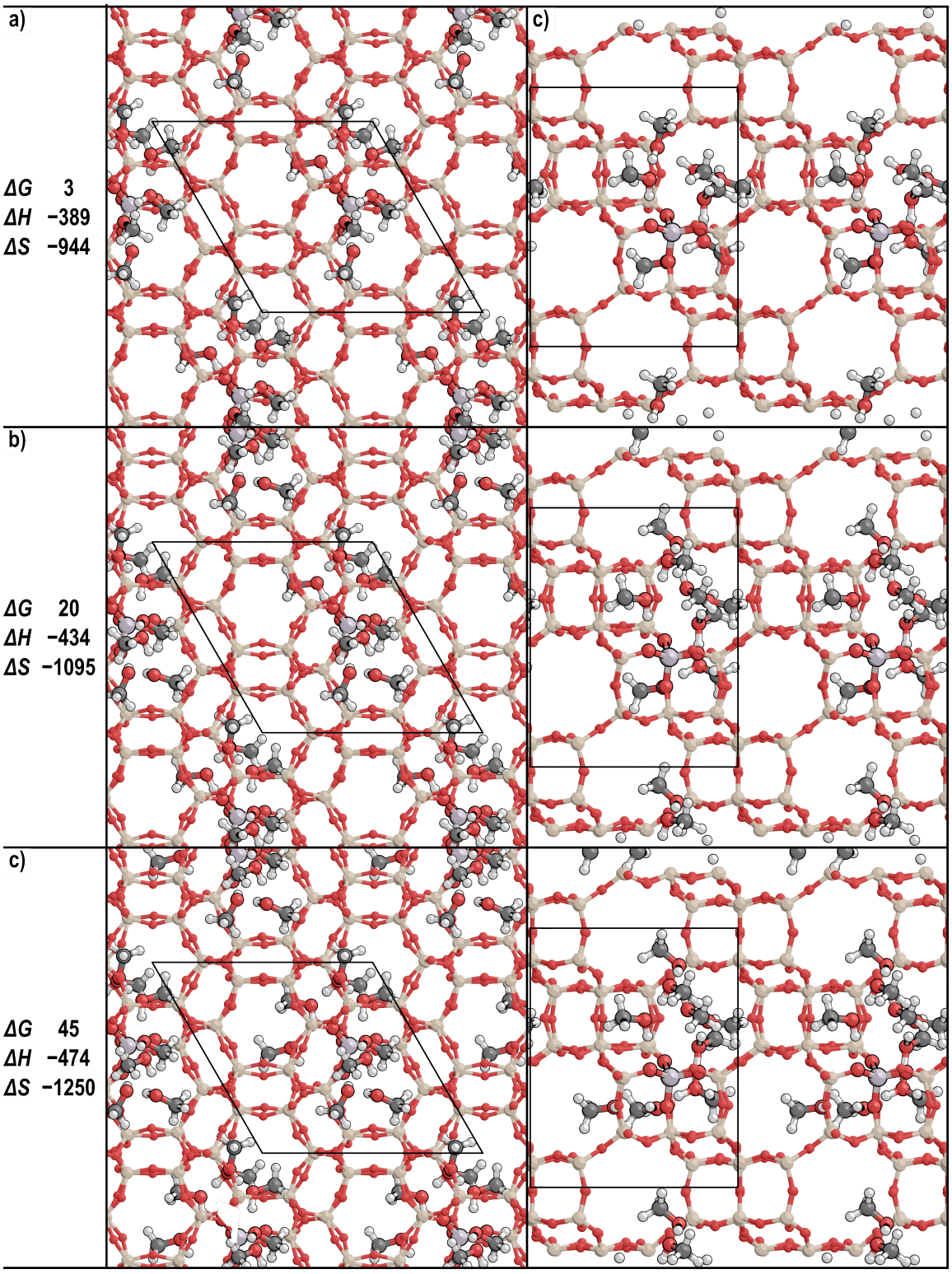

Figure S.21. The most stable methanol clusters with views along the c-axis of the CHA unit cell (left) and along the b-axis of CHA (right) with (a) seven, (b) eight, and (c) nine methanol molecules. Free energies (ΔG) and enthalpies (ΔH) in kJ mol^{-1}, and entropies (ΔS) in J mol^{-1} K^{-1}, are shown relative to the methanol monomer at 415 K and 1 bar CH_3OH.

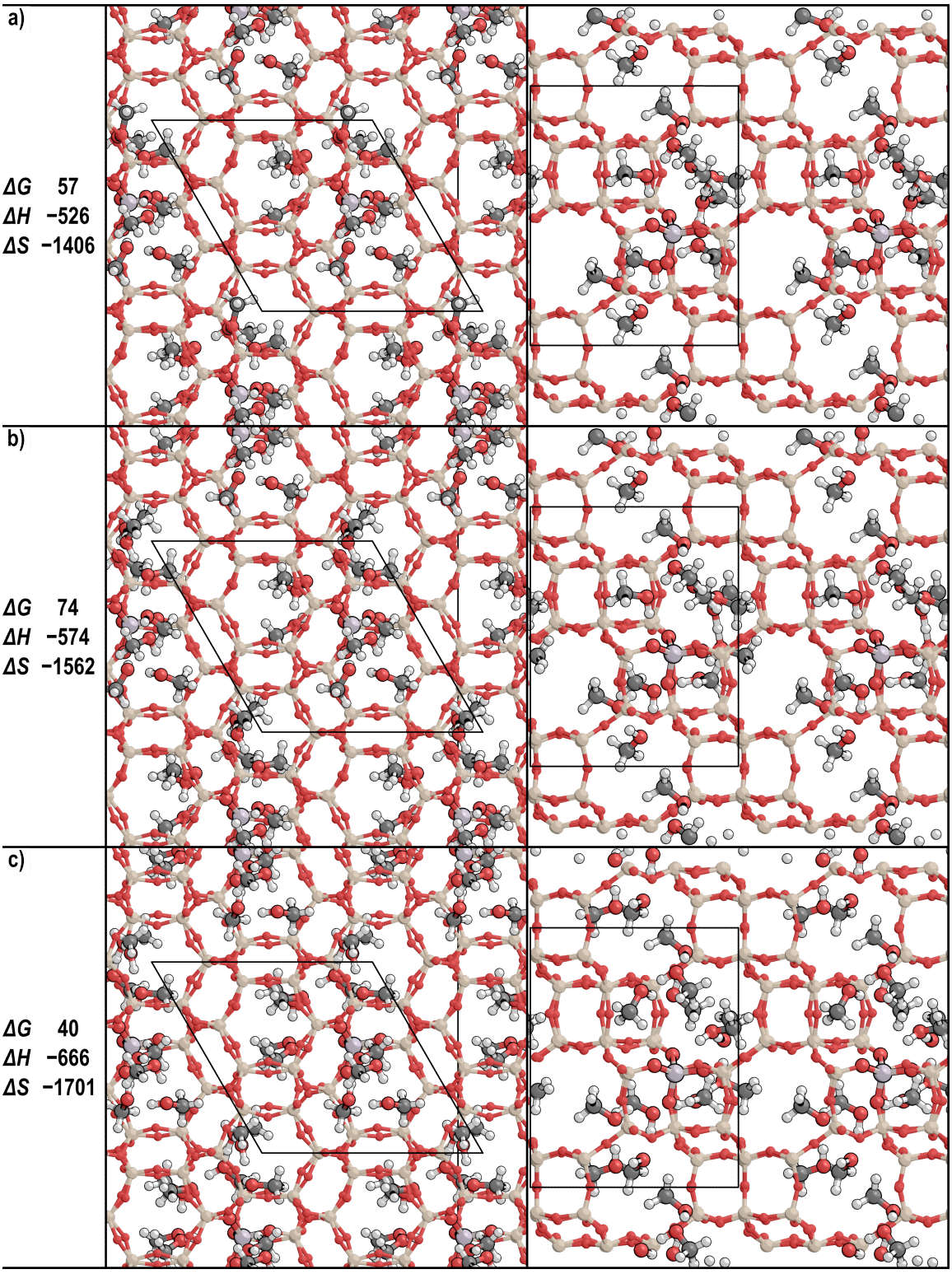

Figure S.22. The most stable methanol clusters with views along the c-axis of the CHA unit cell (left) and along the b-axis of CHA (right) with (a) ten, (b) eleven, and (c) twelve methanol molecules. Free energies (ΔG) and enthalpies (ΔH) in kJ mol^{-1}, and entropies (ΔS) in J mol^{-1} K^{-1}, are shown relative to the methanol monomer at 415 K and 1 bar CH_3OH.

S.16. Derivation of methanol Gibbs free-energies

Values of the methanol Gibbs free energy were calculated as a function of methanol pressure and temperature to relate adsorption equilibrium between gaseous methanol and adsorbed methanol under different conditions. Methanol adsorbed within the pores of CHA was considered to be similar to liquid methanol, due to the presence of methanol clusters in IR spectra (~3370 cm^{-1}) measured during methanol dosing experiments (Fig. 10, main text) and during steady-state methanol dehydration catalysis [11]. The vibrational band attributed to methanol clusters represents perturbed H-bonding interactions between adjacent methanol molecules that are assumed to be more similar in structure to liquid methanol than to gaseous methanol. While this assumption does not account for strong interactions between methanol monomers and bare H^+ sites or for stabilization via van der Waals interactions with the framework, it does provide an initial approximation of methanol coverage within CHA under reaction conditions (>0.01 kPa CH_3OH, 415 K). DFT calculations, which are able to rigorously account for differences in the adsorption free energy of different sized methanol clusters and for interactions between adsorbed methanol with the zeolite framework, predict methanol coverages similar to those estimated by assuming equilibrium with an ideal liquid-like adsorbed methanol (Fig. 11, main text).

Equilibrium between gaseous methanol and adsorbed, liquid-like methanol occurs when the chemical potential (μ) of both states are equal:

$$\mu_m = \mu_{m*} \tag{S.48}$$

where μ_m is the chemical potential of gaseous methanol and μ_{m*} is the chemical potential of adsorbed methanol. Here changes in free energy of the zeolite lattice upon adsorption of methanol are assumed to be negligible. The chemical potential of a species, i, can then be expressed as the sum of the ideal state (μ^0) and the excess chemical potential (μ^ε):

$$\mu_i = \mu_i^0 + \mu_i^\varepsilon \tag{S.49}$$

where μ^ε of species i (μ_i^ε) can be expressed in terms of the activity of species i (a_i):

$$\mu_i^\varepsilon = RT\ln[a_i] \tag{S.50}$$

Substituting Eq. S.49 and S.50 into S.48 yields:

$$\mu_m^0 + RT\ln[a_m] = \mu_{m*}^0 + RT\ln[a_{m*}] \tag{S.51}$$

Estimation of the gas-phase methanol activity coefficient (γ_M) at 415 K using the Peng-Robinson equation of state gives activity coefficients near unity (γ_M>0.98), indicating that under the conditions studied here (415 K, 0.01-50 kPa CH3OH), gas-phase methanol behaves as an ideal gas. As a result, a_m can be rewritten as:

$$a_m = \frac{P_m}{P_0} \tag{S.52}$$

where P_m is the partial pressure of methanol and P_0 is a reference pressure of 1 bar. The activity of the adsorbed methanol phase was considered by treating adsorbed methanol as a pure-component liquid, in order to approximate the equilibrium between gaseous and adsorbed

methanol. The activity of adsorbed methanol can be written in terms of the fugacity of adsorbed methanol (f_{m*}) at a given T and P:

$$a_{m*} = \frac{f_{m*}}{f^0_{m*}} \tag{S.53}$$

where f^0_{m*} is the fugacity of methanol under a reference condition of 1 bar. The fugacity of adsorbed liquid-like methanol can then be related to a saturated liquid using a Poynting factor:

$$f_{m*} = \varphi^{sat}_{m*} P^{sat}_{m*} \exp\left[\frac{v_{m*}}{RT}(P - P^{sat}_{m*})\right] \tag{S.54}$$

and at low pressures, the Poynting factor approaches unity and by considering adsorbed methanol as an ideal liquid, Eq. S.54 reduces to:

$$f_{m*} = P^{sat}_{m*} \tag{S.55}$$

Eq. S.53 can now be rewritten in terms of P^{sat}_{m*}, referenced to a pressure of 1 bar:

$$a_{m*} = \frac{P^{sat}_{m*}}{P_0} \tag{S.56}$$

Rearranging Eq. S.51 and substitution of Eq. S.52 and S.56 yields:

$$\mu^0_{m*} - \mu^0_m = RT\ln\left[\frac{P_m}{P_0}\right] - RT\ln\left[\frac{P^{sat}_{m*}}{P_0}\right] \tag{S.57}$$

Assuming a constant T and P process, the change in the chemical potential can then be rewritten in terms of the change in Gibbs free energy (per mole) and results in Eq. 9 of the main text:

$$\Delta G_m = RT\ln\left[\frac{P_m}{P^{sat}_{m*}}\right] \tag{S.58}$$

Eq. S.58 provides an estimation of the difference in free energy between adsorbed methanol and gaseous methanol as a function of temperature and pressure. This equation was then used to calculate the free energy of methanol at different partial pressures during methanol adsorption isotherms (293 K) and under reaction conditions (415 K) to estimate the coverage of methanol during methanol dehydration catalysis (Fig. 9, main text).

S.17. Complete methanol dehydration reaction network

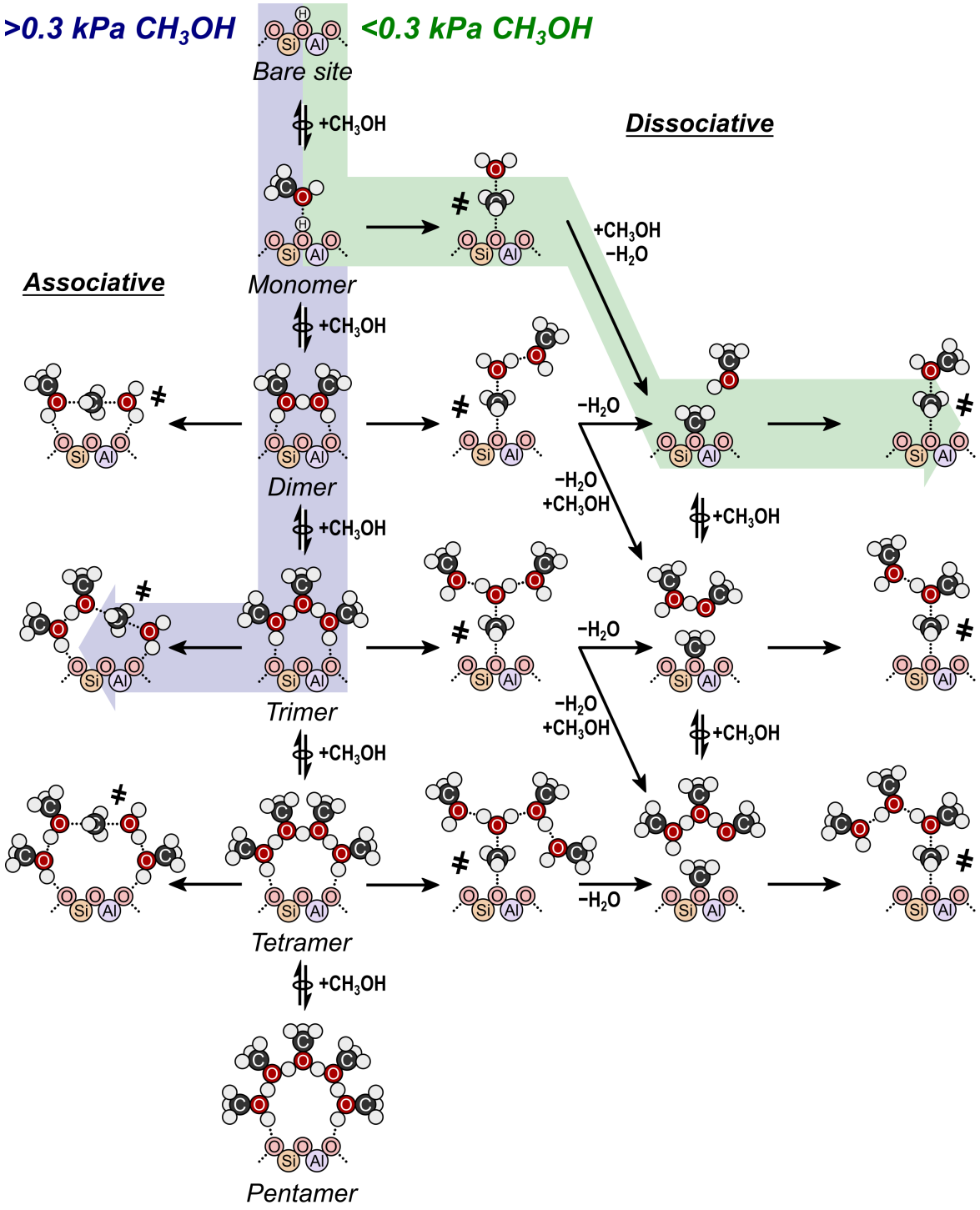

Scheme S.4. Complete methanol dehydration reaction network for the associative and dissociative dehydration mechanisms as a function of methanol coverage. The most favorable reaction pathway for methanol pressures <0.3 kPa and >0.3 kPa are highlighted in green and

blue, respectively, and correspond to the maximum rate analysis presented in Figure 16 of the main text.

S.18. References

[1] D.A. McQuarrie, Statistical mechanics, University Science Books, Sausalito, Calif, 2000.

[2] C. Baerlocher, L.B. McCusker, Database of Zeolite Structures: http://www.iza-structure.org/databases., (2013). http://www. iza-structure. org/databases (accessed January 5, 2017).

[3] S. Nystrom, A. Hoffman, D. Hibbitts, Tuning Brønsted acid strength by altering site proximity in CHA framework zeolites, ACS Catal. 8 (2018) 7842–7860. doi:10.1021/acscatal.8b02049.

[4] M. DeLuca, P. Kravchenko, A. Hoffman, D. Hibbitts, Mechanism and Kinetics of Methylating C_6 –$C1_2$ Methylbenzenes with Methanol and Dimethyl Ether in H-MFI Zeolites, ACS Catal. 9 (2019) 6444–6460. doi:10.1021/acscatal.9b00650.

[5] A. Ghorbanpour, J.D. Rimer, L.C. Grabow, Computational Assessment of the Dominant Factors Governing the Mechanism of Methanol Dehydration over H-ZSM-5 with Heterogeneous Aluminum Distribution, ACS Catal. 6 (2016) 2287–2298. doi:10.1021/acscatal.5b02367.

[6] R.T. Carr, M. Neurock, E. Iglesia, Catalytic consequences of acid strength in the conversion of methanol to dimethyl ether, J. Catal. 278 (2011) 78–93. doi:10.1016/j.jcat.2010.11.017.

[7] W. Song, D.M. Marcus, H. Fu, J.O. Ehresmann, J.F. Haw, An oft-studied reaction that may never have been: direct catalytic conversion of methanol or dimethyl ether to hydrocarbons on the solid acids HZSM-5 or HSAPO-34., J. Am. Chem. Soc. 124 (2002) 3844–3845. doi:10.1021/ja016499u.

[8] S. Chen, E.I. Izgorodina, Prediction of 1H NMR chemical shifts for clusters of imidazolium-based ionic liquids., Phys. Chem. Chem. Phys. 19 (2017) 17411–17425. doi:10.1039/c7cp02951a.

[9] H. Eyring, The Activated Complex in Chemical Reactions, J. Chem. Phys. 3 (1935) 107. doi:10.1063/1.1749604.

[10] M.G. Evans, M. Polanyi, Some applications of the transition state method to the calculation of reaction velocities, especially in solution, Trans. Faraday Soc. 31 (1935) 875. doi:10.1039/tf9353100875.

[11] J.R. Di Iorio, C.T. Nimlos, R. Gounder, Introducing Catalytic Diversity into Single-Site Chabazite Zeolites of Fixed Composition via Synthetic Control of Active Site Proximity, ACS Catal. 7 (2017) 6663–6674. doi:10.1021/acscatal.7b01273.